Metallurgical Investigation
Final Report

Subject: **Metallurgical Investigation of Fan Blades from PW4077 Engine SN 777047**

Date: **February 24, 2023**

Summary and Conclusions:

Fan blade S/N CBDUAU9992 fractured due to fatigue, which initiated internally ~6.6” above the root bottom from multiple origins in cavity FA along the transition radius between the convex side wall and the internal spanwise rib. The origins were located near the radius runout to the rib which exhibited an irregular contour (lack of tangency).

Field Emission Scanning Electron Microscope (FESEM) examination identified three primary surface origins associated with most of the crack progression. The early crack progression exhibited predominantly faceted growth mixed with occasional areas of fatigue striations. Beyond this early progression zone, about 0.063” deep (towards the convex wall), the fatigue crack transitioned to a predominantly striated growth mode consistent with stable low cycle fatigue (LCF) growth. Areas of the crack progression exhibited near fully faceted growth that tended to propagate in the chordwise direction, suggestive of microtexture regions (MTRs). There were no MTRs identified at the primary fatigue origins. A striation count conducted from 0.063” to 0.199” from the origin estimated 3,150 cycles of LCF crack propagation within the stable zone. Beyond the stable LCF zone, multiple separately nucleated faceted regions were encountered, consistent with MTRs. Beyond this region, the crack surface exhibited unstable progression, leading ultimately to final fracture.

In addition to the primary fracture, multiple fatigue cracks were identified in the flowpath and midspan of the subject blade. Many of the cracks exhibited multiple origins, consistent with the primary fracture.

Metallographic sections through multiple internal cavities on the blade identified light etching of the alpha grains within 0.003” of the surface, indicating possible surface contamination. Fatigue test results of specimens removed from the cavity surfaces verses specimens removed from the bulk material of the blade identified a lower fatigue capability of the cavity surfaces. Microhardness testing revealed a slight increase in hardness within 0.005” of the surface. Additionally, areas of the blade that were force fractured open exhibited faceted grains, 2-3 grains deep, along the cavity surfaces before transitioning to dimple overstress features. Advanced characterization confirmed a carbon contamination gradient that extended from the cavity surfaces.

Overall, the lab investigation identified two conditions at the fracture origin which both contributed to the in-service fatigue fracture of the subject event fan blade: 1) the irregular contour of the fillet radius which resulted in a stress concentration at the fracture origin and 2) a diffused contamination layer (surface contamination) along the internal cavity which reduced the fatigue capability of the material.

Acronym Glossary

ATB - Air turnback
CC - Concave
CV - Convex
EBSD - Electron Backscatter Diffraction
EDM - Electrical Discharge Machining
EMP - Electron Microprobe
FESEM - Field Emission Scanning Electron Microscope
FPI - Fluorescent Penetrant Inspection
GDMS - Glow Discharge Mass Spectrometry
HF - Hydrofluoric
LCF - Low Cycle Fatigue
LE- Leading Edge
MTR - Microtexture Region
NTSB - National Transportation Safety Board
OIM - Orientation Image Mapping
P&W - Pratt & Whitney
SEM - Scanning Electron Microscope
SIMS - Secondary Ion Mass Spectrometry
TAI - Thermal acoustic imaging
TE - Trailing Edge
UAL - United Airlines
UT - Ultrasonic
XPS - X-ray Photoelectron Spectroscopy

1.0 Background

On February 20th, 2021, United Airlines (UAL) Boeing 777-220, powered by PW4000-112" engines, experienced a fan blade fracture from engine P777047 during climb from Denver resulting in an air turnback (ATB) and emergency landing. Blade no. 19, S/N CBDUAU9992, fractured from fatigue at the flowpath of the blade. The fan blade had a total of 77,827 hours and 15,379 cycles. It was last inspected by thermal acoustic imaging (TAI) 2,979 cycles prior to the event.

Multiple pieces of the event fan blade in addition to the following blade were returned to Pratt & Whitney (P&W) in East Hartford, CT for metallurgical investigation under the supervision of the National Transportation Safety Board (NTSB). The pieces included the root section that was still installed on the engine following the event, a midspan portion of the blade that had been lodged in the fan containment case during the event, two fragments from the outboard portion of the event blade which were recovered from the ground following the event, and additional small fan blade fragments recovered during teardown that exhibited significant secondary damage.

The following blade, no. 18, CBDUA49233, was fractured at the midspan due to impact damage from the event blade (*Reference Section 3.0).* The remaining blades from the engine ("sister blades") were damaged due to the event and returned to P&W for additional non-destructive and destructive evaluations (*Reference Section 4.0).*

2.0 Details of Examination - S/N CBDUAU9992 (Blade No. 19)

The root section that was still installed on the engine following the event measured approximately 15" x 7.6", weighed 10.8 lbs./4.9 kg, and contained the inboard half of the primary fracture surface. It was labeled as blade #19 prior to receipt (*Reference Section 2.1*). A large midspan portion of the blade that had been lodged in the fan containment case during the event was recovered at engine teardown and submitted for investigation. It measured approximately 19" x 22", weighed 12.9 lbs./5.8 kg, and contained the outboard half of the primary fracture (*Reference Section 2.2*). Two additional blade fragments that were confirmed to be from the outboard portion of the event blade were recovered from the debris on the ground following the event. The larger of the two fragments measured approximately 13"x5.5" and weighed 1.9 lbs./0.8 kg. The smaller of the fragments measured approximately 4.75"x5.5" and weighed 0.6 lbs./0.3 kg (*Reference Section 2.3*). Additional small fan blade fragments were recovered as well, all measuring less than 2" x 2". The fragments exhibited significant secondary damage and it could not be confirmed which part of the blades most of the fragments were originally from (*Reference Section 2.4*).

In addition to the primary fracture, multiple cracks were identified on the event blade fragments and further evaluated. Images showing the event blade fragments and the approximate fatigue fracture/crack locations marked on a blade diagram are shown in **Figure 1**. The part manufacture and repair identification markings located on the root bottom of the event blade are shown in **Figure 2.**

2.1 CBDUAU9992 Blade Root

2.1.1 Primary Flowpath Fracture Surface

2.1.1.1 Visual and Binocular Review

The transverse fracture through the flowpath region of the airfoil on the event fan blade was due to fatigue, which initiated internally at the forward end of cavity FA, approximately 6.6” outboard of the blade root bottom face and 5.0” from the trailing edge (TE) (**Figure 3**). The crack progressed from along the transition radius between the convex side wall and an internal spanwise rib, closer to the radius runout to the rib. A white deposit was observed on areas of the fracture surface and on the internal cavity walls (**Figure 4**). The deposit appeared secondary to the fracture and was removed with coolant during initial sectioning. It was reported that fire retardant, a white foamy material, was used following the event.

The transition radius between the internal rib and convex side wall in cavity FA was replicated just inboard of the fracture location using rubber replicating material. The radius runout to the rib exhibited an irregular contour (lack of tangency) (**Figure 5**). P&W structural analysis found this radius geometry resulted in a stress concentration at the fracture origin.

2.1.1.2 SEM Examination

The part was sectioned down via wire electrical discharge machining (EDM) for further analysis. A chordwise section was prepared 1” below the fracture surface and the origin area between cavities FA and EA was removed (**Figure 6**). Binocular examination and fluorescent penetrant inspection (FPI) of the sectioned piece identified multiple secondary cracks inboard of the fracture surface (*Reference Sections 2.1.2 – 2.1.3*). An additional section was made via wire EDM to separate the fracture surface from the secondary cracks for further analysis of both (**Figure 7**).

Scanning electron microscope (SEM) examination of the fracture surface identified multiple fatigue origins along the surface near the radius runout to the rib. Most of the origins were located within 0.031” of the radius runout to the rib. Both surface grain origins and featureless facet origins were identified (**Figure 8**). High magnification SEM examination of the cavity surface at the fatigue origins did not find evidence of damage or anomalies. Fractographic mapping of the fracture features identified three primary origins associated with most of the crack progression (**Figure 9**). The primary origin associated with the through-wall progression was located approximately 0.025” from the irregular contour located at the radius runout to the rib (**Figure 10**). The fractographic assessment did not identify microtexture regions (MTRs) at the primary origins. Subsequent electron backscatter diffraction (EBSD) of a metallurgical section planar into this area confirmed that no MTRs were present at the primary origin area (*Reference Section 2.2.1.3, Figure 44*).

The early crack progression exhibited predominantly faceted growth with a mix of cleavage and striations (**Figure 11**). Beyond this early progression zone, approximately 0.063” deep, the fatigue crack transitioned to predominantly striated growth, consistent with stable low cycle fatigue (LCF), with faceted growth mixed in at varying levels (**Figure 12**). Occasional areas of the crack progression exhibited near fully faceted growth that tended to propagate in the chordwise direction, suggestive of MTRs. Beyond the stable LCF zone, approximately 0.199” from the primary origin, multiple separately nucleated faceted regions were encountered, consistent with MTRs. Beyond this region, the crack surface exhibited a gradual transition to dimple rupture features indicative of unstable progression, leading ultimately to final fracture.

A striation count was conducted from 0.063” to 0.199” from the origin. The crack growth rate ranged from $5.4x10^{-6}$ to $6.7x10^{-5}$ inches/cycle. No credit was taken for cycles prior to 0.063” because the area was not predominantly striated. Additionally, no credit was taken for cycles beyond the separately nucleated MTRs (beyond 0.199” from the origin) because it was unknown whether or not the MTRs grew simultaneously with the rest of the crack progression (**Figure 13**). Since the crack growth rate observations were from predominantly striated areas that exhibited some amount of faceted growth mixed in, image analysis was used to determine the area fraction of striations at each observation. The area fractions were then used to adjust (reduce) the estimated crack growth cycles. No credit was taken for a region of crack growth that consisted of less than 50% striations. Relatively weak separately nucleated initiations were observed in the striation count region but did not impede the major crack progression. After the adjustments, the striation count estimated 3,150 cycles of LCF crack propagation within the stable zone (**Figure 14**). The blade was last inspected via thermal acoustic imaging (TAI) 2,979 cycles ago. Based on the striation count data, the crack would have been ~0.064” deep at that time.

2.1.1.3 Metallographic Examination

Metallographic sections were completed in cavity FA inboard of the fracture surface for an initial evaluation of the microstructure and for possible surface deformation caused by machining. Four sections were prepared in cavity FA including a transverse/chordwise section into the rib/walls (section A), a longitudinal/spanwise section through the rib on the convex side (section B), a longitudinal/spanwise section through the rib on the concave side (section C), and a longitudinal/spanwise section into the convex wall (section D) (**Figure 15**). No surface deformation or secondary cracks were observed in any of the sections. The bulk microstructure appeared typical of Ti 6Al-4V when etched with Kroll’s Reagent (i.e., Kroll’s) and 1% hydrofluoric acid solution (i.e., 1% HF). The alpha grains at the surface etched lighter when etched with 1% HF. This effect was observed on all internal surfaces of the blade that were evaluated. It was not observed on external surfaces of the blade or along the bond lines (**Figures 16-19**).

A spanwise metallographic section was also prepared into the primary origin as shown in **Figure 20**. Three step polishes at 0.001” increments were made into the primary origin. The section was etched with Kroll’s and 1% HF at each increment. No distorted surface layer/deformation was observed. Alpha grains within 0.002”-0.003” of the internal surface etched lighter when etched with 1% HF. Representative images of the step polishes are shown in **Figure 21**.

2.1.2 **Secondary Chordwise Cracks**

2.1.2.1 Visual and Binocular Review

The secondary cracks identified inboard of the flowpath fracture were all located within 0.68” of the fracture surface. Multiple mostly-chordwise oriented cracks, parallel to the fracture surface, were identified in the transition radius between the convex wall and the internal rib at the forward end of the FA cavity. They were approximately aligned with the origin area on the fracture surface. The secondary crack closest to the fracture surface exhibited a spanwise jog of the crack that aligned with the irregular contour of the radius runout to the rib. After sectioning the fracture surface from the secondary cracks, an additional chordwise section was made via wire EDM as shown in **Figure 22** to prepare for metallography on the two cracks furthest from the fracture surface (*Reference Section 2.1.2.3*).

2.1.2.2 SEM Examination

The largest of the chordwise secondary cracks inboard of the fracture surface was fractured open. The maximum crack depth measured 0.065" (**Figure 23**). Binocular review of the outboard half of the crack identified an additional crack plane at the irregular contour of the radius runout to the rib (**Figure 24**).

SEM examination of the fractured open secondary crack identified multiple origins near the radius runout to the rib, similar to what was observed on the primary fracture surface. A mix of featureless facets and surface origins were observed. The primary origin associated with the crack progression in the through-wall direction was in the transition radius, approximately 0.016" from the irregular contour at the radius runout to the rib (**Figure 25**). The early crack progression exhibited predominantly faceted growth with a mix of cleavage and striations, consistent with the fracture surface. Four discrete striated bands were observed in the crack progression between 0.015" and 0.063" from the primary origin. At these locations, less than approximately 50% striations were observed therefore a full striation count could not be completed. The crack growth rate ranged from $2.9x10^{-6}$ to $6.9x10^{-6}$ inches/cycle which followed a similar trend as the primary fracture (**Figures 26 and 27**).

2.1.2.3 Metallographic and EBSD/OIM Examination

A planar section was prepared into the outboard half of the largest secondary chordwise crack that was previously broken open. EBSD/orientation image mapping (OIM) was completed to characterize MTRs near the origins. The primary origin on the crack aligned with an MTR which may have contributed to crack growth (**Figures 28 and 29**). The section was etched with 1% HF and Kroll's after EBSD/OIM. Alpha grains near the surface etched lighter when etched with 1% HF but no distorted surface layer/deformation was observed (**Figure 30**).

A longitudinal/spanwise section was prepared into the two secondary chordwise cracks furthest away from the fracture surface. Multiple polishes at 0.005" increments were completed into the cracks until the plane of polish was located at approximately the radius runout to the rib, near where the origins were located on the previously evaluated secondary crack and fracture. The maximum crack depths observed in the polishes were 0.053" and 0.034" for the outboard and inboard cracks, respectively. The section was etched with Kroll's and 1% HF. The bulk microstructure appeared typical of Ti 6Al-4V. Light etching of the alpha grains within 0.002"-0.003" of the internal surface was observed. No surface deformation or microcracking along the surface was observed (**Figure 31**).

2.1.3 **Secondary Spanwise Crack**

2.1.3.1 Visual and Binocular Review

Visual and binocular review of the secondary cracks inboard of the fracture surface also identified a more spanwise oriented crack located in the convex wall side of the transition radius. The outboard edge of the crack was located approximately 0.33" from the fracture surface. The outboard and inboard edges of the spanwise crack were oriented in a more chordwise direction. The spanwise crack was broken open. It measured approximately 0.117" in length and 0.035" in depth (**Figure 32**).

2.1.3.2 Keyence 3D Scan

A 3D scan of the spanwise crack showed the crack was changing planes at the extremities. The features appeared to grow into a more chordwise plane direction, particularly at the inboard and outboard edges of the crack (**Figure 33**).

2.1.3.3 SEM Examination

SEM examination identified multiple origins along the surface of the spanwise crack. Both surface grain origins and featureless facet origins were identified. Crack growth at the origins was made up of predominantly faceted features that progressed along the surface, indicating a possible MTR contribution. Areas of the crack progression exhibited near fully faceted growth that tended to propagate in the spanwise direction, suggestive of MTRs. Toward the crack extremity, features appeared to propagate into a chordwise plane direction (**Figures 34 - 36**). Further examination identified multiple secondary cracks beyond the spanwise crack extremity. Faceted grains were observed along the surface of the secondary cracks (**Figure 37**).

2.1.3.4 Metallographic Examination

A transverse section was prepared into the primary origin on the half of the crack away from the radius where the chordwise cracks were located. Four step polishes were prepared through the primary origin on the spanwise crack. 1% HF and Kroll's etches were completed at each increment. Alpha grains near the surface etched lighter when etched with 1% HF. There was also banding of the microstructure observed near the origin. No distorted surface layer/deformation was observed, and no abnormalities were noted at the origin. Secondary cracks, up to 0.001" in depth were observed approximately 0.07" from the spanwise crack. It was unclear if these cracks were a result of breaking the spanwise crack open or if they were prior existing (**Figure 38**).

2.2 CBDUAU9992 Midspan Blade Fragment

A fan blade fragment that had been lodged in the fan containment case during the event was removed and submitted for investigation. The fragment was confirmed to be part of the midspan of the fractured blade. It measured approximately 19" x 22", weighed 12.9 lbs./5.8 kg, and contained the outboard half of the primary fracture (**Figure 39**).

2.2.1 Outboard Half of Primary Flowpath Fracture

2.2.1.1 Visual and Binocular Review

The mating flowpath origin area was mostly intact but exhibited secondary damage from the post-fracture event. The convex and concave sides of the blade were disbonded at several spanwise ribs in the flowpath due to secondary damage. The origin area was sectioned from the fragment for further evaluation (**Figure 40**). Binocular review identified two additional secondary cracks outboard of the fracture surface. The furthest outboard crack was located ~0.32" from the fracture origin. The fracture surface was sectioned from the secondary cracks via wire EDM for further evaluation (**Figure 41**).

2.2.1.2 SEM Examination

SEM examination of the outboard half of the fracture surface found features consistent with those observed on the inboard side of the fracture. Further examination did not identify any additional anomalies or discontinuities at the origins (**Figure 42**).

2.2.1.3 Metallographic and EBSD/OIM Examination

A metallographic section was prepared planar into the outboard half of the fracture surface as shown in **Figure 43**. EBSD/OIM evaluation of the section confirmed that there were no MTRs at the primary origin (**Figure 44**). The planar section was etched with 1% HF. The alpha grains near the cavity surface etched lighter. No distorted surface layer/deformation was observed. A spanwise microcrack, approximately 0.001” in depth, was observed at the radius runout to the rib (**Figure 45**).

2.2.2 Outboard Secondary Chordwise Crack

2.2.2.1 Visual and Binocular Review

The large crack outboard of the fracture surface was broken open. The maximum crack depth measured 0.053” (**Figure 46**). In total, the fracture origin area and parallel secondary cracks outboard and inboard of the fracture spanned approximately 1.0” in the cavity, from approximately 5.9” to 6.9” above root bottom.

2.2.2.2 SEM Examination

The outboard secondary crack origin area was located at the radius runout to the rib, consistent with the flowpath fracture surface and other secondary cracks. Some of the crack surface was smeared, likely due to damage during the event (**Figure 47**). During SEM examination of the surface surrounding the crack, a spherical metallic deposit, consistent with what has been previously determined to be a “spark” from original machining, was observed 0.070” outboard of the secondary crack. There were no sparks observed at the origin area of the secondary crack and there were no cracks observed at the spark (**Figure 48**).

2.2.3 Midspan Crack I – Cavity CD/DD

2.2.3.1 Visual and Binocular Review

Binocular examination of the midspan blade fragment that was removed from the case identified possible fatigue on the outboard surface, located on the spanwise rib between cavities CD and DD approximately 0.2” outboard of the inboard chordwise rib (**Figure 49**). The fatigue appeared to extend under a flap of material on the convex side of the blade. The area was sectioned from the blade fragment and the flap of material was removed for further evaluation (**Figure 50**).

2.2.3.2 SEM Examination

SEM examination confirmed fatigue features on the crack. Areas of striations and faceted features were identified among large areas of secondary damage/smearing. Fatigue features progressed from an origin area located on the CD side of the rib, however, due to the secondary damage, the exact origin could not be identified. Fatigue features were observed progressing along the concave wall (**Figure 51**). Crack growth rate measurements were taken at points progressing both towards the concave and convex walls. The path towards the convex wall was less damaged. Crack growth rates

ranged between $9.6x10^{-06}$ – $8.5x10^{-05}$ in/cycle. A complete striation count could not be completed due to the extent of secondary damage.

2.3 CBDUAU9992 Outboard Blade Fragments

Two additional blade fragments that were confirmed to be from the outboard portion of the event blade were recovered from the debris on the ground following the event. The larger of the two fragments measured approximately 13”x5.5” and weighed 1.9 lbs./0.8 kg (**Figure 52**). Remnant part markings included the last 5 digits of the event blade S/N – “U9992”, confirming that the fragment was from the event blade. The smaller of the fragments measured approximately 4.75”x5.5” and weighed 0.6 lbs./0.3 kg.

2.3.1 Midspan Crack II – Cavity CD/DD

2.3.1.1 Visual and Binocular Review

Binocular microscope inspection of the fracture surfaces identified possible fatigue on the inboard side of the fragment between cavities CD and DD, approximately 0.1” inboard of the outboard chordwise rib in cavity CD (**Figure 53**). The region of possible fatigue was sectioned from the outboard blade fragment (**Figure 54**).

2.3.1.2 SEM Examination

SEM examination confirmed fatigue on the fracture surface. Areas of striations and faceted features were identified interspersed among large areas of secondary damage/smearing. The fatigue progressed from an area near the bond line in cavity CD. Due to the secondary damage, the exact origin area could not be identified (**Figure 55**). Crack growth rate measurements were taken at points along the rib progressing towards both the concave and convex walls. The path towards concave wall was less damaged; more data was able to be gathered on this side. Crack growth rates at points towards the concave wall ranged from $6.0x10^{-06}$ – $4.9x10^{-05}$ in/cycle and the crack growth rates at points towards the convex wall ranged from $6.5x10^{-06}$ – $2.9x10^{-05}$ in/cycle (**Figure 56-57**). A complete striation count could not be completed due to the extent of damage.

2.3.2 Bond Line Evaluation

2.3.2.1 Visual and Binocular Review

The bond line between cavities CD and CE, adjacent to the midspan crack in the outboard blade fragment, appeared separated. It was removed from the part for further evaluation (**Figure 58**).

2.3.2.2 SEM Examination

SEM examination of the disbonded rib between cavities CE and CD identified elongated ductile dimples and rub/smear. No fatigue was observed (**Figure 59**).

2.3.2.3 Metallographic Examination

A metallographic section was prepared through an area of the spanwise rib that appeared intact just outboard of the midspan crack in the outboard blade fragment. No voids or unbonded areas were observed. The 1% HF etch did not reveal any light etch layer along the bond line. The fishmouth feature extended 0.002” which was acceptable per bond quality requirements (**Figure 60**).

2.3.3 **Midspan Crack III – Cavity CE**

2.3.3.1 Visual and Binocular Review

Binocular review and FPI identified crack-like indications on the convex wall side of Cavity CE, adjacent to where the bond line was disbonded and previously evaluated. The indications were located in the radius between the convex wall skin and the chordwise rib between cavities CE and CD. The cavity side wall in this area was deformed, most likely due to secondary damage (**Figure 61**).

2.3.3.2 SEM Examination

The broken open crack at the LE corner of the cavity measured 0.068” x 0.011”. SEM examination confirmed fatigue features. Features near the cavity surface were faceted. The progression exhibited a mix of faceted and crystallographic features, with isolated striated grains (**Figure 62**). SEM examination also identified faceted areas one or two grains deep along the surface in the force fractured region outside of the broken open crack. The remainder of the force fractured surfaces exhibited smear or ductile dimples, typical of overstress (**Figure 63**). FPI indications at the TE side of the cavity were also force fractured open. Smeared ductile dimples, indicative of overstress, up to 0.008” in depth, were observed (**Figure 64**).

2.3.3.3 Metallographic Examination

A metallographic section was prepared longitudinally through the indications observed on the TE side of cavity CE, located in the chordwise rib radius. An open crack-like feature, approximately 0.008” in depth was observed at the radius runout to the skin. SEM examination at a broken open region of this feature had identified smear and ductile dimples. Cracks up to 0.001” in depth were observed on the internal surface of the convex wall. The surface in this area had buckled and deformed likely during the event. The cracks spanned the deformed area of the wall (**Figure 65**).

2.3.4 **Midspan Crack IV – Cavity DF**

2.3.4.1 Visual and Binocular Review

Additional sections were prepared via wire EDM through the outboard midspan blade fragment to allow for visual access to each of the cavities as shown in **Figure 66**. Visual, binocular and FPI examination of each of the cavities identified two cracks – one at the forward spanwise rib in cavity DG and the other at the forward spanwise rib in cavity DF. Both cracks were located just outboard of the inboard chordwise ribs (**Figure 67**). No fatigue features were observed after breaking open the crack in cavity DG (**Figure 68**). Fatigue features were observed on the broken open crack in cavity DF. A second crack on another plane was observed on the concave side of the bond line; this crack was cut into during lab fracture. The larger crack measured 0.033” in depth and the smaller crack on the concave side of the bond line measured 0.017” in depth (**Figure 69**).

2.3.4.2 SEM Examination

SEM examination confirmed that there were no fatigue features at the crack location in cavity DG. Similar to the force fractured area in cavity CE, areas of alpha grains, one to two grains deep, were observed along the cavity surface. The remainder of the force fractured surfaces exhibited ductile dimples typical of overstress (**Figure 70**). SEM examination of the broken open cracks in cavity DF identified multiple origins along the rib surface. The primary origin, associated with most of

the crack progression, was located 0.020" from the bond line on the convex side of the rib. The origins were surface grain origins; no featureless facets or striated grains were observed at the origins and there did not appear to be MTRs associated with the origins (**Figure 71**). The crack progression exhibited predominantly faceted growth. Some areas exhibited crystallographic growth and there were isolated grains with striated/slip features with very fine spacing. These striated/slip features varied in directionality. Banding was observed on some faceted grains. These fatigue features indicate low delta K cracking (**Figure 72**). The smaller crack on the concave side of the rib exhibited a single surface origin and a similar mode of cracking; predominantly faceted growth, some areas that exhibited crystallographic growth, and isolated grains that exhibited striated/slip features with very fine spacing and variation in directionality (**Figure 73**).

2.4 Additional Small Fan Blade Fragments

Several additional small fan blade fragments were recovered, all measuring less than 2" x 2". The fragments exhibited significant secondary damage and it was unclear which part of the blades most of the fragments were originally from (**Figure 74**).

2.4.1 Midspan Crack II – Mating Half

2.4.1.1 Visual and Binocular Review

Binocular review identified remnant fatigue features on one of the fragments. Further evaluation found that this fragment was from cavity CD and the fatigue features observed were the mating surface to the convex side of the midspan crack on the outboard blade fragment (**Figure 75**). The remaining fragment surfaces exhibited secondary damage and overstress features.

2.5 Fatigue Testing

Fatigue test coupons were machined from the convex and concave airfoil sides of the root fragment of the event blade S/N CBDUAU9992 to determine if the fatigue performance of the part internal surface had been degraded. Krouse bend testing was used to produce S-N curves at R=0.4 and room temperature. The baseline curve was made up of two components –as-machined bulk specimens from the event fan blade, CBDUAU9992, and legacy data representing the typical clean or non-contaminated surface condition from a previously tested PW4000 fan blade, S/N CBDUAY1357. Fatigue testing of baseline samples showed results similar to legacy uniaxial fatigue of Ti 6Al-4V plate also tested at R=0.4 and room temperature, validating the bend test set-up and procedure. The samples representing the as-produced cavity surface from the root of the event blade exhibited significantly lower fatigue capability than the samples machined from the bulk. The fatigue curve results are shown in **Figure 76**. SEM examination of the samples tested at higher stress levels found multiple origins from the cavity surface side and some of the samples exhibited secondary cracks adjacent to the fracture.

2.5.1 Bend Test

A strain to failure bend test was completed to prove that there were no pre-existing cracks on the internal surface of the blade which would have invalidated the fatigue test results. A section of cavity FA surface was removed from the concave side of the blade. It was sliced to a thickness of

approximately 0.050” via wire EDM and then it was heat tinted in a furnace until the surface appeared gold. The sample was then bent until fracture. There was no heat tint on the fracture surface or on the winked open secondary cracks, indicating that there were no pre-existing cracks (**Figure 77**).

SEM examination of the fracture surface identified a faceted region a few grains deep along most of the surface of the bent sample. The faceted area extended up to 0.0024” from the surface, a depth similar to that observed in the etch effect observed in previously evaluated metallographic sections. The secondary winked open cracks were also faceted. Many origins were observed, most of which were surface origins. A few featureless facet origins were observed (**Figure 78**).

2.6 Characterization

To evaluate for detrimental surface conditions, several characterization methods were utilized to test the internal surface of the event fan blade.

2.6.1 Surface Roughness

Prior to metallographic sectioning of the origin area, surface roughness measurements were taken with a Mahr profilometer using a 4mm stylus chordwise along the surface just inboard of the fracture and spanwise along the adjacent cavity. Ra values ranged between 18 – 53 µin which met drawing requirements (**Figure 79**). Stylus and laser profilometry were used to evaluate surface roughness on fatigue test coupons. A specimen from the as-manufactured internal surface of the event blade, DA-CV-1, that exhibited low fatigue capability was compared to a fatigue test coupon from the as-manufactured internal cavity surface of reference fan blade, S/N CBDUAY1357, that exhibited fatigue capability consistent with legacy fan blade baseline capability. The stylus profilometry for both samples found Ra’s between 8 and 23 µin, which was within drawing requirements. The laser profilometry provided a surface roughness measurement (Sa). The baseline fatigue sample laser profilometry results were slightly higher in Sa compared to the event blade fatigue specimen results. Overall, these results suggested that the difference in fatigue capability was not the result of surface roughness (**Figure 80**).

Sample	Trial 1	Trial 2
CBDUAU9992 DA-CV-1 Stylus Profilometry	Ra = 16.4 µin	Ra = 22.4 µin
CBDUAU9992 DA-CV-1 Laser Profilometry	Sa = 65 µin	Sa = 63 µin
CBDUAY1357 Fatigue test – Stylus	Ra = 10.4 µin	Ra= 8.4 µin
CBDUAY1357 Fatigue test – Laser	Sa = 78 µin	Sa = 81 µin

2.6.2 **Hardness**

50g micro-hardness traces were taken from the cavity surface near the primary fracture origin into the material at 0.0005” increments. A slight increase in hardness within ~0.005” from the surface was observed (**Figure 81**). Vickers hardness measurements were also taken directly onto the surface of the flat fatigue test coupons with original event blade cavity surfaces (FA-CV-1, DA-CV-2, and DA-CC-1). For comparison, a machined bulk material coupon (EA-CC-3) was tested as well as a baseline surface coupon from CBDUA1357. Results showed that the event blade surfaces were harder than the machined and baseline blade surfaces (**Figure 82**).

Nanohardness trials using a diamond Berkovich indenter on an KLA Instruments™ Nano Indenter® G200 were completed on a cross-section through the baseline fatigue test coupon as well as DA-CV-2 from the event blade fatigue test coupons. A significant indentation size effect was seen in the analysis and consequently, caution was taken in converting the values directly to a Vicker’s hardness. DA-CV-2 showed a slightly harder surface layer that appeared to penetrate at least 25 µm (~0.001”) into the substrate. No evidence of a surface layer was observed in the baseline sample. Generally, the alpha phase was found to be harder than the transformed beta phase.

2.6.3 **Wet Chemistry - Bulk Chemical Composition**

Chemical composition on the bulk material was completed using LECO elemental analysis on a section from the 1” slice that was removed from the fracture surface. The chips used were from near the LE just inboard of the fracture surface (**Figure 83**). The chemical composition of the bulk material conformed to the Ti 6Al-4V specification.

2.6.4 **Advanced Characterization of the Surface Contaminant**

The blade failure and the additional cracks observed were thought to be caused by a surface debit as exemplified by (1) the fractography which identified multiple origins and multiple cracks, (2) the fatigue results that showed lower fatigue capability for the event blade internal cavity surfaces, (3) the bend test that identified faceted grains along the internal surface before transitioning to ductile dimples, (4) microhardness results which showed a slight increase in hardness within 0.005” of the internal surface, and (5) light etching of the alpha grains within 0.003” of the internal surface when etched with 1% HF. Advanced characterization techniques were needed to identify the elemental source of the surface contamination. Oxygen, carbon, nitrogen, and hydrogen are the primary titanium contaminants damaging to fatigue life and were therefore the focus of this effort.

2.6.4.1 XPS

X-ray photoelectron spectroscopy (XPS) was initially completed on a cavity FA rib surface, approximately 1 inch below the fracture surface (metallographic section A in 2.1.1.3). The sample was broken out of the mount for XPS evaluation (**Figure 84**). An argon ion beam was used to iteratively remove material (sputter) and analyze the composition through the first ~70nm (0.0000027”) of the blade allowing for measurement of the surface oxide layers. An exemplar reference sample was used from an internal rib surface of a typical blade.

Results showed a titanium oxide layer along the surface, which was less than 60nm deep and not significantly different from the reference sample. Titanium alloys react readily with oxygen and typically exhibit a very thin oxide layer on the surface. The peak oxygen concentration was observed at the surface and decayed within ~50nm to a background level. The event blade profile

was slightly higher than the reference, but the depth of oxygen penetration was still far below levels associated with an alpha case. The peak carbon concentration was observed at the surface, which decayed within ~50nm to a background level. The event blade carbon depth profile was consistent with the reference. The nitrogen depth profile was flat and at a low level, as was sulfur, both of which were consistent with the reference. There was a slight surface peak for fluorine, which decayed to a background level within ~10nm, and was consistent with the reference. There was a slightly higher level of silicon associated with the event blade vs. the reference, which decayed to a background level within ~30nm.

Follow up XPS analysis was completed on the cavity FA surface near the origin area of a secondary chordwise crack (**Figure 85**). This sample exhibited a carbonaceous layer that dominated the composition for the first ~40nm of the surface before titanium became the dominant element. Titanium metal is highly reactive when exposed under vacuum, so the ion beam sputtering process used to iteratively remove nanometers of material and analyze the near surface resulted in a lingering amorphous and carbide carbon signature. The distribution of carbon bonding states was not consistent with adventitious carbon (carbon associated with atmospheric contact). Following XPS, SEM examination identified carbon rich deposits of varying size decorating the surface of interest as well as an adjacent lab cut surface, indicating that they were introduced after sectioning. These carbon rich regions were not displaced or dissolved during ~2min of ultrasonic exposure in ethanol which was the cleaning procedure prior to XPS.

Additional XPS analysis was conducted at a second fatigue origin, adjacent to a secondary flowpath crack just outboard of the primary origin (**Figure 86**). SEM examination prior to the XPS was performed to confirm the surface was relatively free from carbon contamination. The oxide layer at the surface was estimated to be ~25nm deep, which was consistent with prior samples and did not suggest an alpha case layer. The carbon levels were consistent with the baseline sample and suggestive of adventitious carbon. These results suggested that the high carbon levels observed previously were likely the result of surface contamination during sample preparation or handling. Overall, the elements detected compared favorably with the exemplar sample. The XPS results did not detect a significantly high surface chemistry gradient at the surface that would have affected fatigue capability.

2.6.4.2 GDMS

Glow discharge mass spectrometry (GDMS) trials were conducted because of the technique's ability to detect trace elements such as carbon and oxygen using depth profiling. Oxygen and carbon contaminated standards were created by diffusing the contaminants into machined Ti 6-4 surfaces via heat treating at simulated blade manufacturing conditions. These intentionally contaminated samples were then used to test the feasibility of advanced characterization techniques in identifying oxygen and carbon surface gradients. GDMS was able to identify a gradient in the oxygen contaminated sample however it was unable to quantify accurate baseline levels of oxygen in the bulk material away the surface (confirmed by LECO elemental analysis). GDMS testing was discontinued in favor of SIMS and EMP.

2.6.4.3 SIMS

Secondary ion mass spectrometry (SIMS) was used to further evaluate the concentrations of oxygen, carbon, and hydrogen. This method was chosen because of its high sensitivity to light

elements near the surface with spatial and depth resolution. Elements of interest (H, C, and O) were mapped in negative ion mode over a 256 x 256-pixel area at <1 µm spatial resolution using an elemental concentration far from the surface to act as the "bulk" value for measurement calibration. Again, the oxygen and carbon contaminated standards were used to test the feasibility of the method. SIMS was able to detect a concentration gradient in both the O and C standards consistent with the expected depth however at concentration levels that were lower than expected.

SIMS testing was completed on a cross-section near an origin on the event blade. The sample chosen was a planar polish into a flowpath secondary chordwise crack (Reference Section 2.1.2.3). Two iterations of polishing and EBSD were previously completed on the sample as well as a 1% HF etch that was subsequently buffed off. It was broken out of the mount for SIMS analysis. Concentration line scans were taken over the width of elemental maps that were 200 µm wide for H, C, and O. SIMS did not detect significant surface concentration gradients for H, C or O. The runout concentration levels were within spec limits for Ti 6Al-4V blade alloy (**Figure 87**).

Additional SIMS testing was completed on a spanwise section through a flowpath secondary crack inboard of the fracture surface (Reference Section 2.1.2.3 and **Figure 31**). The analysis was completed adjacent to the larger of the two cracks. Data was along multiple line scans primarily staying within alpha grains. A carbon gradient, approximately 7µm (~0.0003") deep, was observed. The concentration at the surface was approximately 1 wt.% carbon (**Figure 88**).

2.6.4.4 EMP

Although electron microprobe (EMP) is less sensitive to low concentration levels than SIMS, EMP can also perform depth profiles of elements such as Ti, Al, V, O and N from the surface. Multiple iterations of EMP traces into the material near the fracture surface and secondary flowpath cracks showed no detectable levels of nitrogen, aluminum or vanadium above the matrix alpha baseline and no significant differences in the oxygen levels between the sub surface and matrix alpha phases. Examples of these traces are shown in **Figures 89 and 90**.

Since no carbon in titanium alloy standards were available at the expected carbon concentrations, a series of carbon in iron reference samples were used to plot an EMP calibration curve in order to analyze carbon concentration in titanium. Using the same beam conditions as the calibration, analyses were performed at 10KV – 50nA with a ~2 µm (~0.00008") defocused spot for a distance of 200 µm (~0.008") at intervals of 5 µm (~0.0002") for the first 100 µm (~0.004") and 10 µm (~0.0004") thereafter attempting to stay in alpha grains as much as possible. Carbon contaminated Ti 6Al-4V samples were analyzed to test the feasibility of the new method. Two carbon contamination samples were produced; the heat treat cycle of the first sample replicated the final form step during blade manufacturing and the heat treat cycle of the second sample replicated processes prior to forming. EMP traces identified carbon gradients in the surfaces of both samples. The carbon gradient depth and magnitude of the second sample was larger than the first, which was consistent with the longer soak time and higher temperature of the processes prior to forming (**Figure 91**).

EMP of a spanwise metallographic section through secondary flowpath cracks (Reference Section 2.1.2.3) identified a carbon concentration gradient from the surface to approximately 0.006" (**Figure 92**). The gradient appeared more consistent with the first carbon sample that replicated the final form heat treat cycle. EMP carbon traces were completed on the secondary flowpath crack

EBSD origin sample that was previously evaluated using SIMS (Reference Section 2.5.4.3 and **Figure 87**). EMP did not detect a carbon gradient, consistent with the SIMS results which also did not detect a gradient (**Figure 93**). EMP traces at cavities BA and GA exhibited carbon gradients that were shallower than the carbon gradient observed at the origin location, suggesting that the amount of contamination varied within the blade (**Figure 94**). EMP carbon traces completed at the surface of a baseline surface fatigue test sample did not identify a carbon gradient, providing a strong correlation between carbon gradients found by EMP and fatigue capability. EMP traces from the sealed cavity on the event blade also did not show a carbon gradient at the surface, indicating that the carbon contamination was introduced after the fan blade bonding process, and likely occurred during the final blade forming process (**Figure 95**).

3.0 Details of Examination – S/N CBDUA49233 (Blade No. 18)

CBDUA49233 was the following sister blade to the event blade. It was labeled as blade #18 upon receipt. The blade measured approximately 26.5”x18” and weighed 25 lbs/11.3 kg. It fractured at midspan, approximately 26.5” above the root bottom. The root portion was still intact in the engine at disassembly. Visual and binocular review of the fracture surfaces identified features consistent with secondary damage and overstress. No fatigue-like features were observed. Two additional fragments were recovered from the ground and found to be remnants of this blade. The first fragment measured approximately 10.5” x 8.5” and weighed 2.3 lbs./1.0 kg. The second, smaller, fragment measured approximately 10”x6” and weighed 1.2 lbs./0.5 kg. The features on these fragments were also consistent with secondary damage and overstress (**Figure 96**).

4.0 Details of Examination – Sister Blades

The other blades in engine 777047, the “sister blades”, generally exhibited substantial airfoil impact damage, including heavy tip rub, hard body impact damage and buckled airfoil cavities which occurred following the primary fracture of fan blade S/N CBDUAU9992. Upon arrival at P&W, the sister blades were non-destructively inspected via TAI and UT where possible. UT inspection was not possible on areas that exhibited extensive secondary damage. The inspection results were compared to previous TAI results on the blade set, collected in 2014 and 2016. Six sister blades were submitted for destructive evaluation based on midspan indications found during the inspections (**Figure 97**).

Visual/binocular examination and FPI after sectioning did not identify crack-like indications at the TAI/UT indication locations on 5 of 6 blades. On those blades, bond line separation and adhered foreign material was observed. Destructive evaluation of a UT indication on blade S/N CBDUAW0148 revealed a fatigue crack from a scratch-like feature just outboard of the chordwise rib in cavity FH.

Although there were no crack-like UT or TAI indications in the flowpath on any of the blades, the cavity FA-EA rib, where the incident blade fractured, was removed for visual/binocular review, FPI, and structured light (blue light) evaluation on most of the blades that were destructively evaluated. Evaluation of the structured light data, with a focus on the transition radius at the forward side of cavity FA where the incident blade fractured, was completed by the P&W Engineering team.

Examination of the transition radius at the forward side of cavity FA on two of the blades identified irregular contours at the radius runout to the rib and shallow spanwise cracking, up to 0.003” in depth. The cracking was not well-developed, well-behaved fatigue cracking and was not consistent with the features observed on the primary cracks in the incident blade.

The root holes of 5 blades were sectioned to look for evidence of contamination on blades with similar bonding dates to the incident blade. Evaluation of the root hole sections etched with a 1% HF acid solution identified a surface layer up to 0.0001” in depth on each of the blades. The condition observed on the incident blade, light etching of the alpha grains near the surface, was not observed on any of the sister blades.

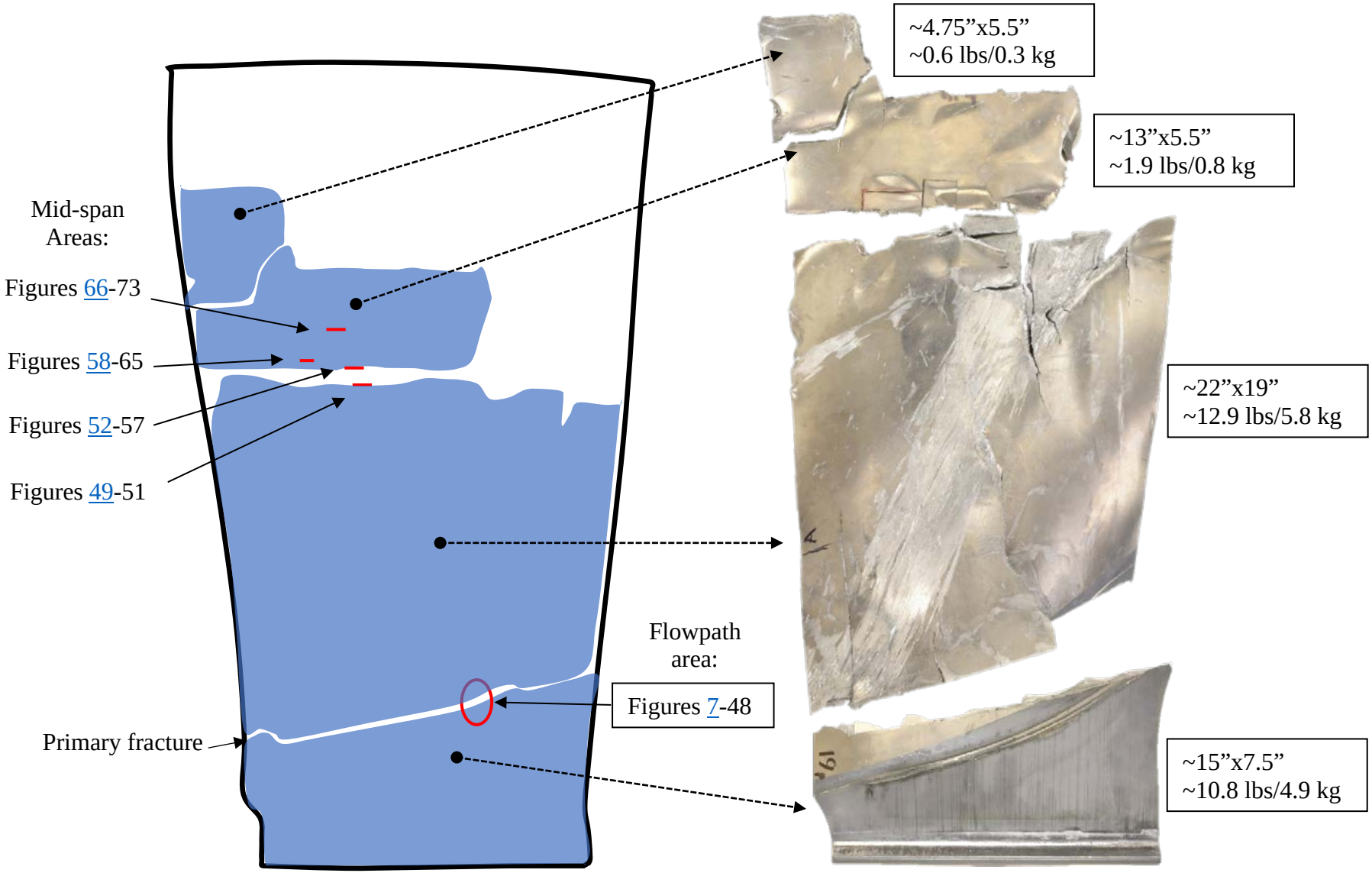

Figure 1: Diagram and images showing the recovered sections of the incident blade and fatigue fracture/crack locations (red circle indicating an area with multiple cracks and red lines indicating approximate locations of individual cracks on the diagram).

Figure 2: Images of the part markings observed on the root bottom of the fractured blade.

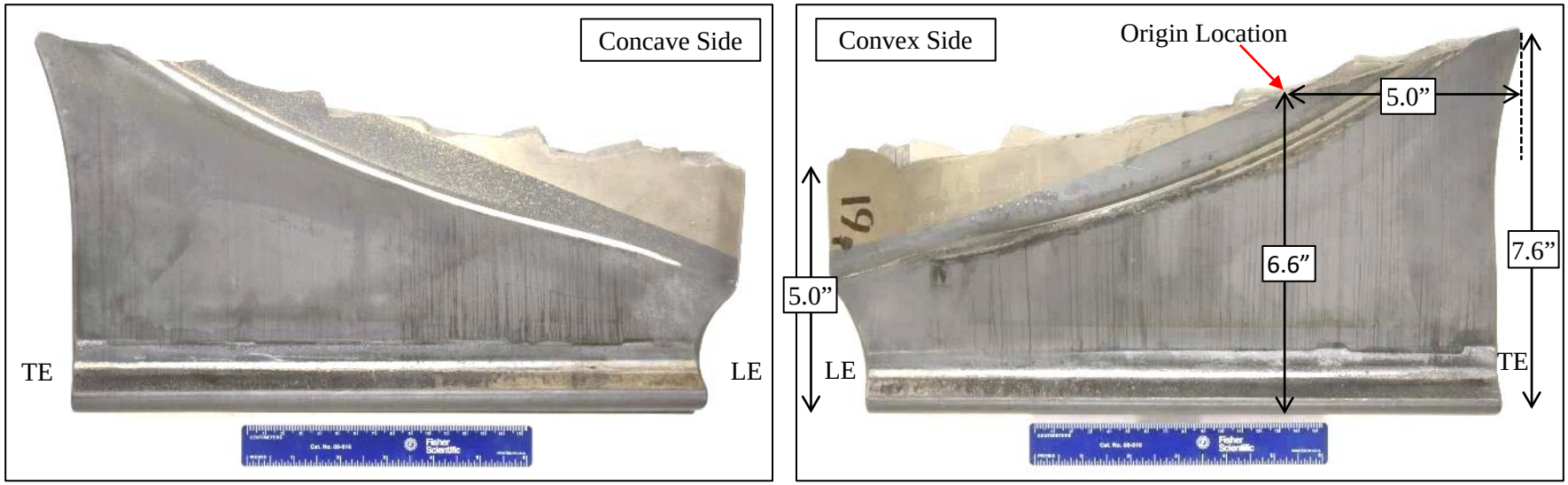

Figure 3: Overall images of the convex and concave sides of the fractured blade, CBDUAU9992. The fracture initiated approximately 6.6” outboard of root bottom and approximately 5.0” from the TE.

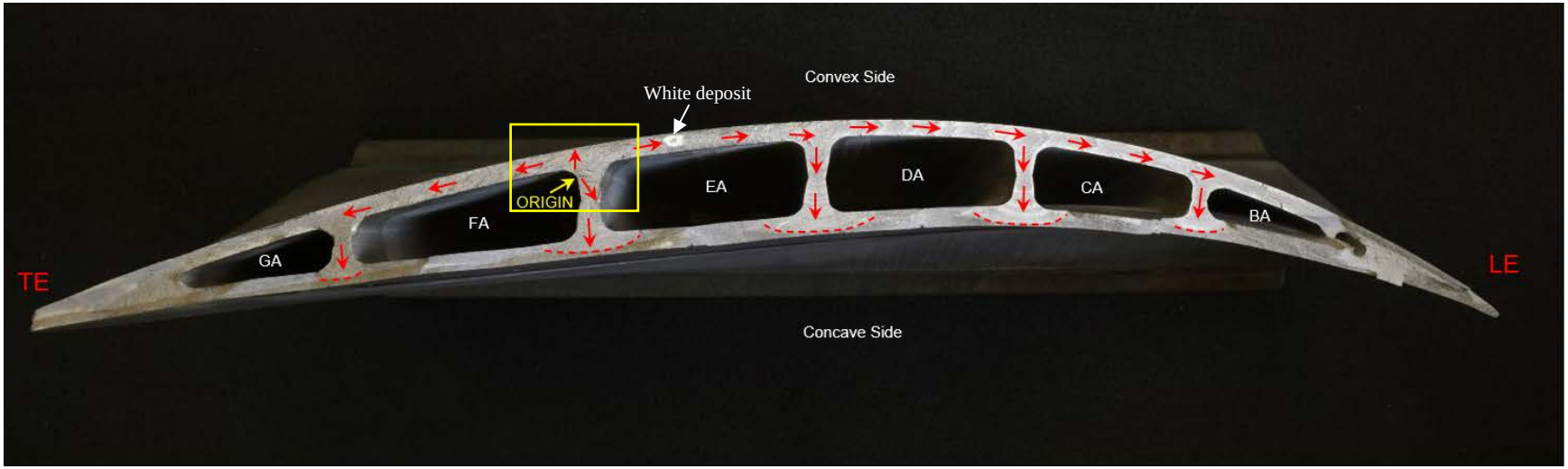

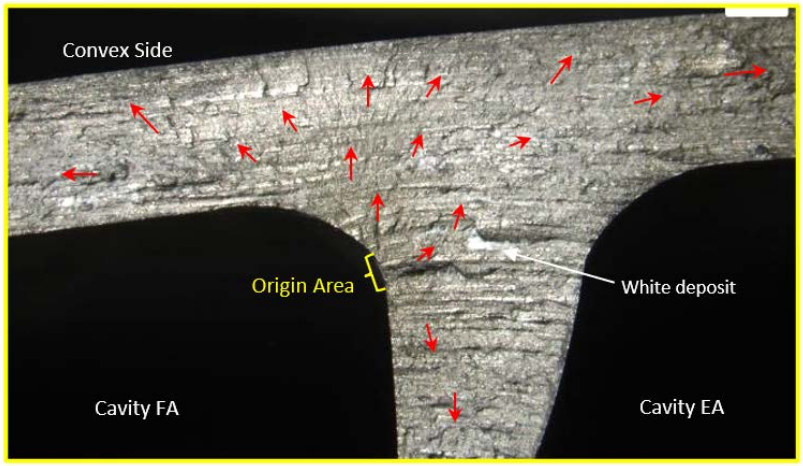

Figure 4: Overall and close-up views of fracture surface showing fatigue features propagating from an area located at the radius runout to the internal rib at the forward end of cavity FA. A white deposit was observed on areas of the fracture surface and on the internal cavity walls; this deposit was likely fire retardant used following the event.

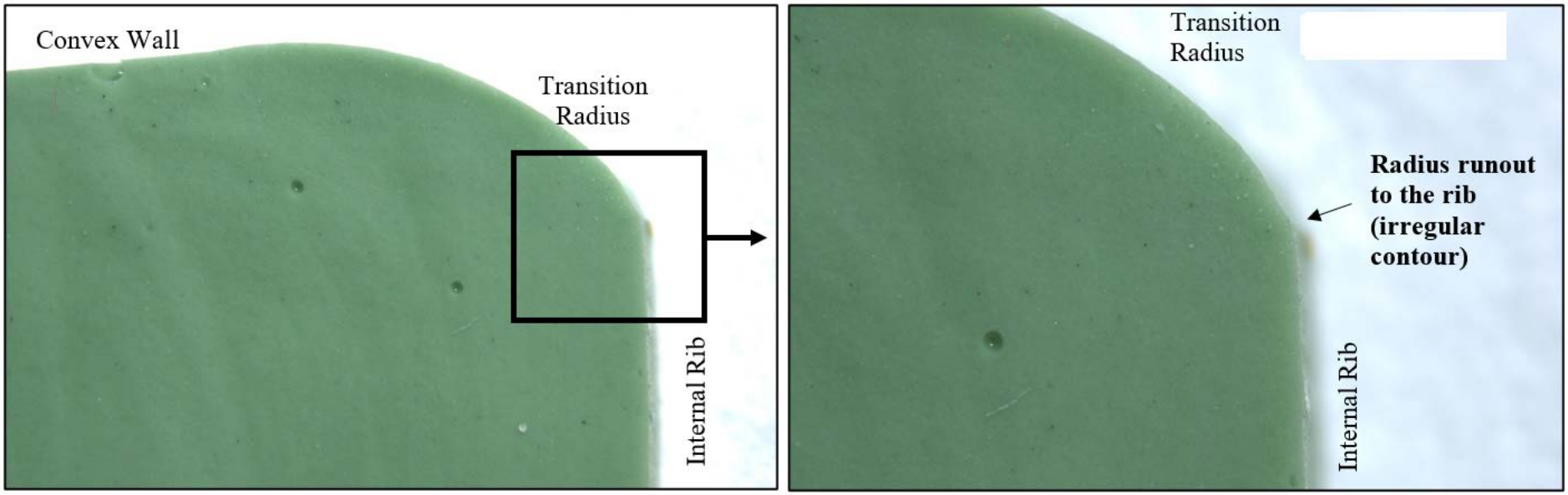

Figure 5: The transition radius between the internal rib and convex side wall in cavity FA was replicated inboard of the fracture location using rubber replicating material. The radius runout to the rib region exhibited an irregular contour (lack of tangency).

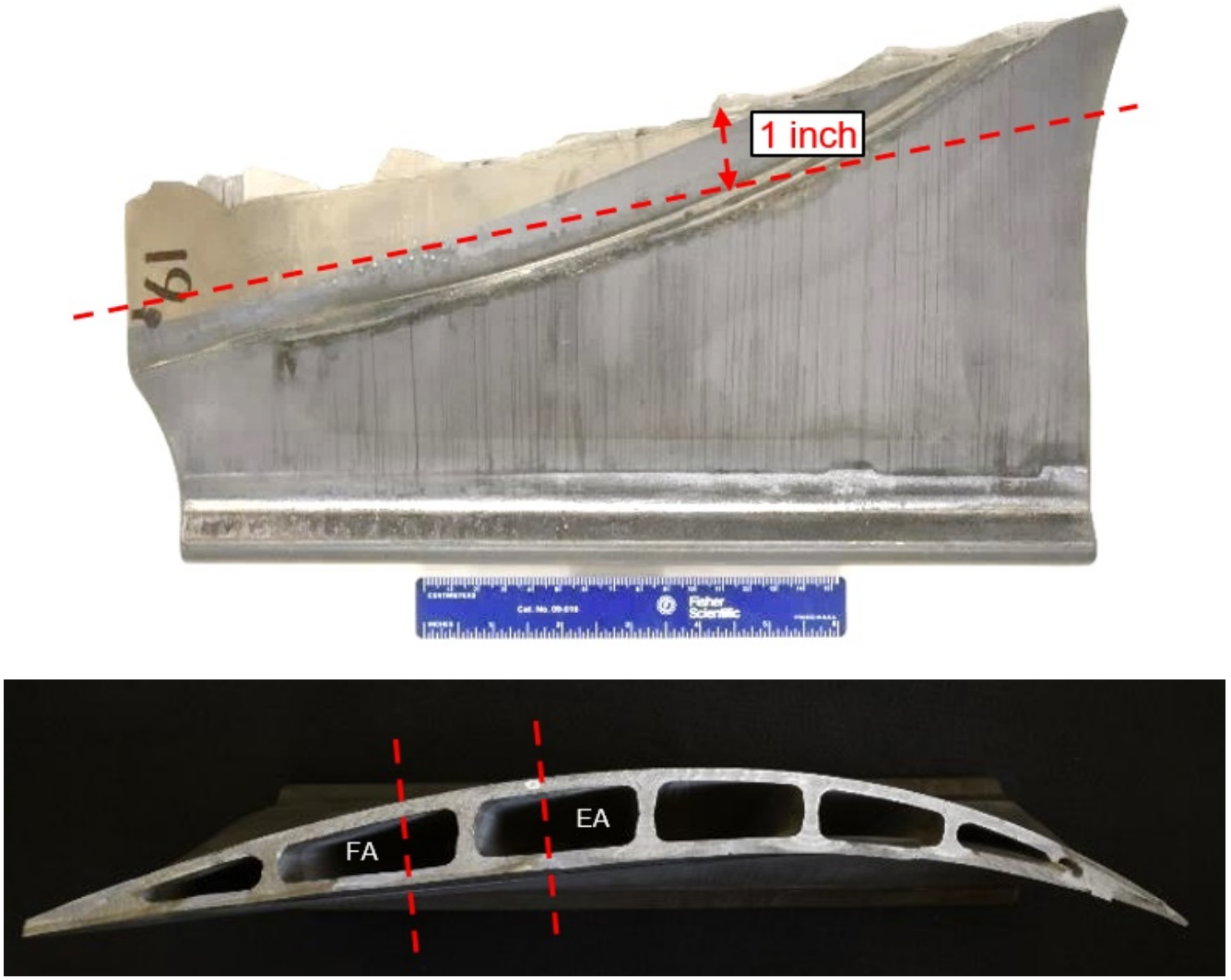

Figure 6: Images showing where the fractured blade was sectioned for further analysis (red dashed lines).

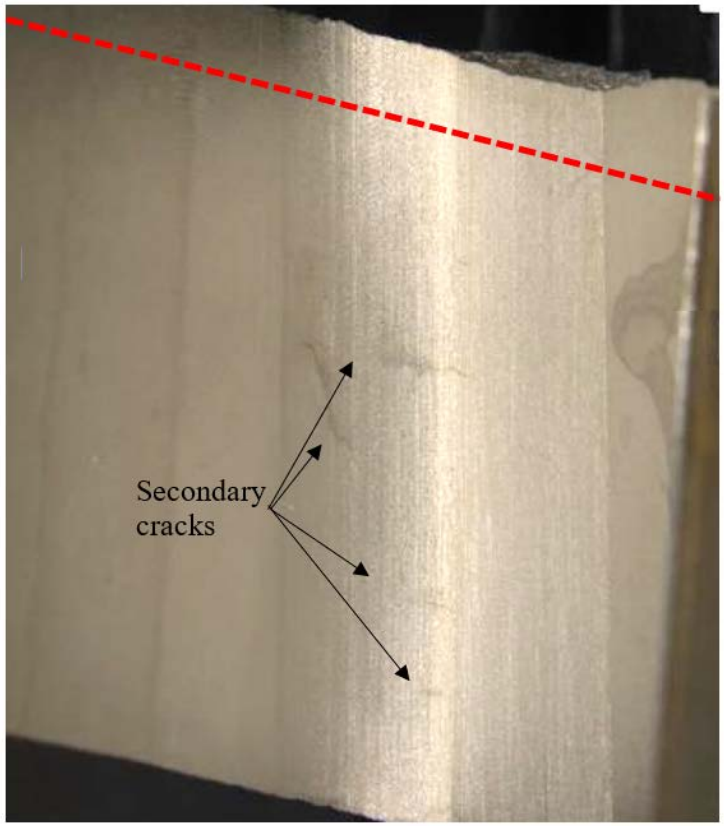

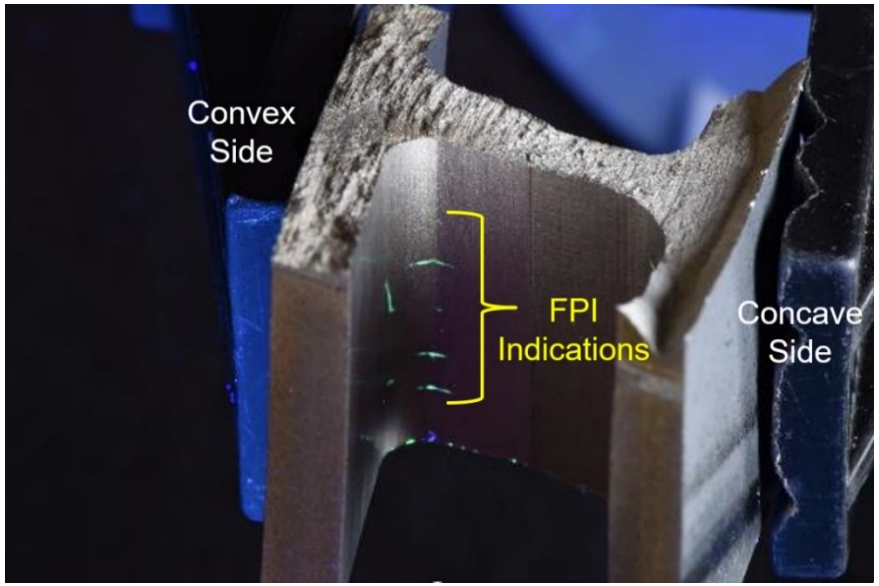

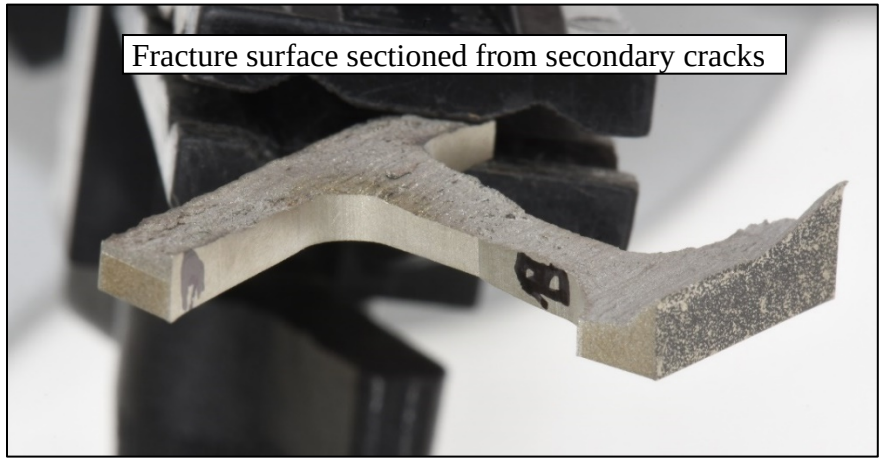

Figure 7: FPI and binocular examination identified multiple cracks inboard of the fracture surface. A section was made via wire EDM to remove the fracture surface from the secondary cracks for further evaluation (red dashed line).

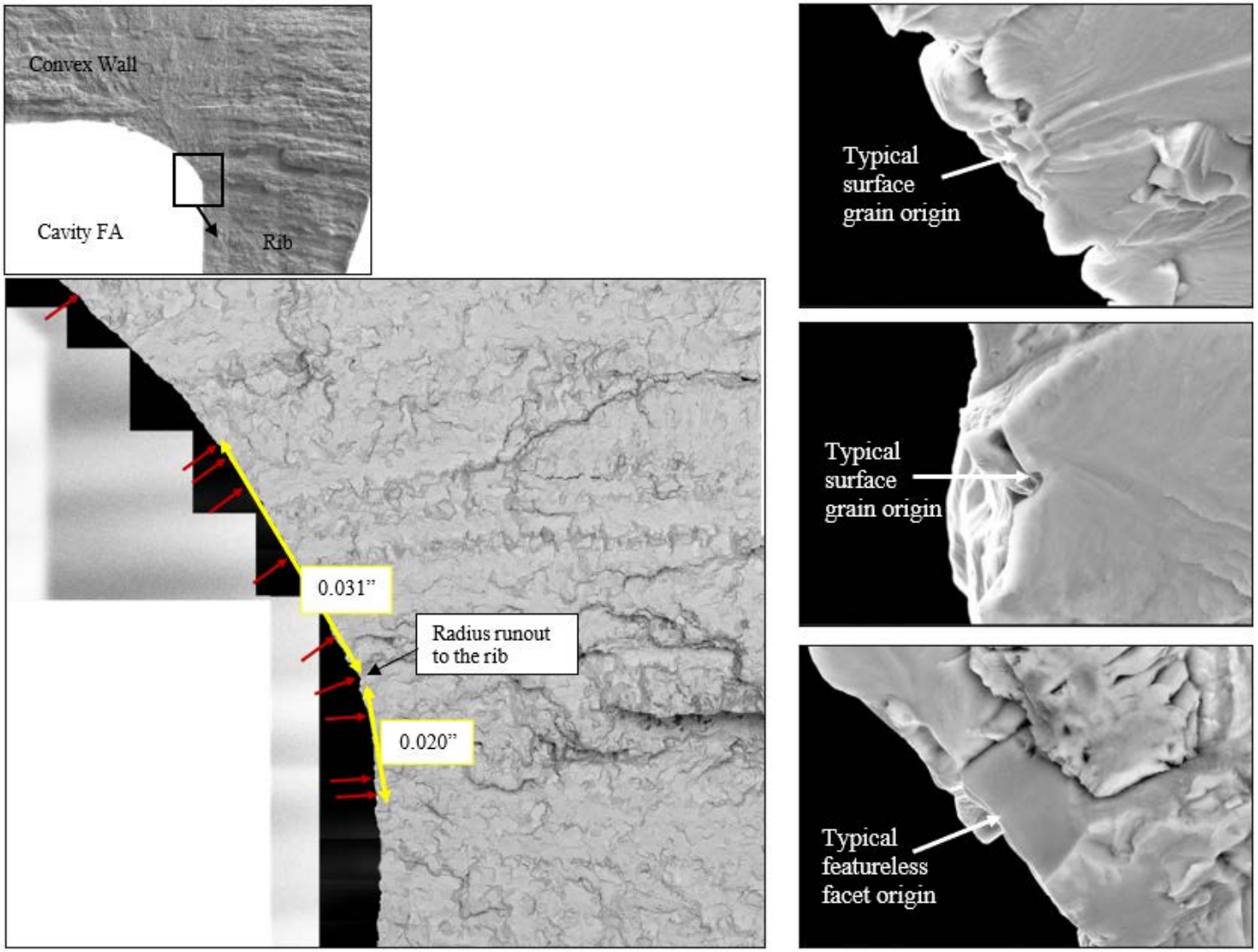

Figure 8: SEM images showing the origin locations (red arrows) and representative images typical of the surface and featureless facet origins observed.

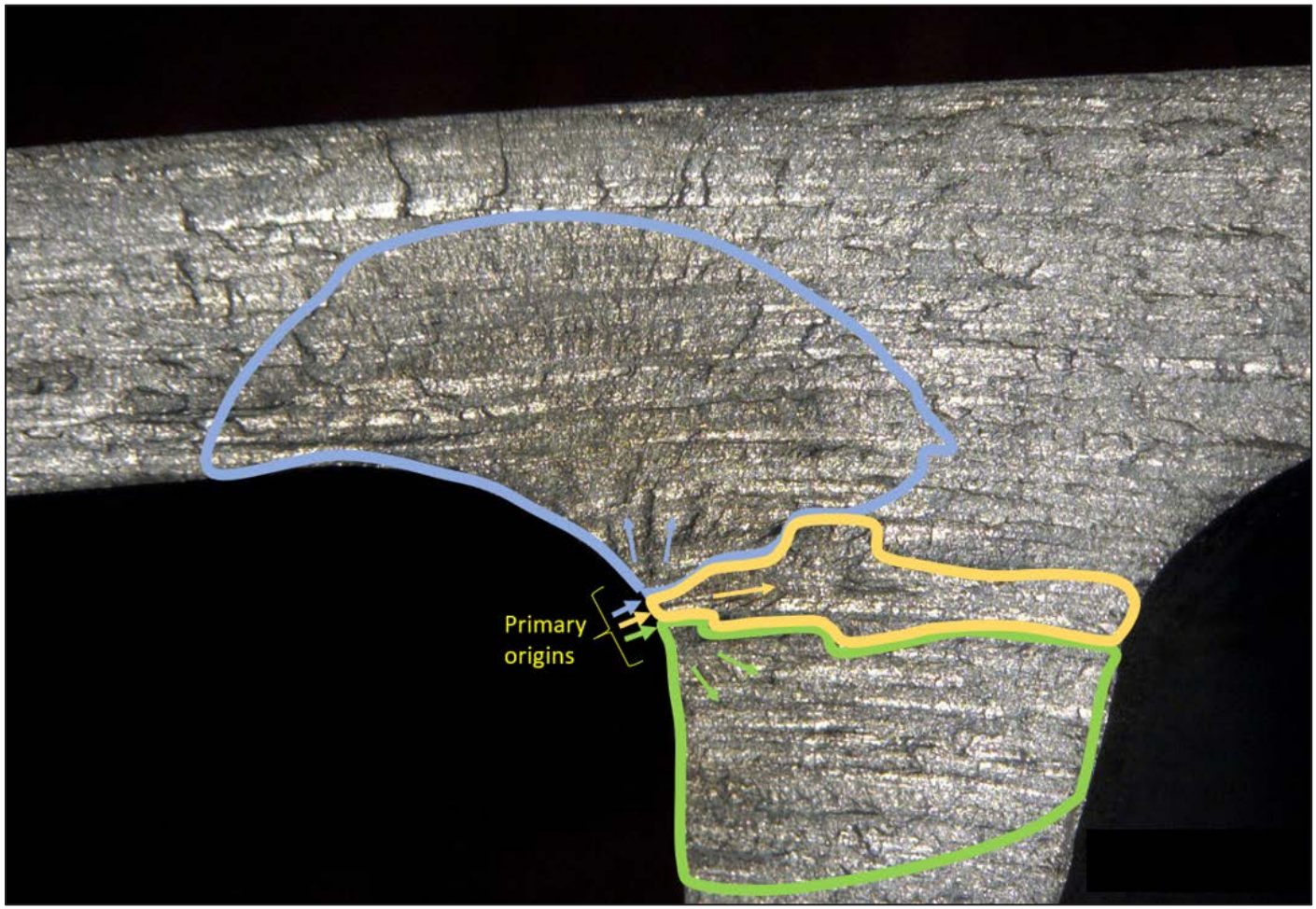

Figure 9: Image of the fracture surface showing the three primary origins (arrows) and the areas of the crack progression that are dominated by the corresponding origin (i.e. green origin was associated with crack progression in the area outlined in green). Areas outside of the indicated regions were not further evaluated.

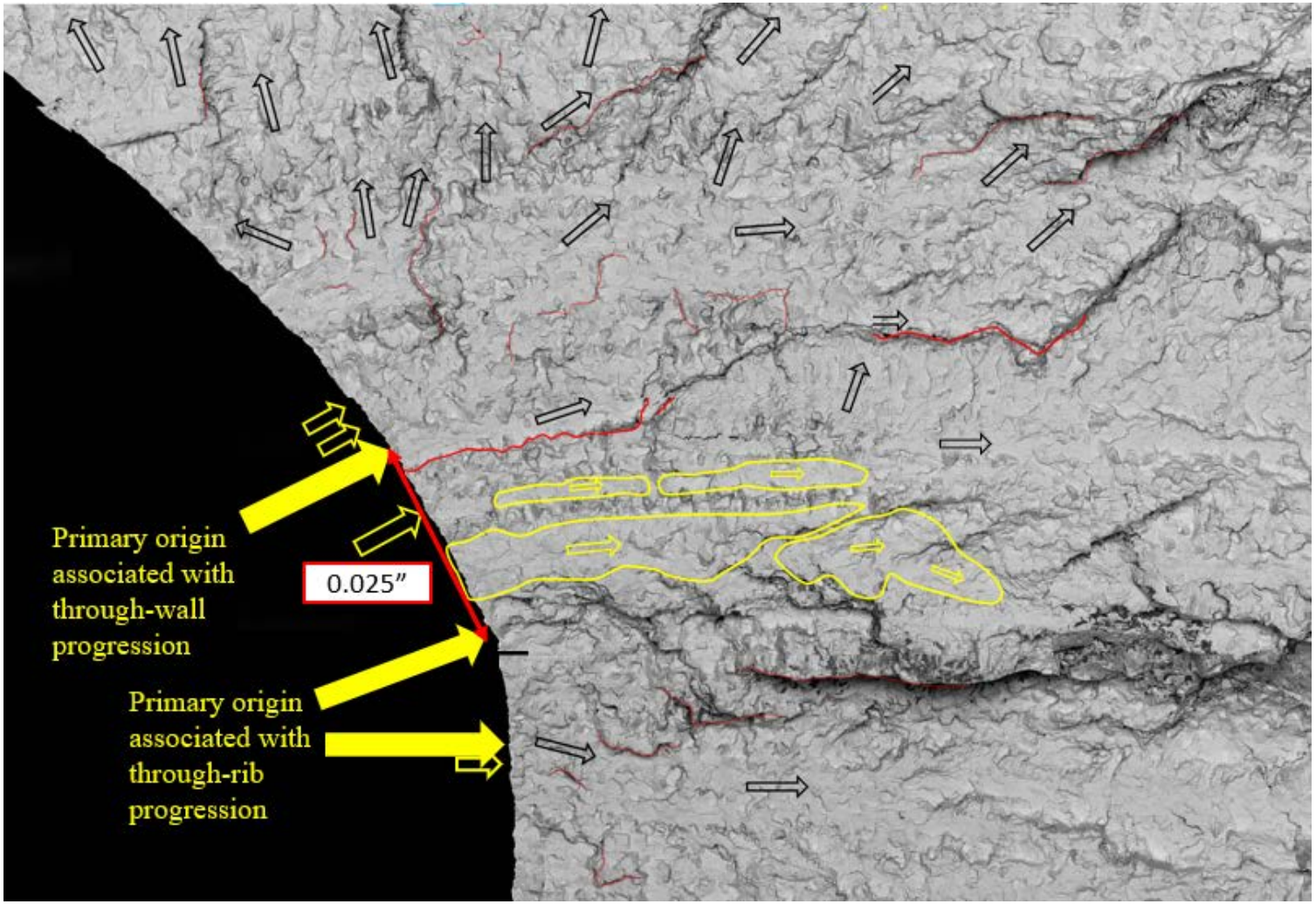

Figure 10: Image showing an annotated fracture map of the origin area. The three primary origins are indicated by bold yellow arrows. Other, relatively "weak" origins are indicated by outlined yellow arrows. Possible MTRs based on the fractographic features are outlined in yellow. The red lines indicate plane changes/separation in the fatigue regions.

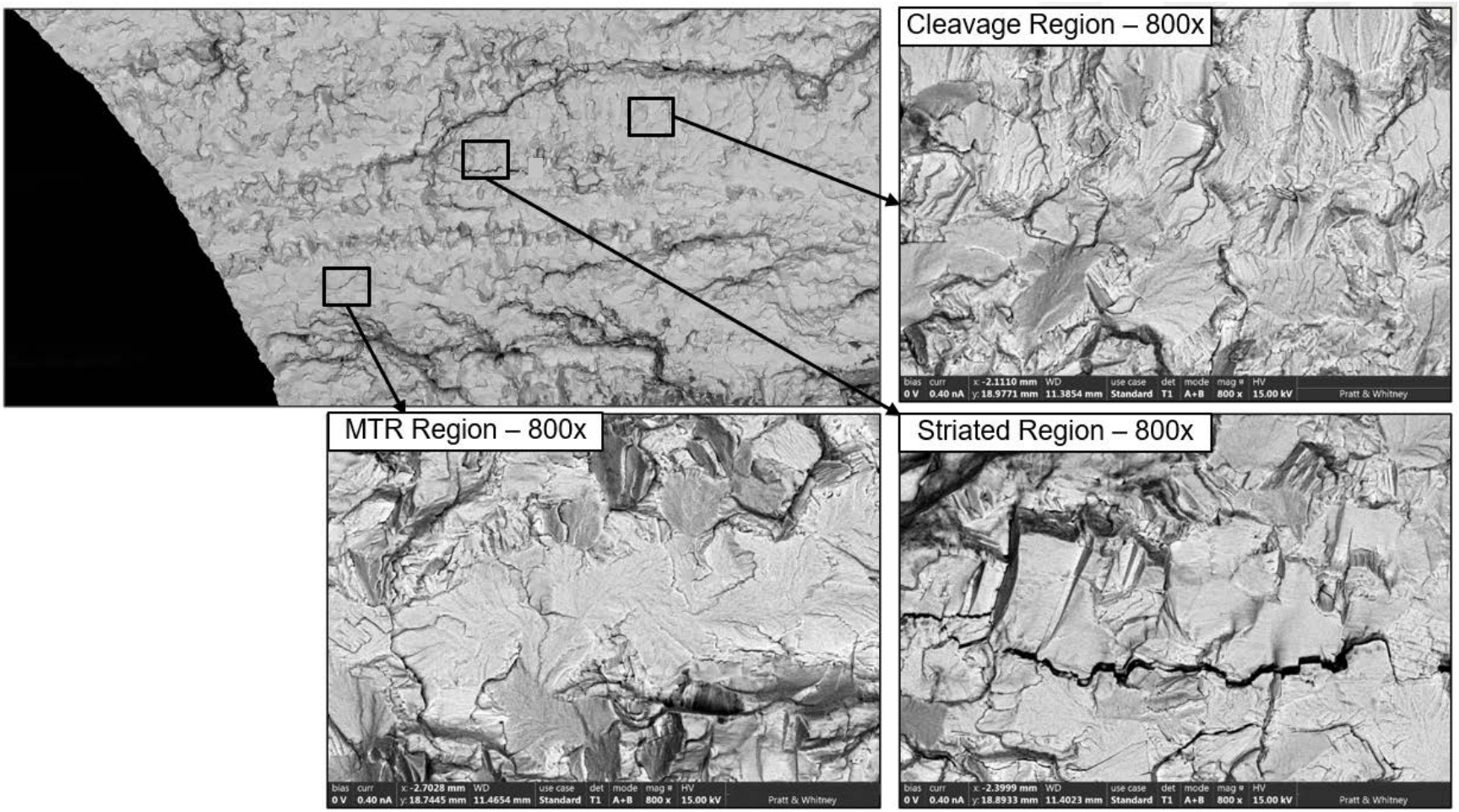

Figure 11: SEM images showing features representative of the early fatigue progression. Predominantly faceted growth with a mix of cleavage and striations was observed within 0.063" of the origin.

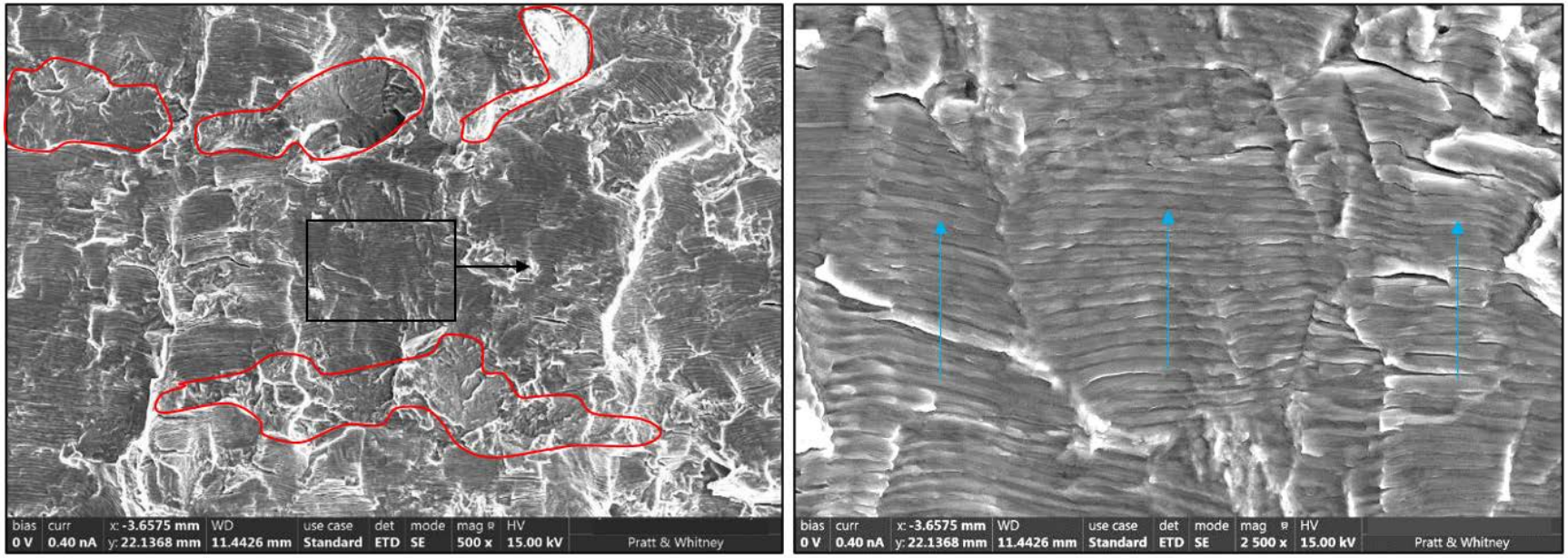

Figure 12: SEM images showing predominantly striated fatigue features with faceted growth mixed in (red areas), representative of the stable LCF region located 0.063” to 0.199” from the primary origin.

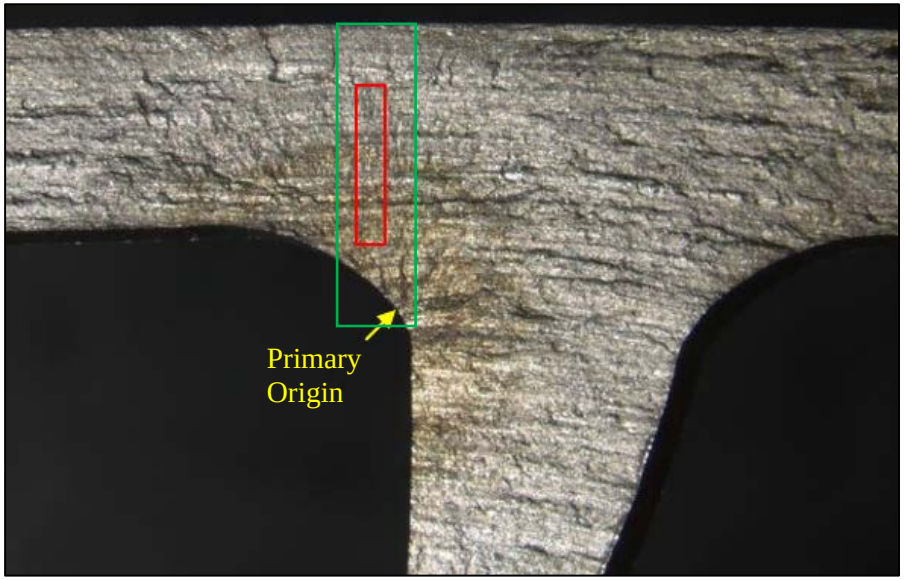

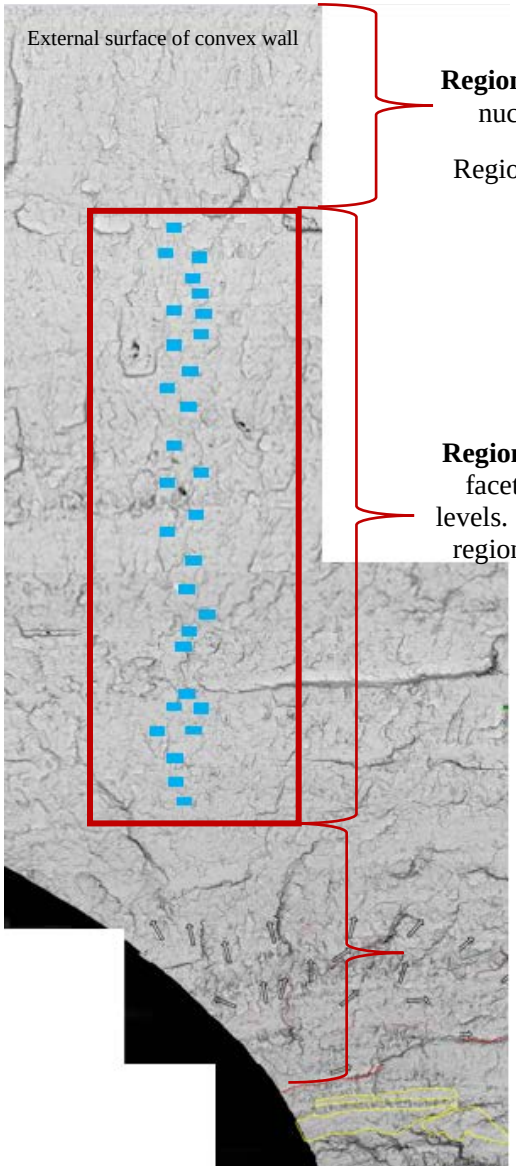

Region 3: Beyond separately nucleated MTR region.

Region omitted from count.

Region 2: Predominantly striated with faceted growth mixed in at varying levels. Striation count completed in this region (0.063” – 0.199” from origin).

Region 1: Predominantly faceted growth, isolated striations.

Region omitted from count.

Figure 13: Images showing the region where the striation count was completed (0.063” to 0.199” from the origin).

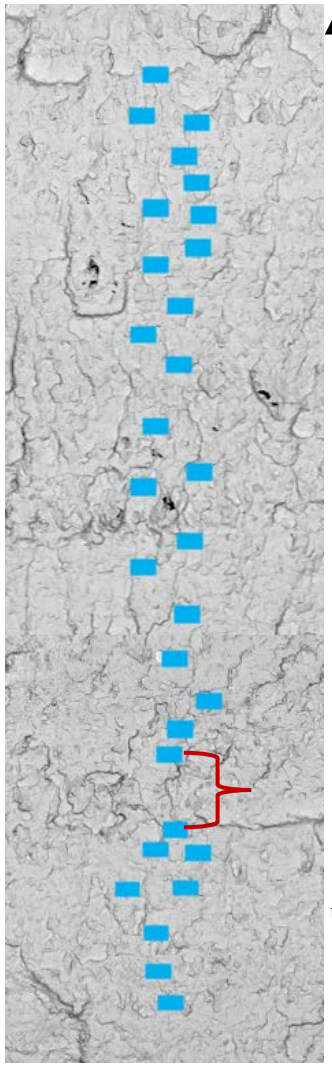

Figure 14: Image showing the striation count region. Points measured were represented by the blue boxes.

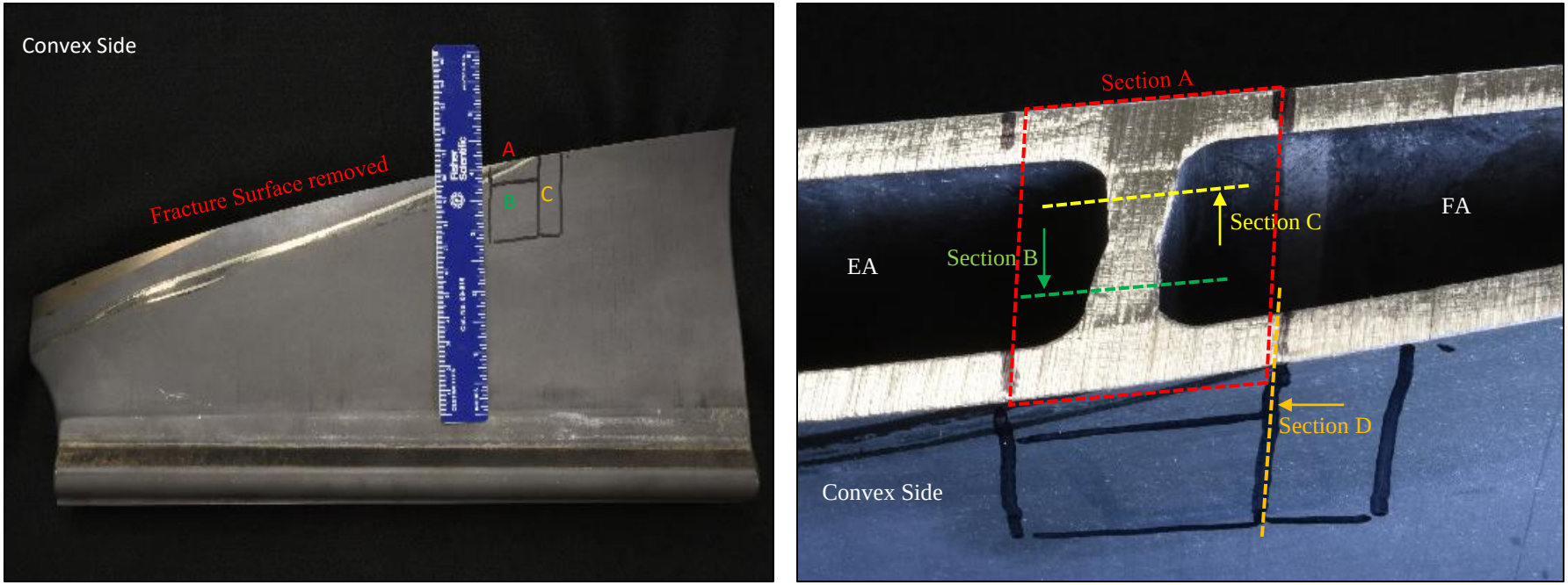

Figure 15: Images showing the locations of metallographic sections taken from the root, inboard of the fracture surface. The sections were prepared for initial evaluation of the bulk and surface microstructure.

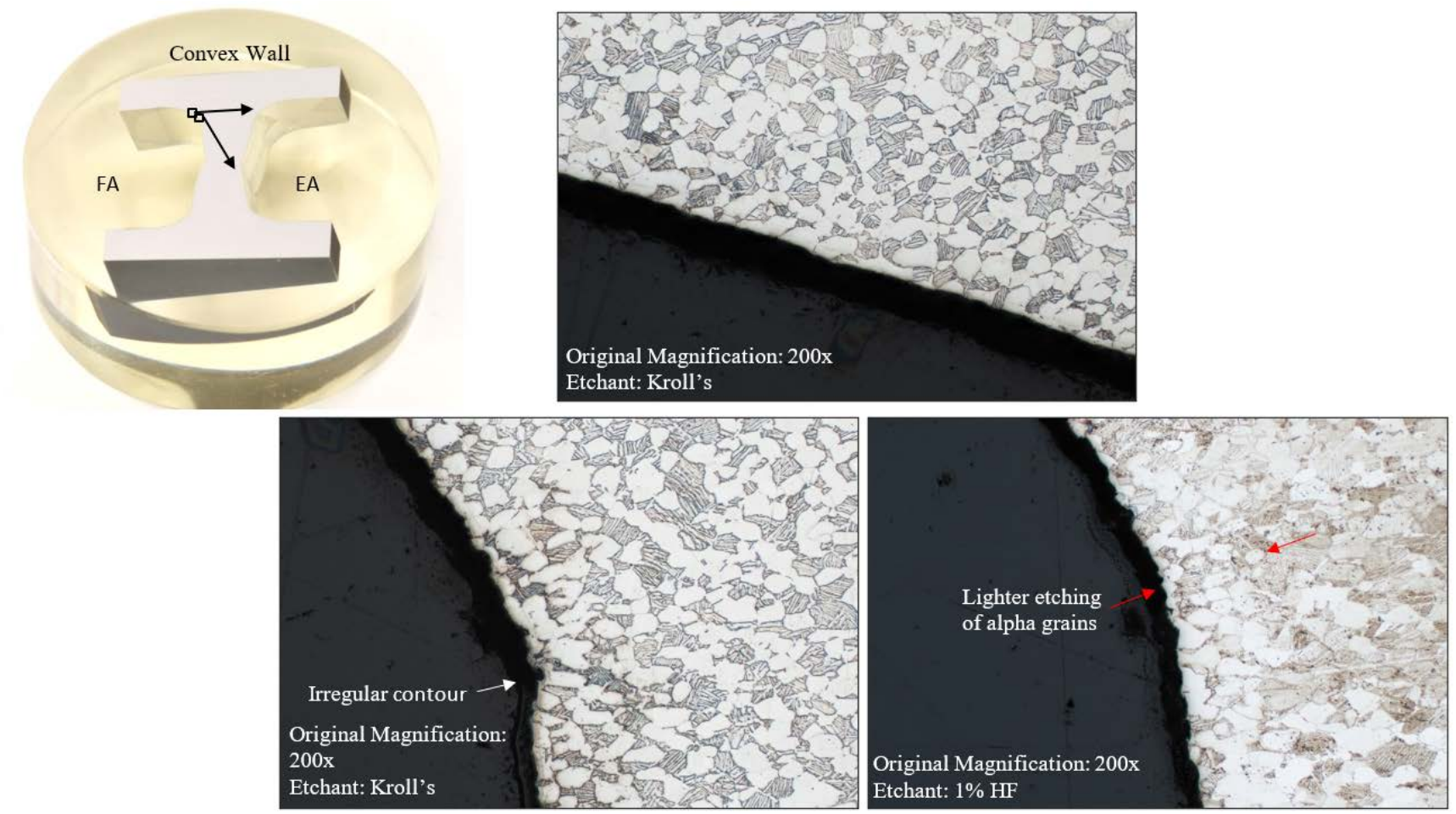

Figure 16: Images showing transverse section A into the ribs/walls approximately 1" below the fracture surface. The microstructure appeared typical, and no surface layer/deformation of the grains was observed. There was an irregular contour at the radius runout to the rib (left image). The alpha grains at the internal surface etched lighter when etched with 1% HF (right image).

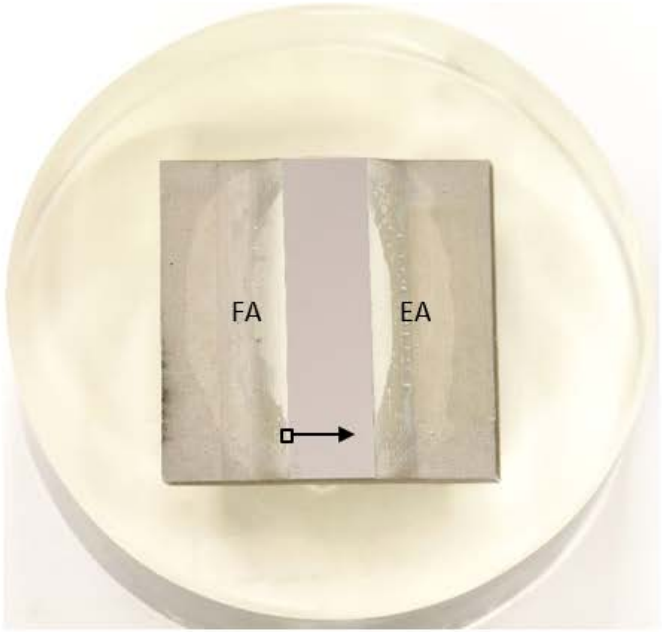

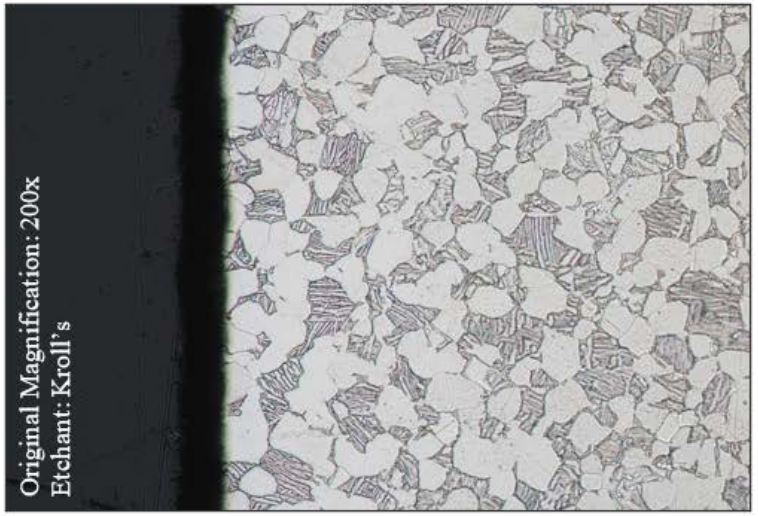

Figure 17: Images showing section B - a longitudinal section through the spanwise rib between cavities FA and EA on the convex side of the bondline, approximately 1.25" below the fracture surface. No surface layer/deformation or secondary cracks were observed. Alpha grains near the surface etched lighter when etched with 1% HF (top image).

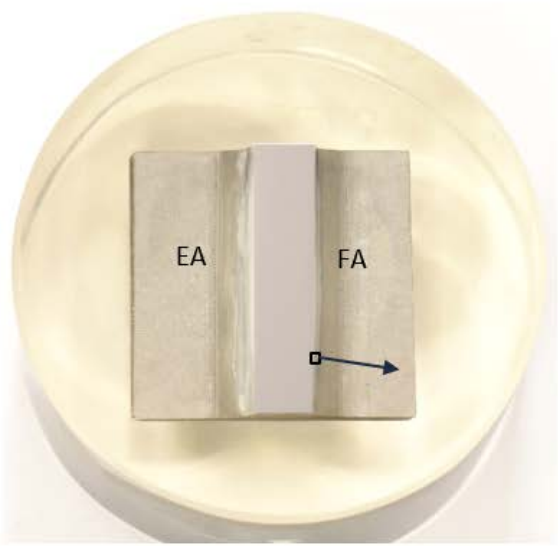

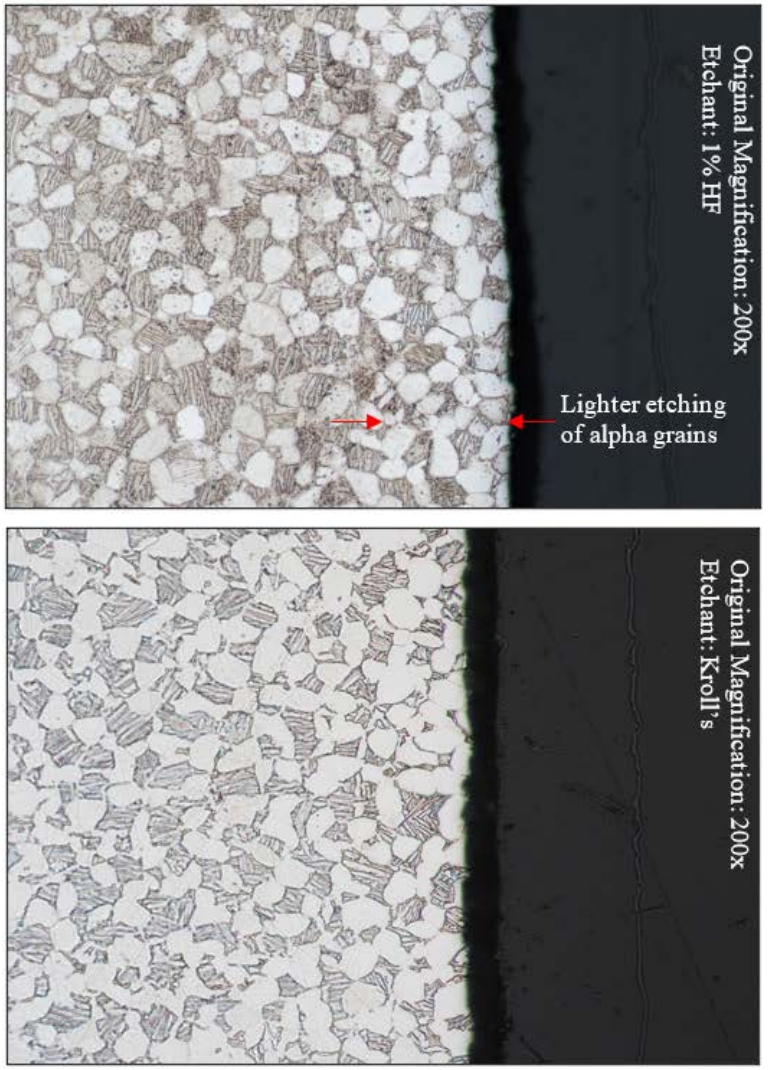

Figure 18: Images showing section C – a longitudinal section through the spanwise rib between cavities FA and EA on the concave side of the bondline, approximately 1.25" below the fracture surface. No surface layer/deformation or secondary cracks were observed. Alpha grains near the surface etched lighter when etched with 1% HF (top image).

Figure 19: Images showing section D – a longitudinal section through the convex wall in cavity FA, approximately 1" below the fracture surface. No uniform surface layer/deformation or secondary cracks were observed. Alpha grains near the internal surface etched lighter when etched with 1% HF (top image). The alpha grains at the external surface of the blade did not exhibit this condition.

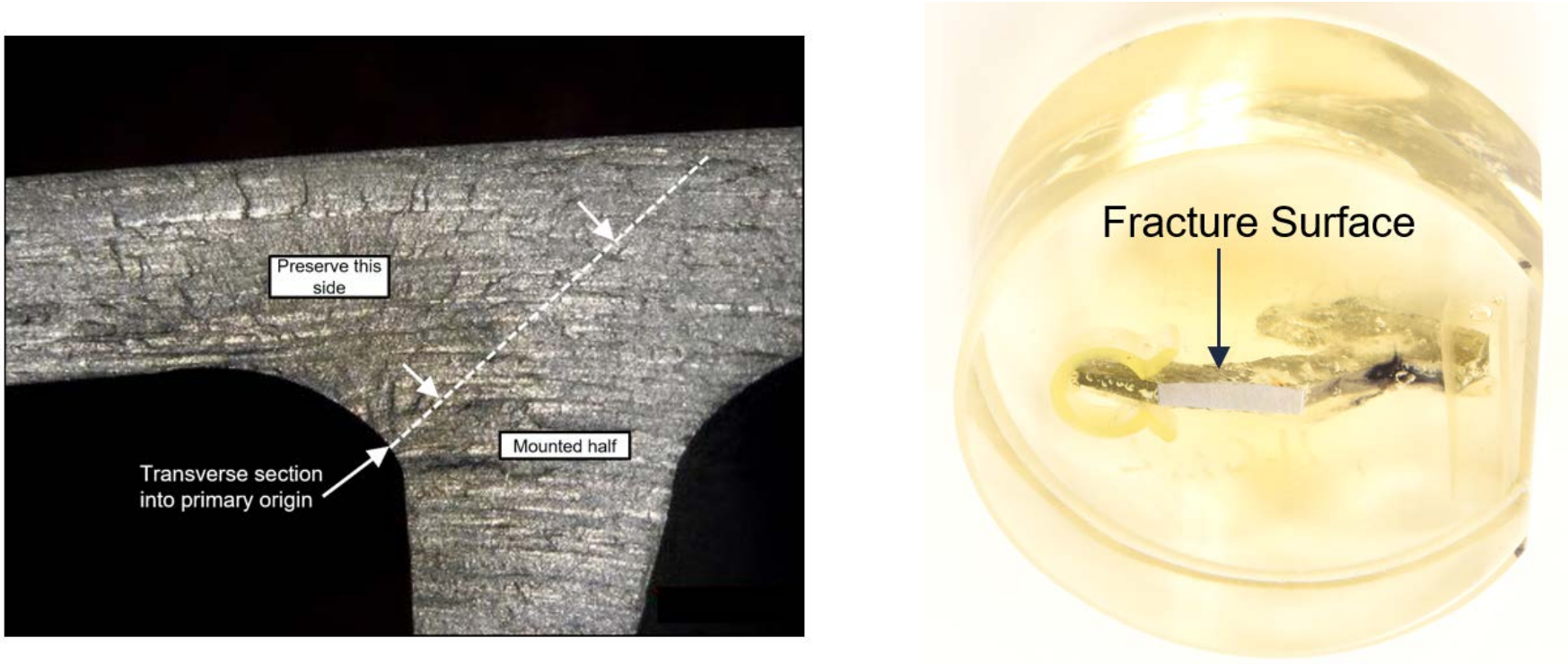

Figure 20: Images showing the location of the spanwise metallographic section through the origin. The white line in the left image shows the plane of polish and which side of the fracture was mounted.

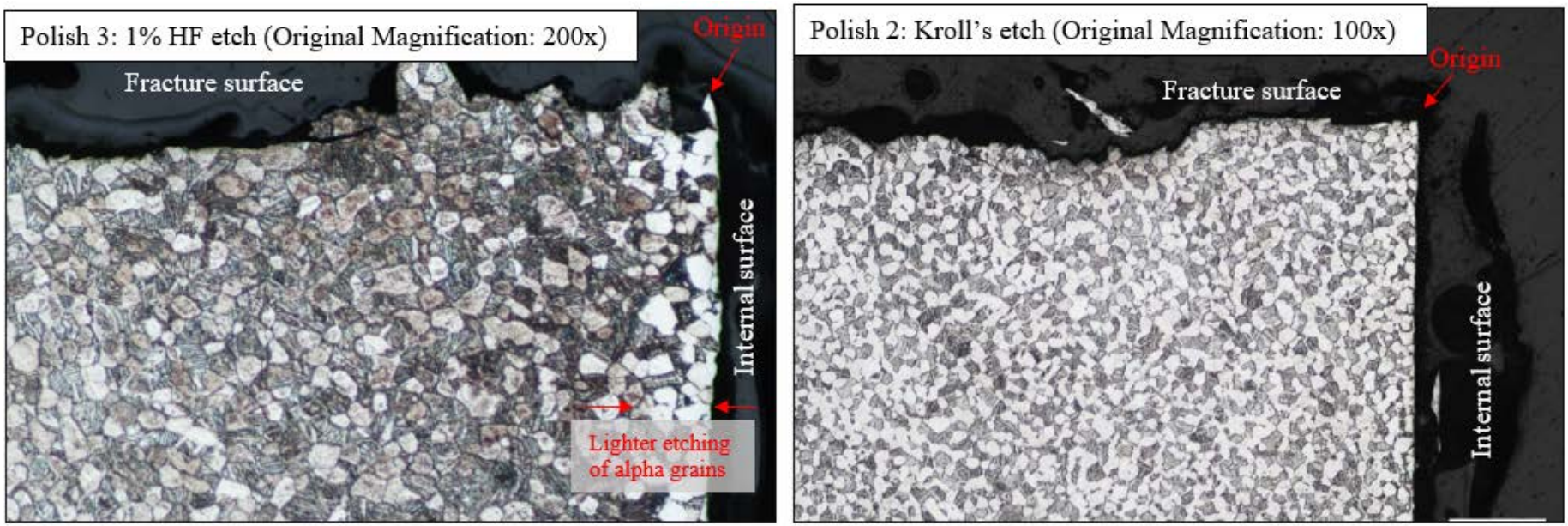

Figure 21: Three step polishes at 0.001" increments were made through the primary origin. 1% HF (left image) and Kroll's (right image) etches were completed at each increment. Representative images of each are shown above. Alpha grains near the surface etched lighter when etched with 1% HF. No distorted surface layer/deformation was observed.

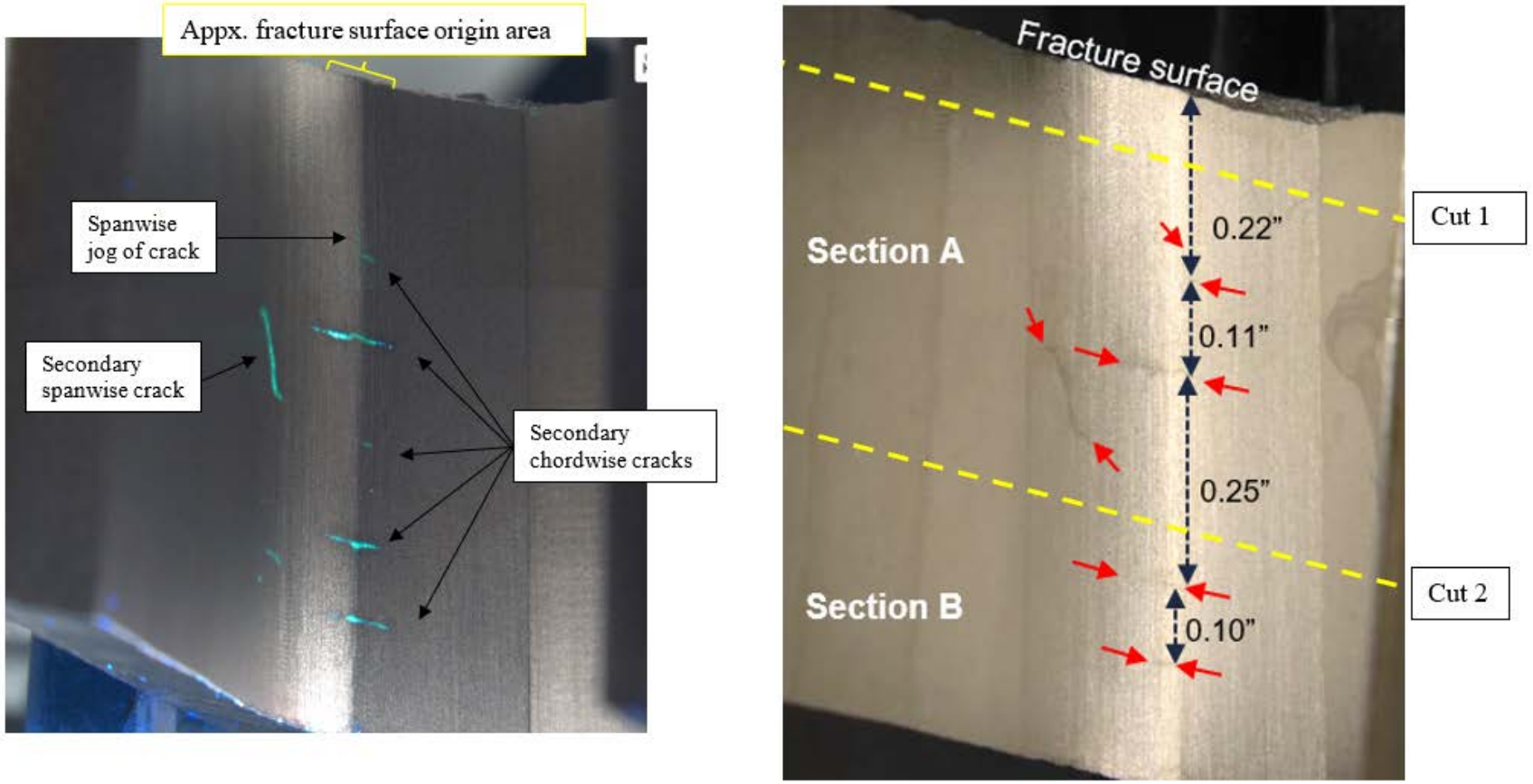

Figure 22: Images showing multiple secondary cracks within 0.68” inboard of the fracture surface (red arrows indicate the ends of the cracks). Multiple mostly-chordwise oriented cracks, parallel to the fracture surface, were identified in the transition radius between the convex wall and the internal rib at the forward end of the FA cavity which aligned with the origin area on the fracture surface. After sectioning the fracture surface from the secondary cracks (cut 1), an additional section along the yellow dotted line (cut 2) was made via wire EDM to prepare for metallography on the two cracks furthest from the fracture surface (section B).

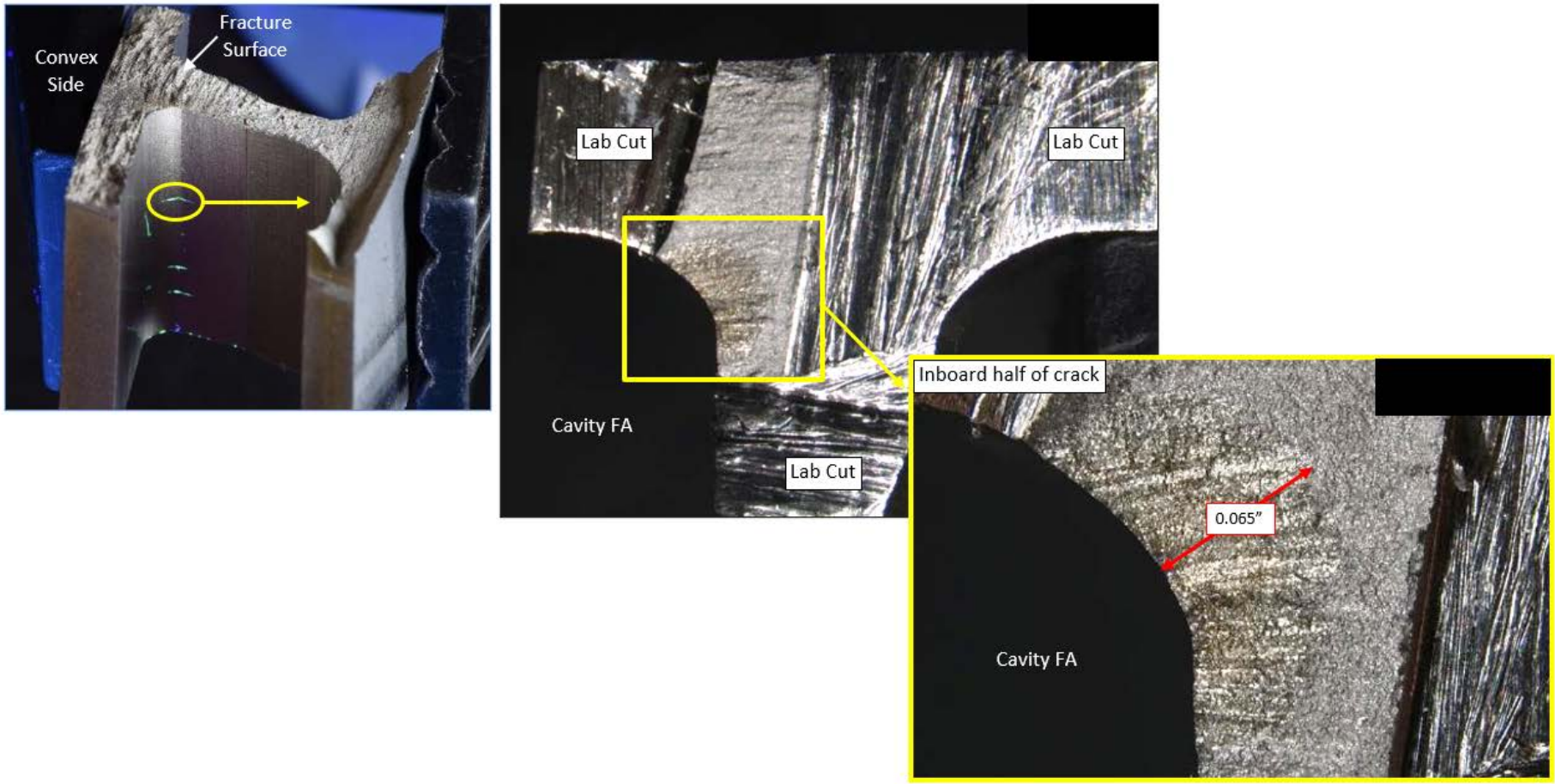

Figure 23: The largest of the secondary chordwise cracks inboard of the fracture surface was lab fractured open. The maximum crack depth measured 0.065”.

Figure 24: Images of the outboard half of the broken open secondary chordwise crack showing an additional crack plane near the radius runout to the rib.

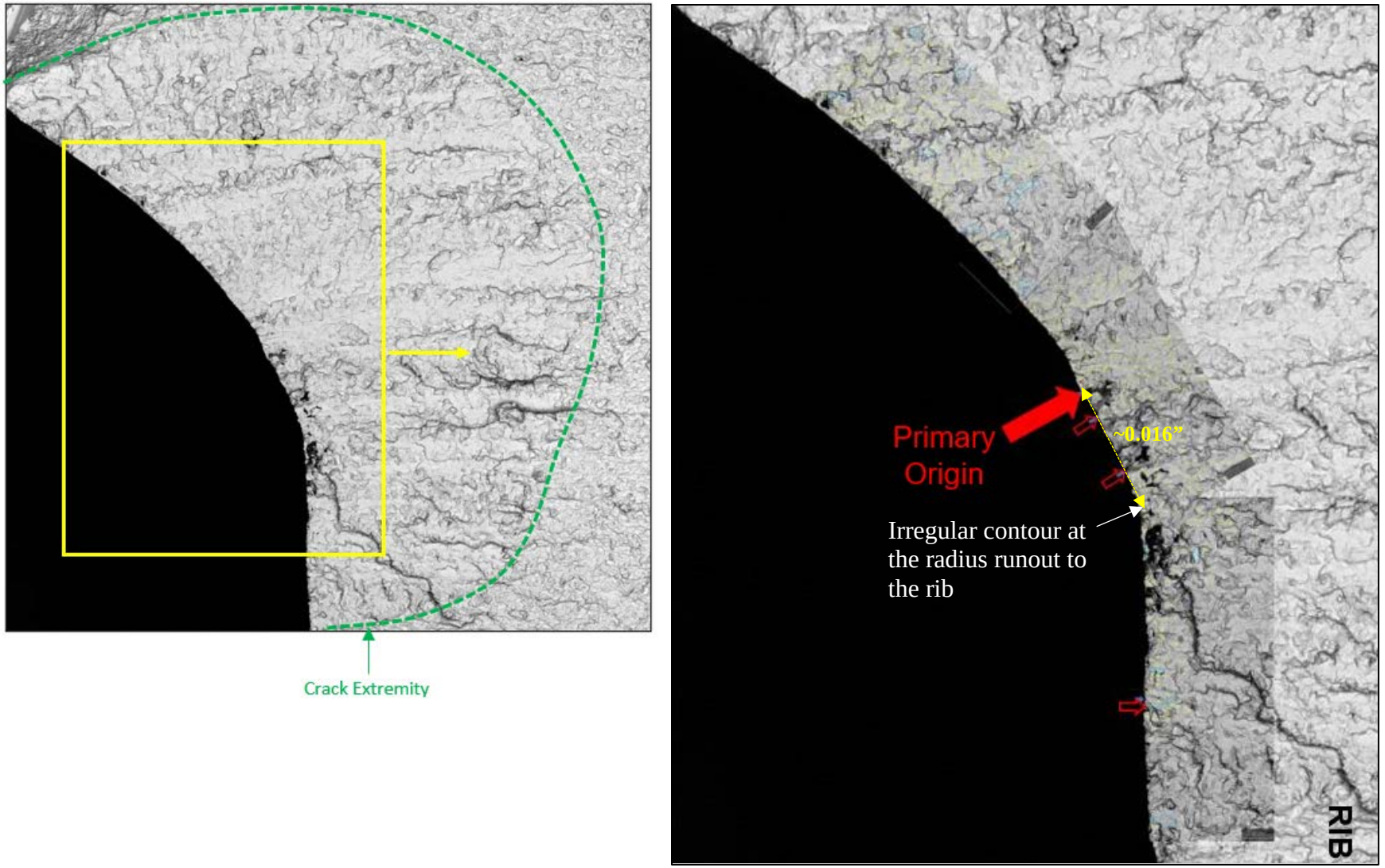

Figure 25: SEM images showing the origins identified on the secondary chordwise crack that was lab fractured open, indicated by the red arrows. Featureless facets and surface origins were both observed.

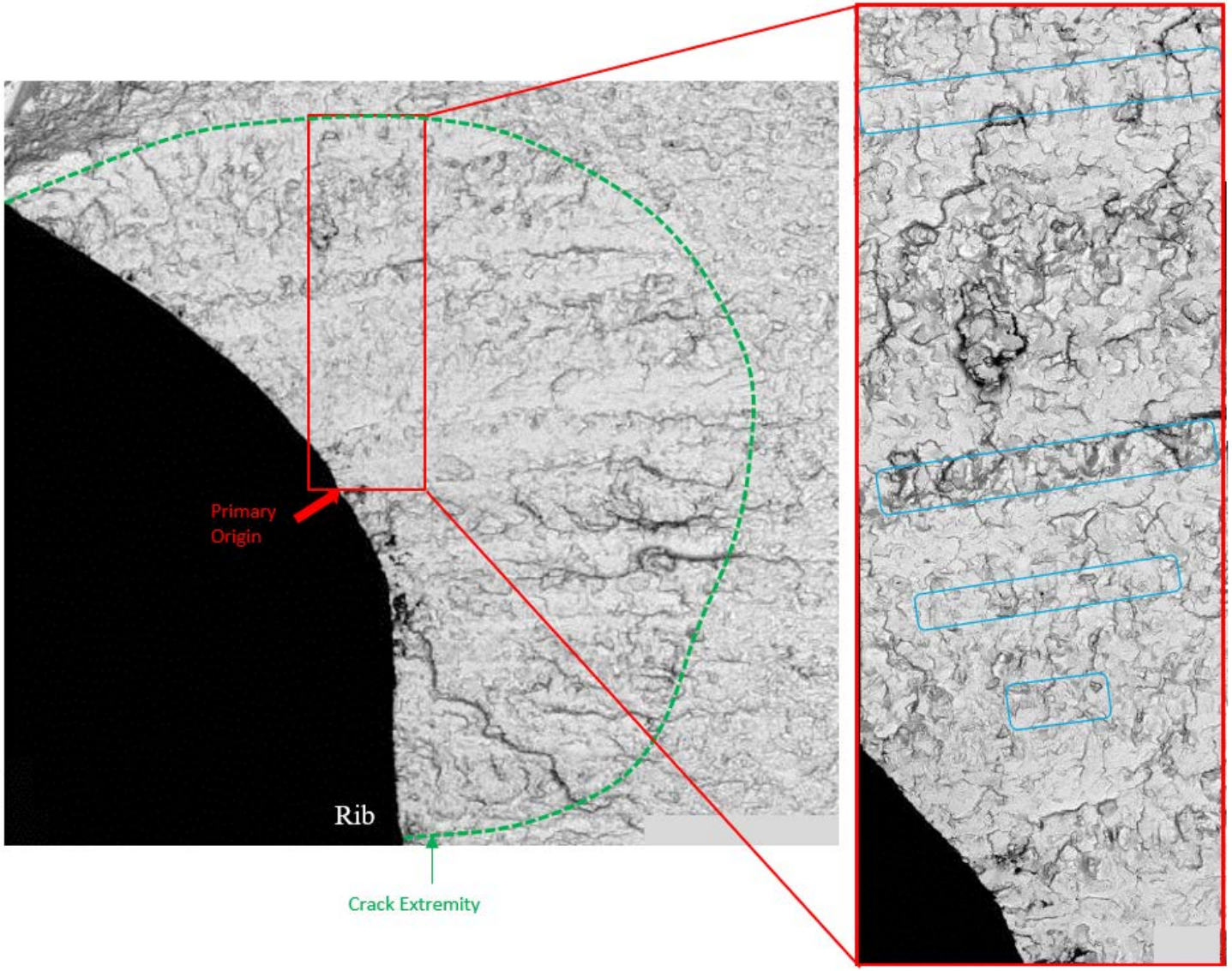

Figure 26: SEM images showing the bands of striations observed in the crack progression (blue boxes). Striation spacing was measured at multiple locations in each of these 4 blue boxes; the rate ranged from $2.9x10^{-6}$ to $6.9x10^{-6}$ in/cycle.

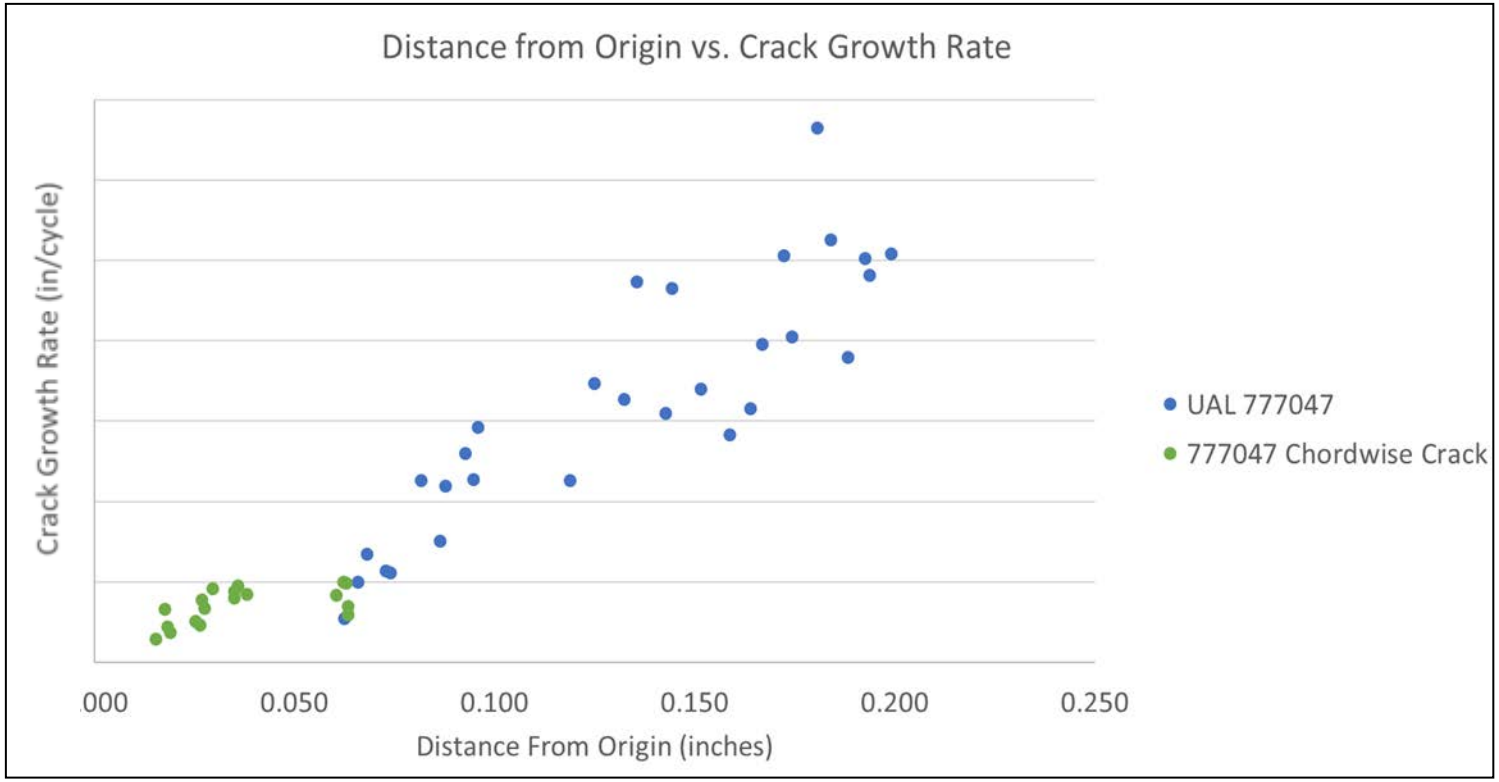

Figure 27: Graph showing crack growth rate vs. distance from the origin of both the primary fracture and the secondary chordwise crack.

Clean and segmented EBSD data

Individual MTR's

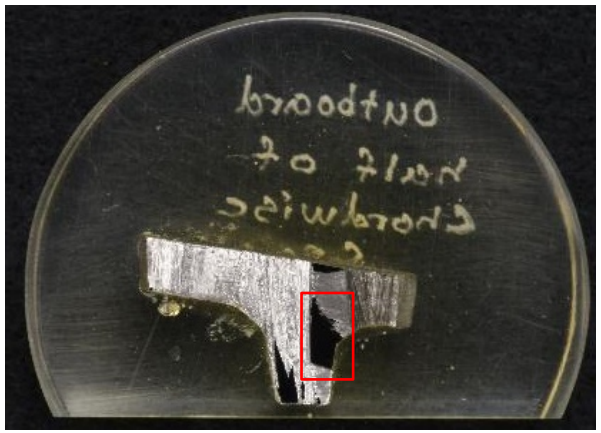

# of MTR's identified	Max MTR Size (μm^2)	Avg MTR Size (μm^2)
35	234723	34552

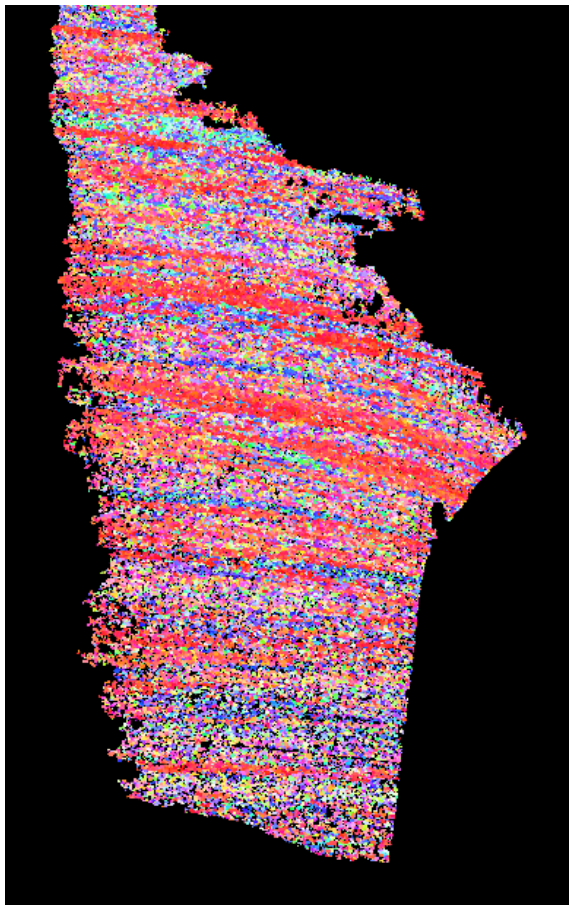

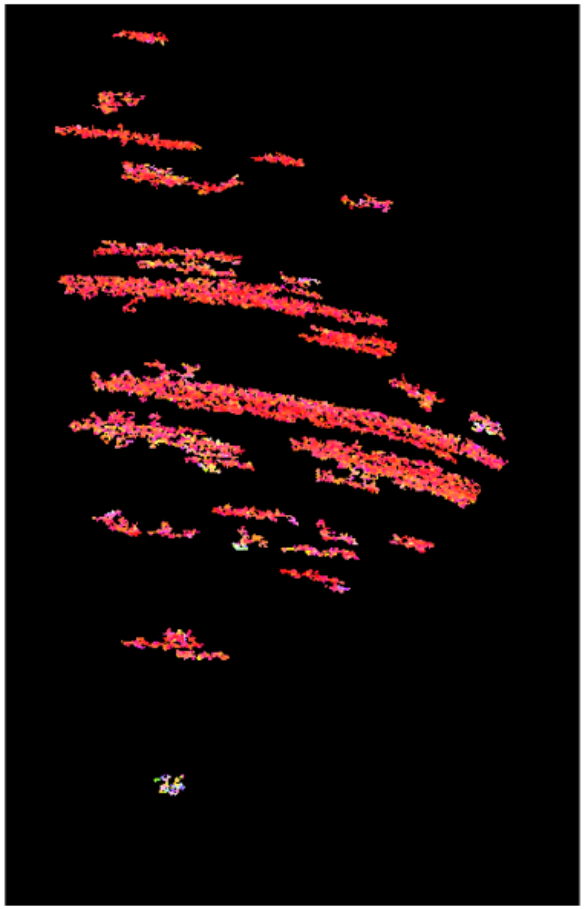

Figure 28: Images showing the EBSD/OIM results on the section planar into the secondary chordwise crack. Red areas represent basal texture regions (MTRs).

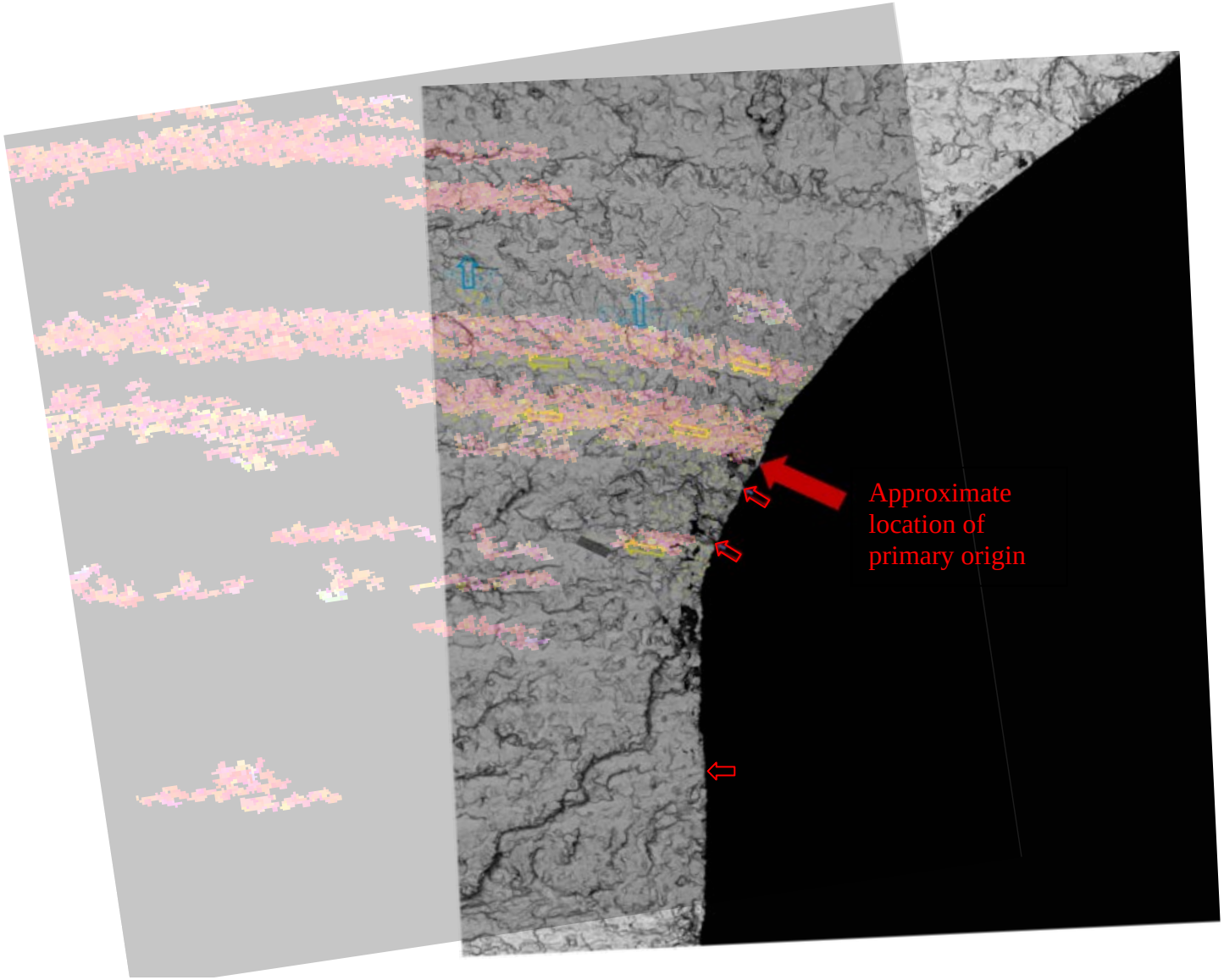

Figure 29: The individual MTR data from Figure 28 aligned with the fracture features. The primary origin on the crack (bold red arrow) was near an MTR which may have contributed to crack growth.

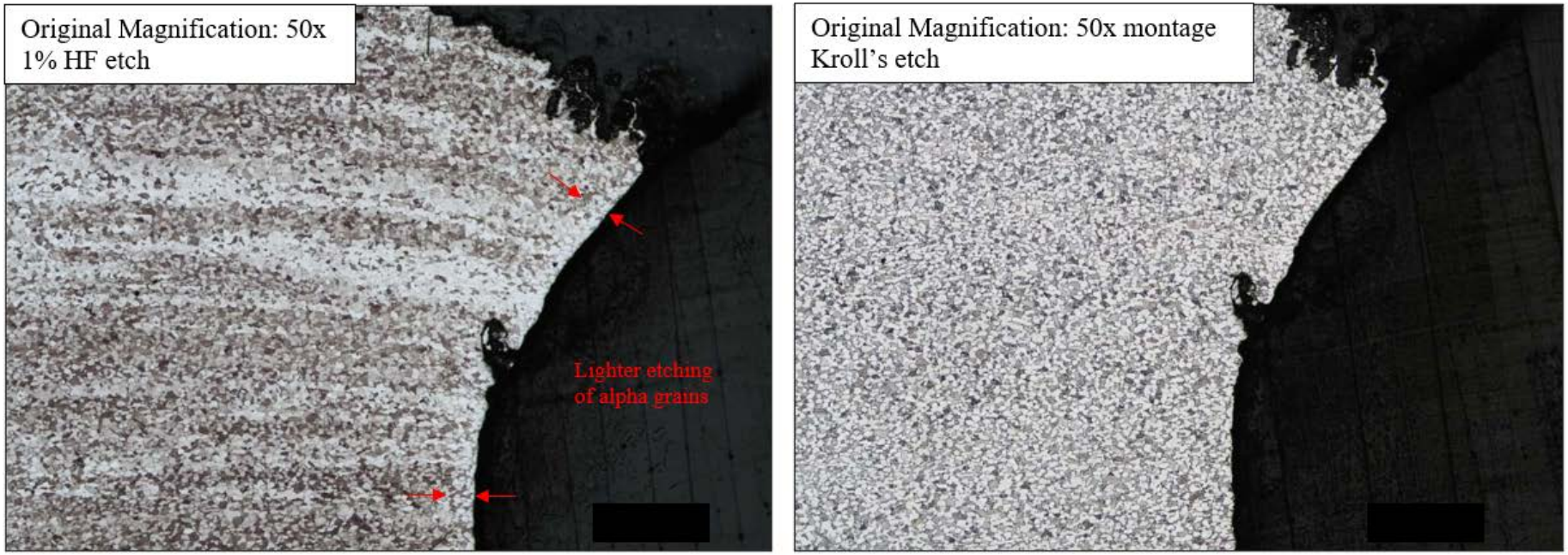

Figure 30: Metallographic images of the planar section into the chordwise crack. The section was etched with 1% HF and Kroll's after EBSD/OIM. Alpha grains near the surface exhibited a lighter etching when etched with 1% HF. No distorted surface layer/deformation was observed.

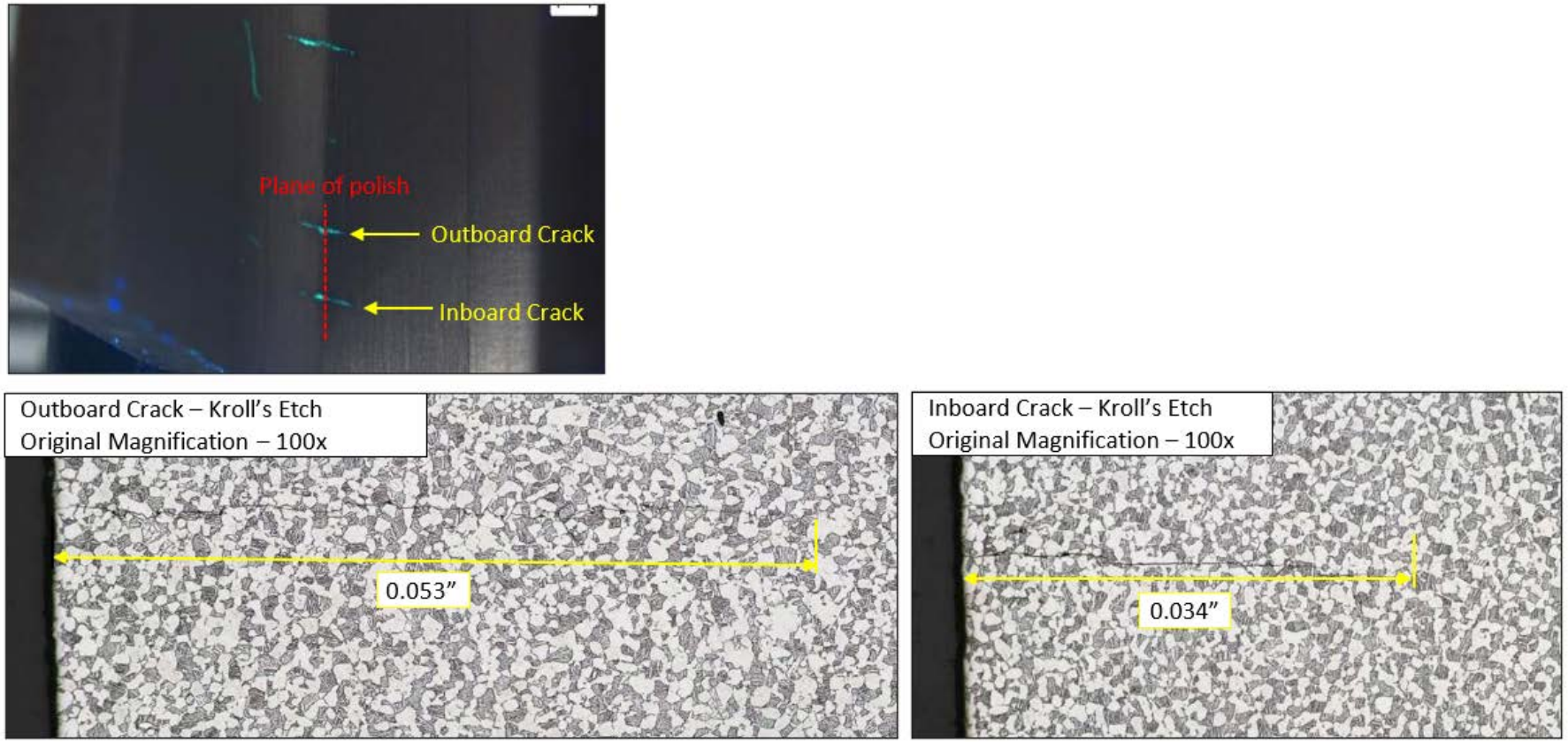

Figure 31: Metallographic images showing the section through the two secondary cracks furthest inboard from the fracture surface etched with Kroll's. The maximum crack depths observed in the polishes were 0.053” and 0.034” for the outboard and inboard cracks, respectively.

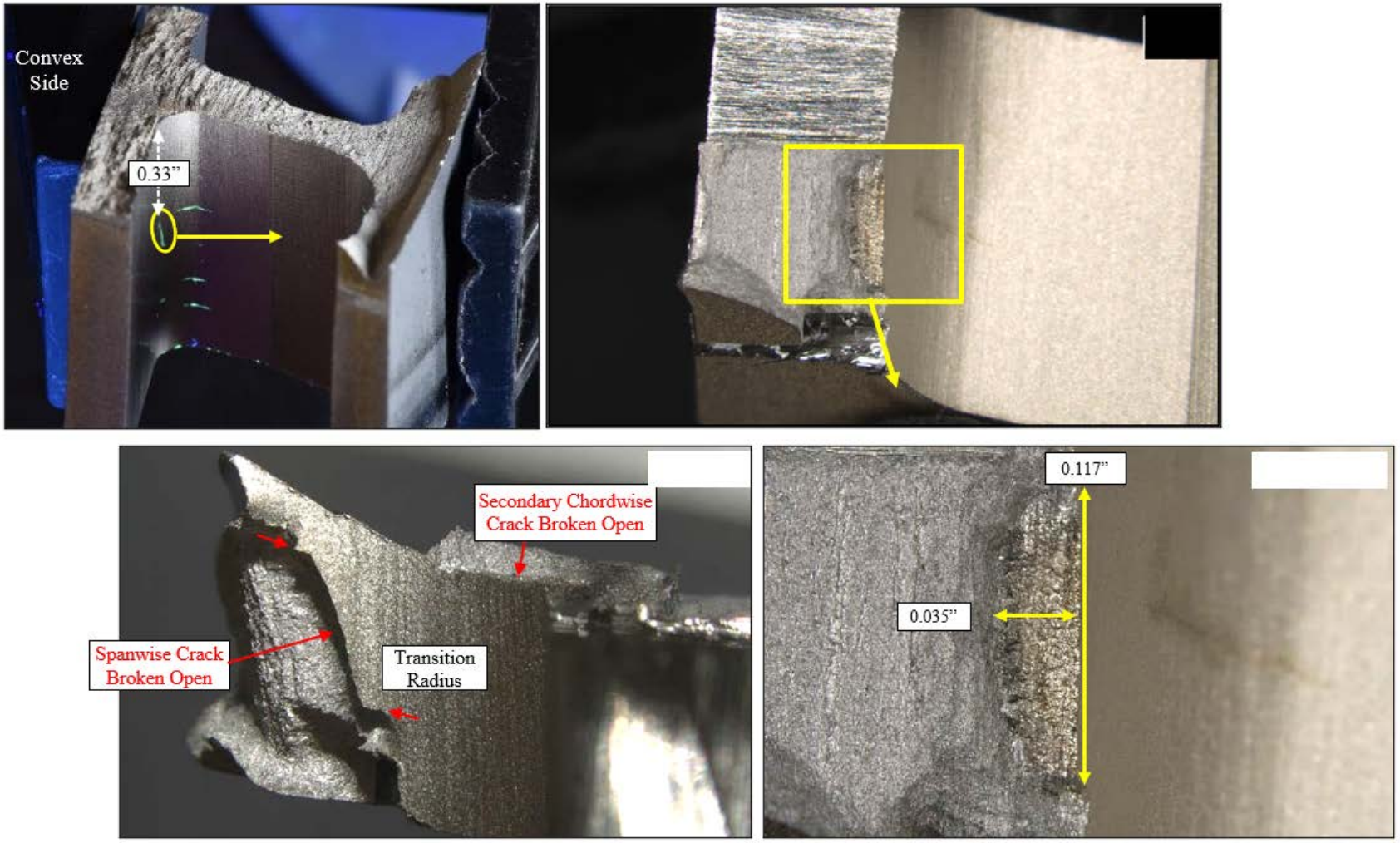

Figure 32: Images of the spanwise secondary crack in the convex wall side of the transition radius. The broken open crack measured approximately 0.117” in length and 0.035” in depth.

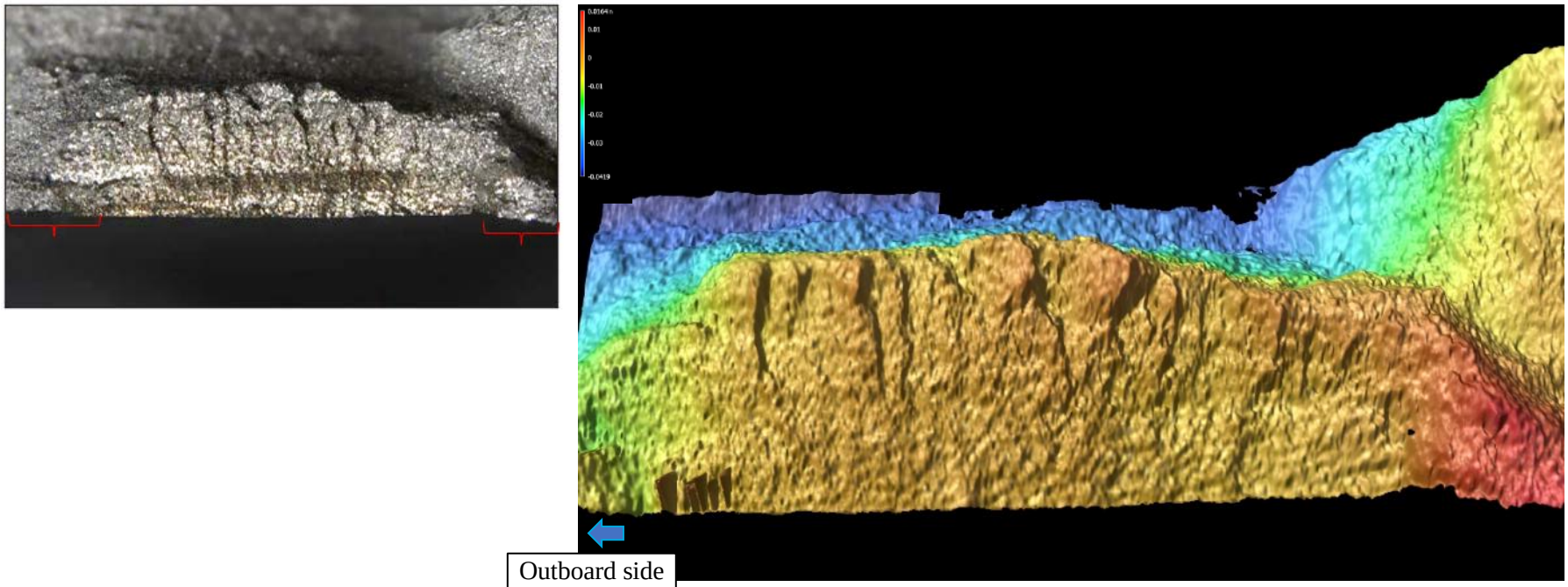

Figure 33: Keyence 3D scan showing the plane changes at the extremities of the crack (red brackets). The green/blue areas in the 3D scan are going into the page and the red areas are coming out of the page.

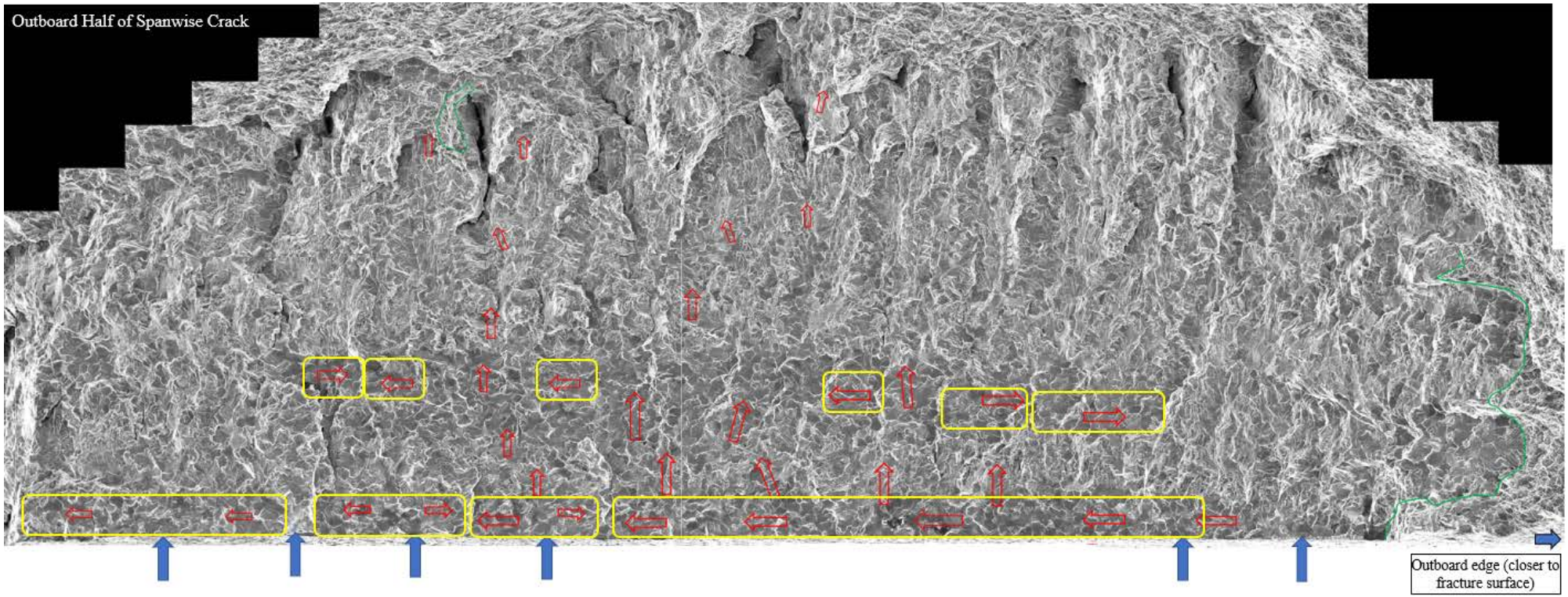

Figure 34: SEM image showing mapping of the crack progression. Multiple origins were observed along the surface (blue arrows). Crack growth at the origins was made up of predominantly faceted features that progressed along the surface, indicating a possible MTR contribution. Predominantly cleavage features were observed progressing from potential MTR regions at the surface. The yellow boxes indicate possible MTRs based on the fractographic assessment. The red arrows indicate general crack propagation direction.

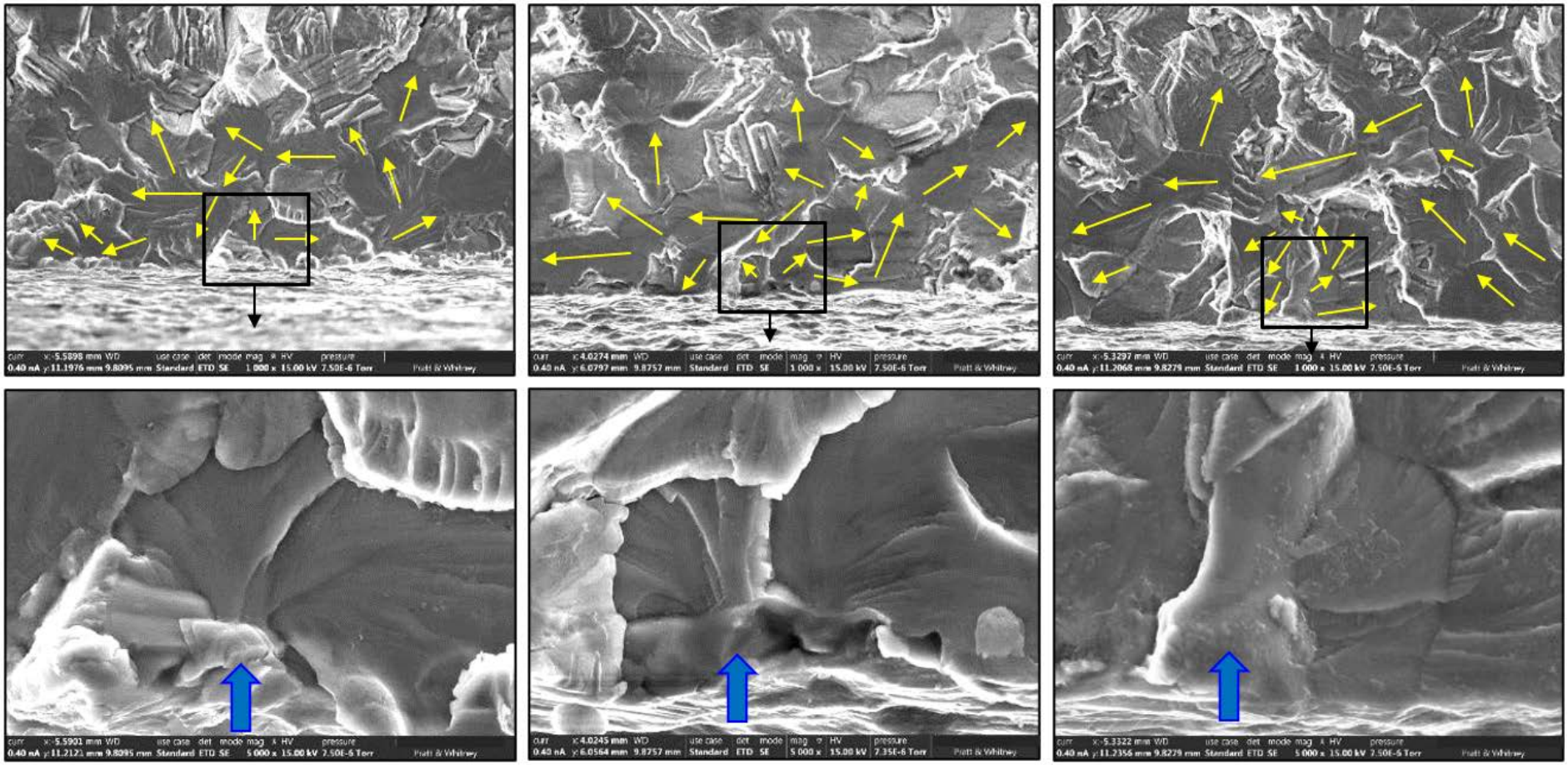

Figure 35: SEM examination showing representative images of the origins observed on the spanwise crack (blue arrows).

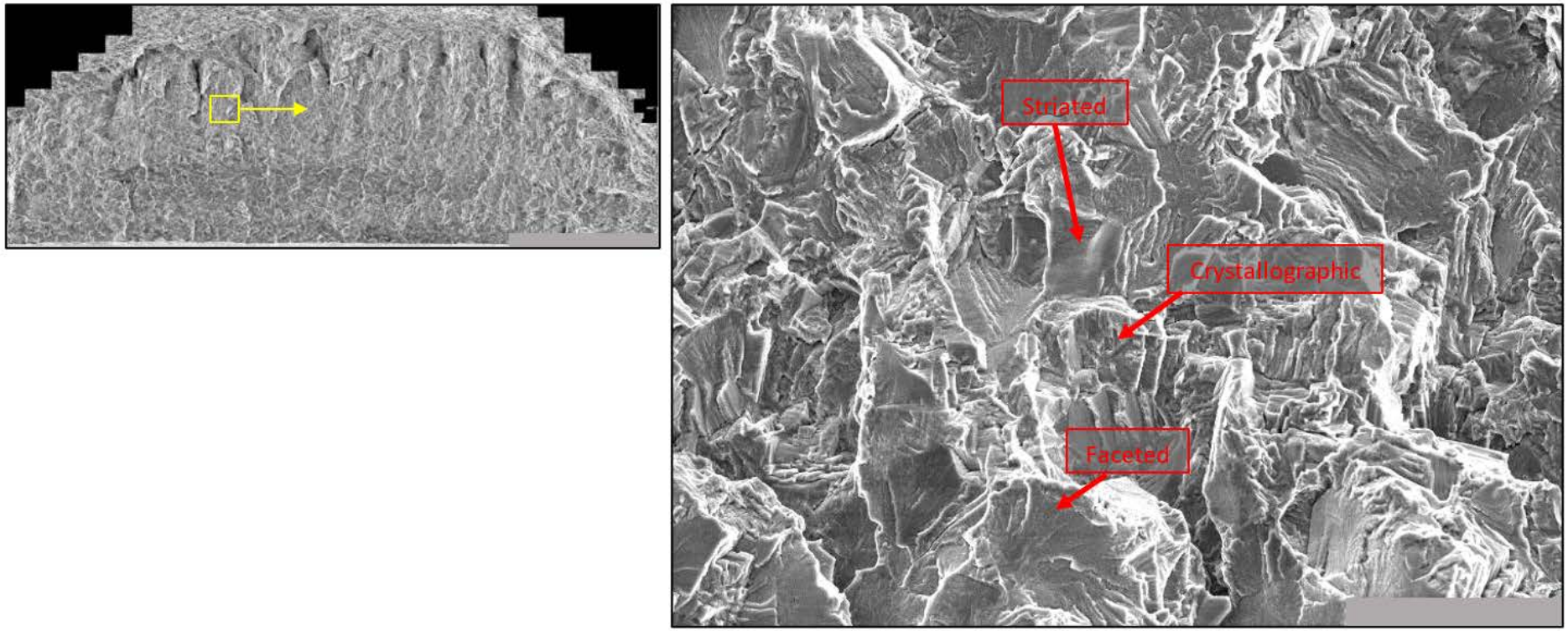

Figure 36: SEM image showing features representative of the crack progression. The crack exhibited a mix of faceted, striated, and crystallographic growth.

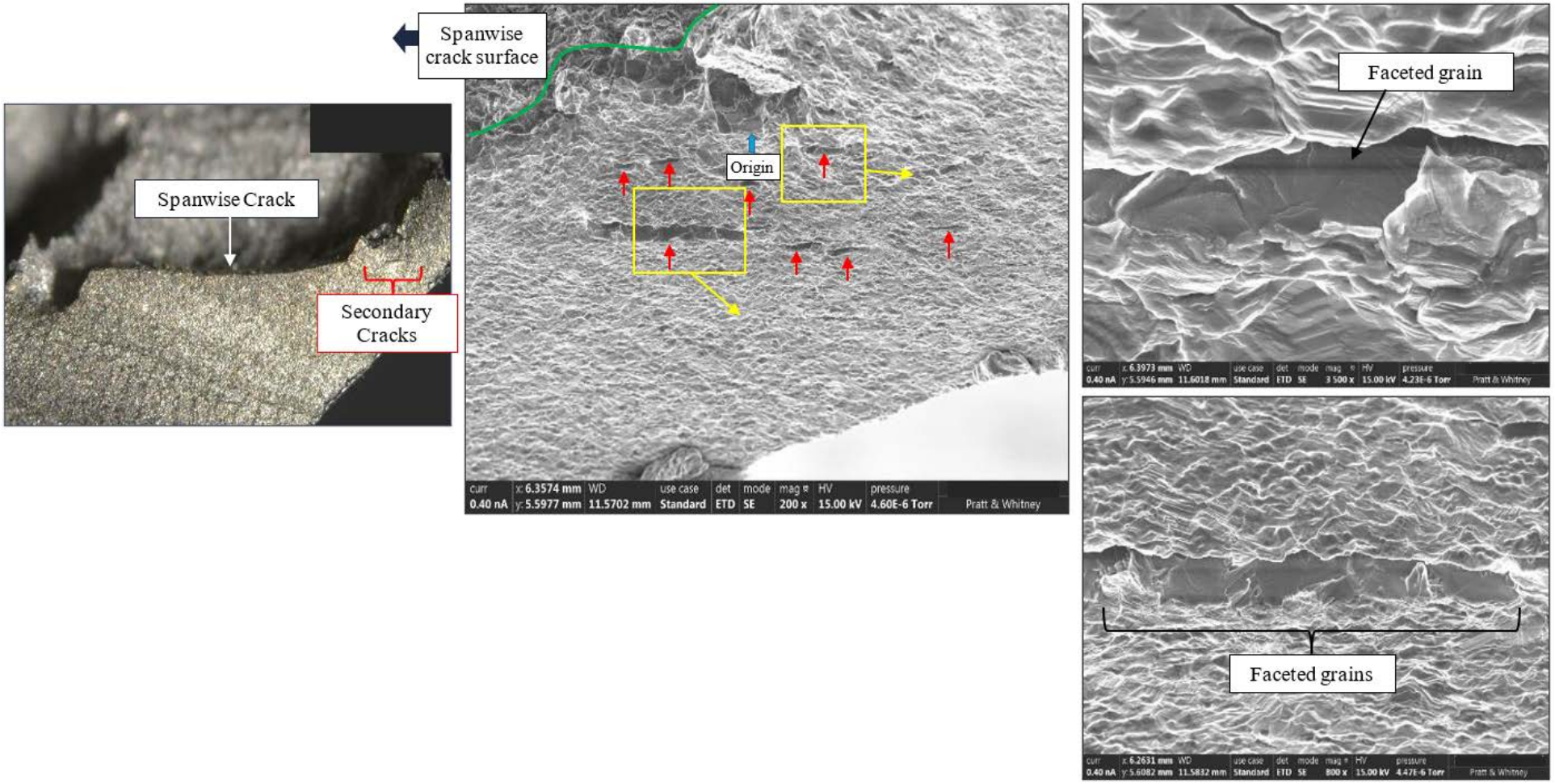

Figure 37: Additional binocular and SEM examination identified secondary cracking adjacent to the spanwise crack extremity (red arrows). Faceted grains were observed along the surface of the secondary cracks.

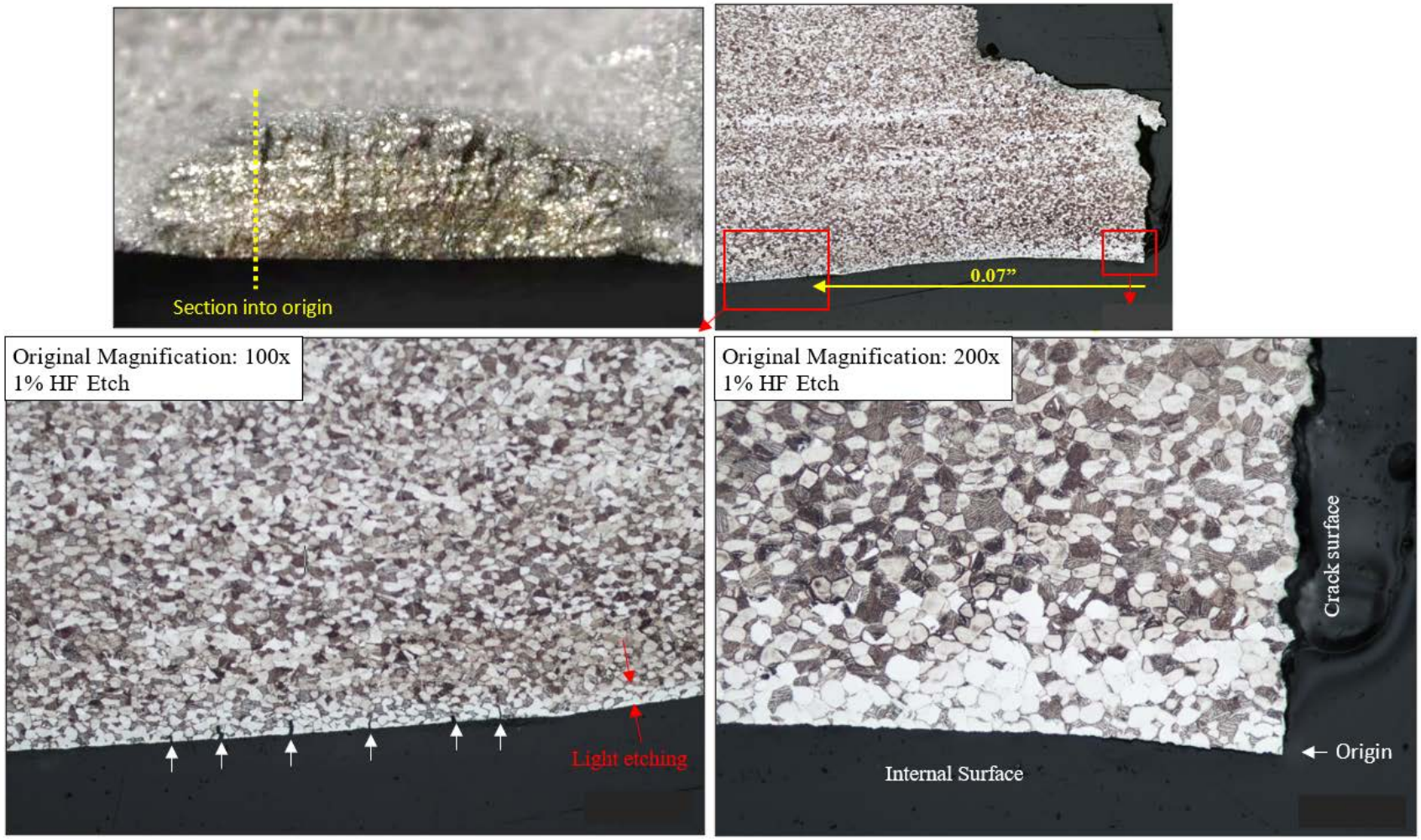

Figure 38: Four step polishes were prepared through the primary origin on the spanwise crack. 1% HF and Kroll’s etches were completed at each increment. The images shown above are from the 1% HF etch on the second polish. Alpha grains near the surface exhibited a lighter etching when etched with 1% HF. No distorted surface layer/deformation was observed. Secondary cracks up to 0.001” in depth were observed approximately 0.07” from the spanwise crack (away from the radius).

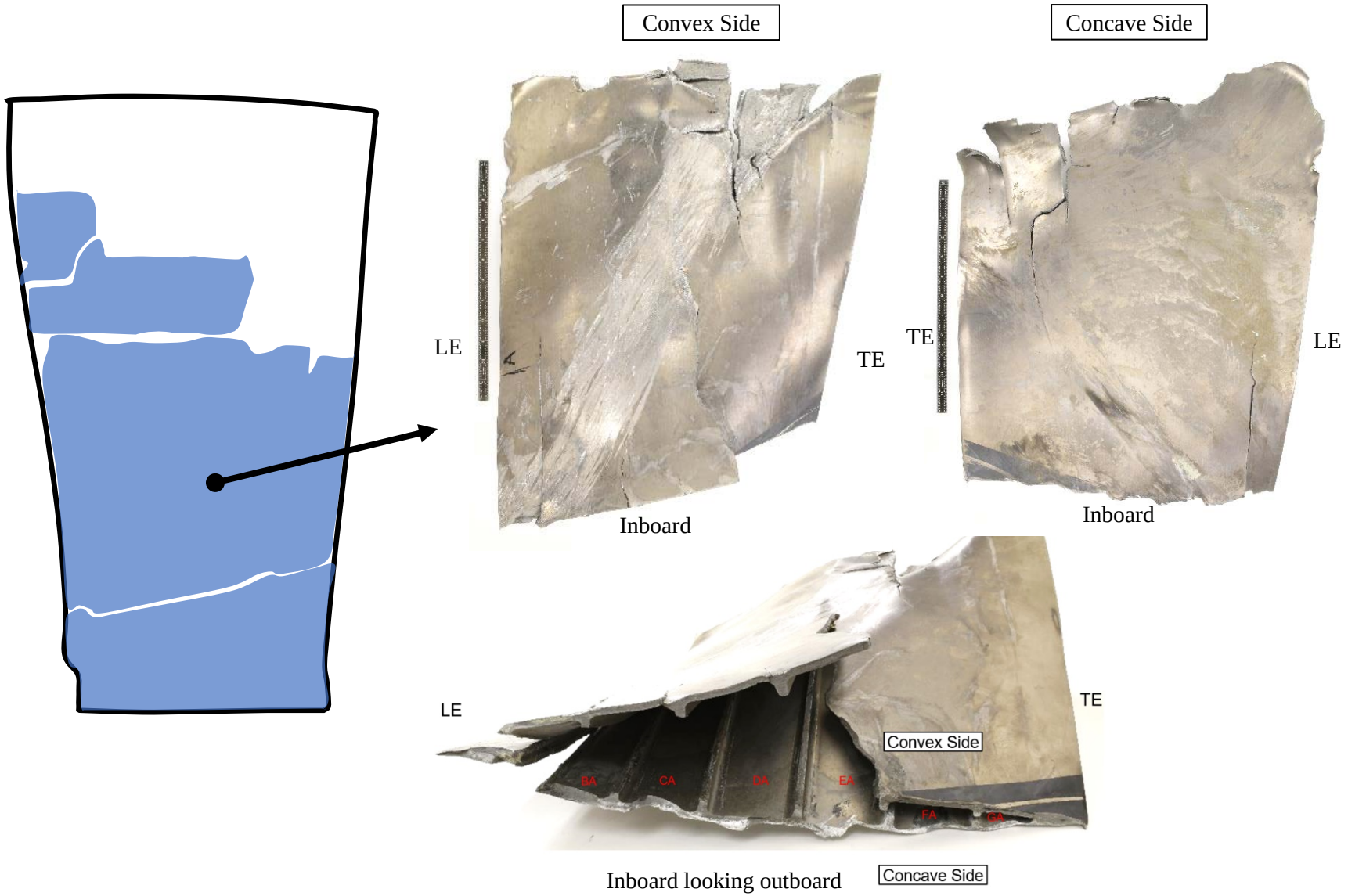

Figure 39: Images of the midspan blade fragment recovered from the fan containment case.

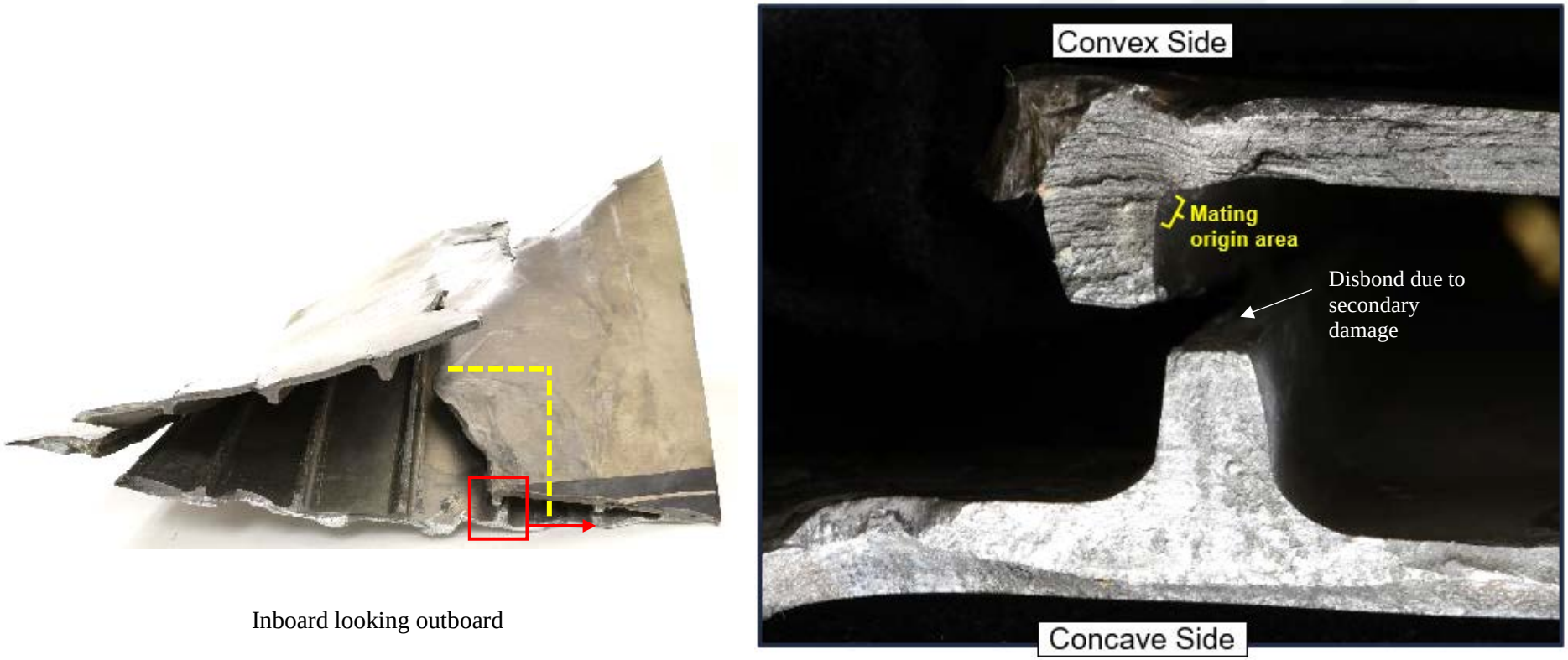

Inboard looking outboard

Figure 40: Images showing the outboard half of the flowpath fracture surface. The origin area was mostly intact with some post-fracture damage. The concave and convex sides of the blade were disbonded due to secondary damage. Sectioning was completed along the yellow dotted lines to remove the origin area for further evaluation.

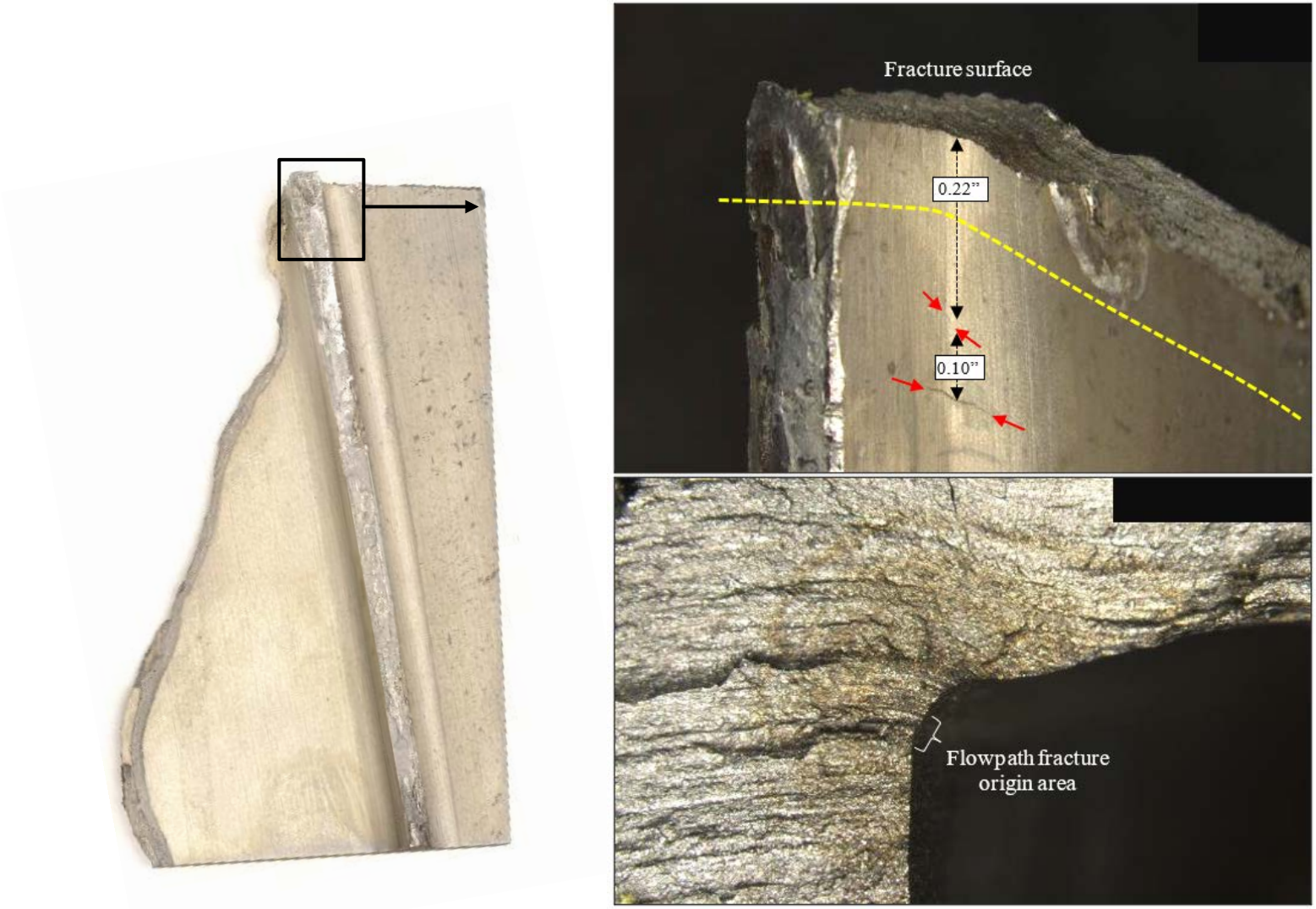

Figure 41: Images of the outboard half of the fracture surface. Two additional secondary cracks were identified within 0.32” of the fracture surface (red arrows). The origin area was intact (bottom right image). The fracture surface was sectioned from the secondary cracks for further evaluation (yellow dotted line).

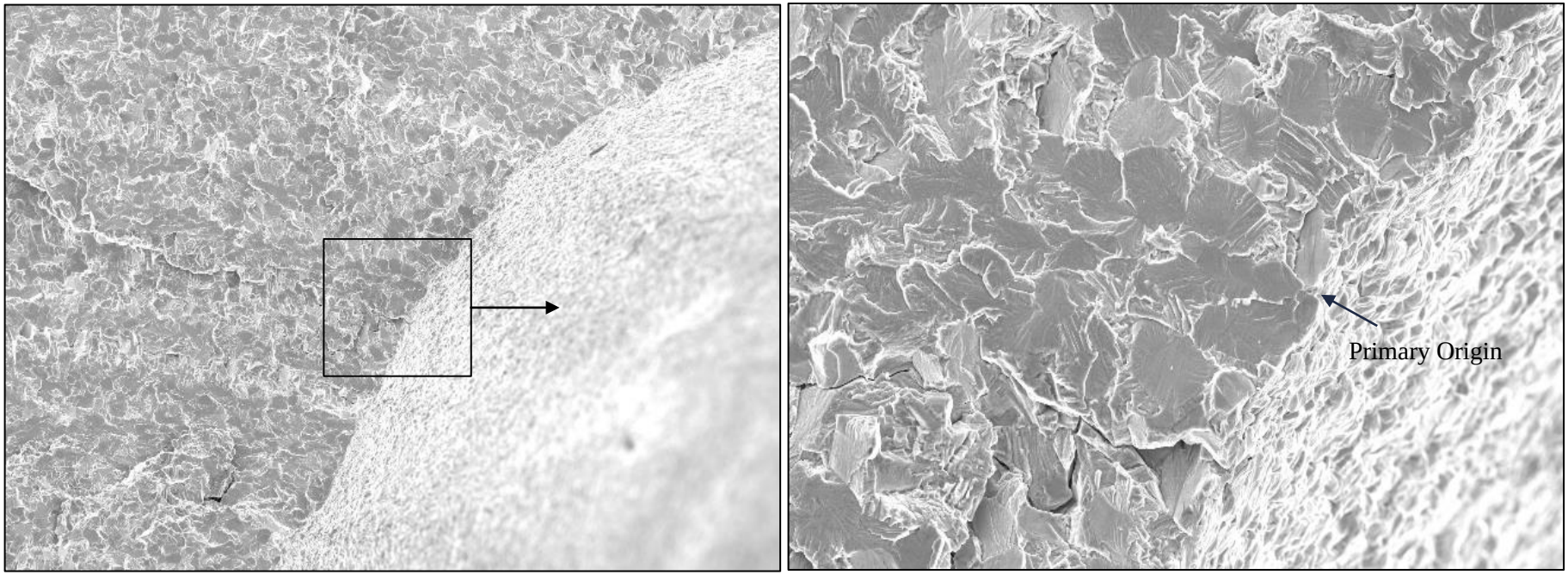

Figure 42: SEM examination of the outboard side of the fracture found features consistent with the inboard side of the fracture. No anomalies were observed at the surface at or near the origin area.

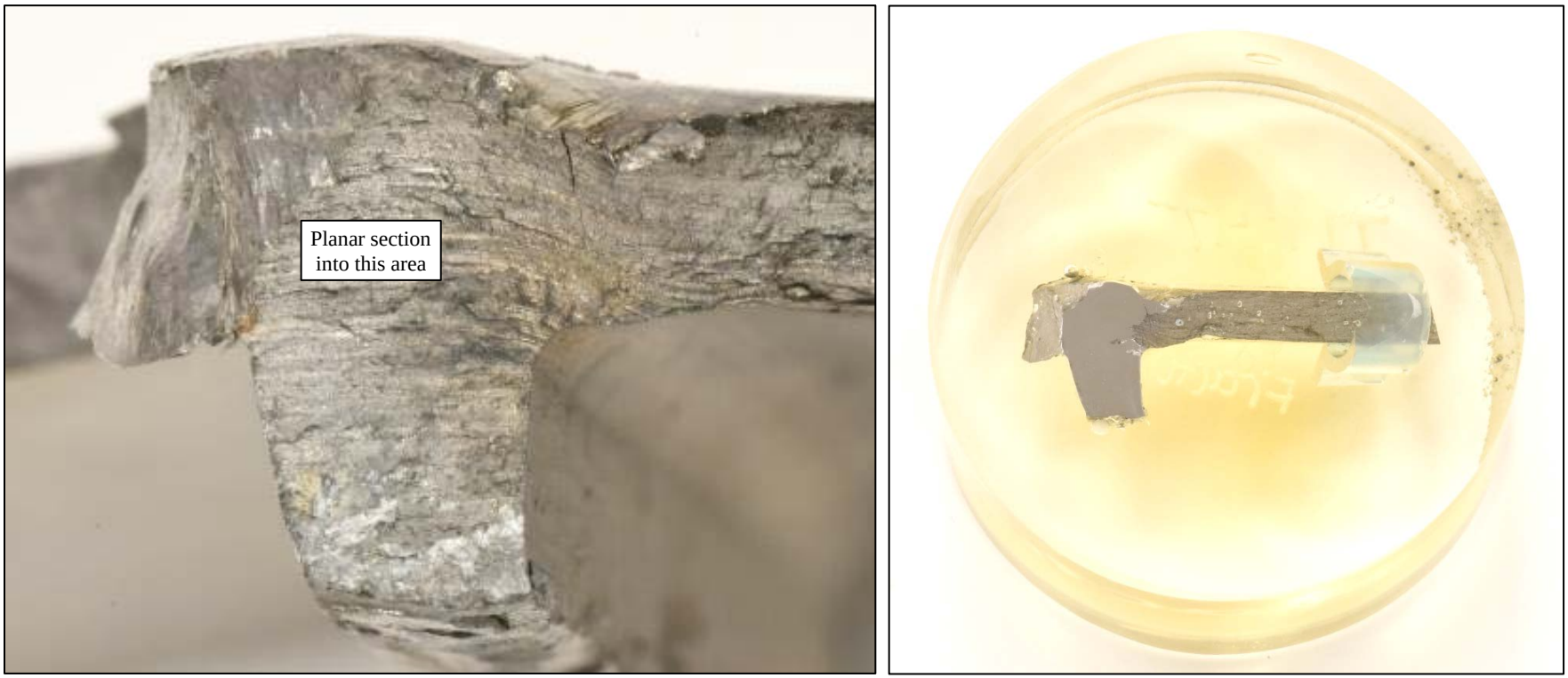

Figure 43: Image of the metallographic section prepared planar into the outboard half of the fracture surface. This section was used for EBSD/OIM to evaluate for MTRs near the origin area.

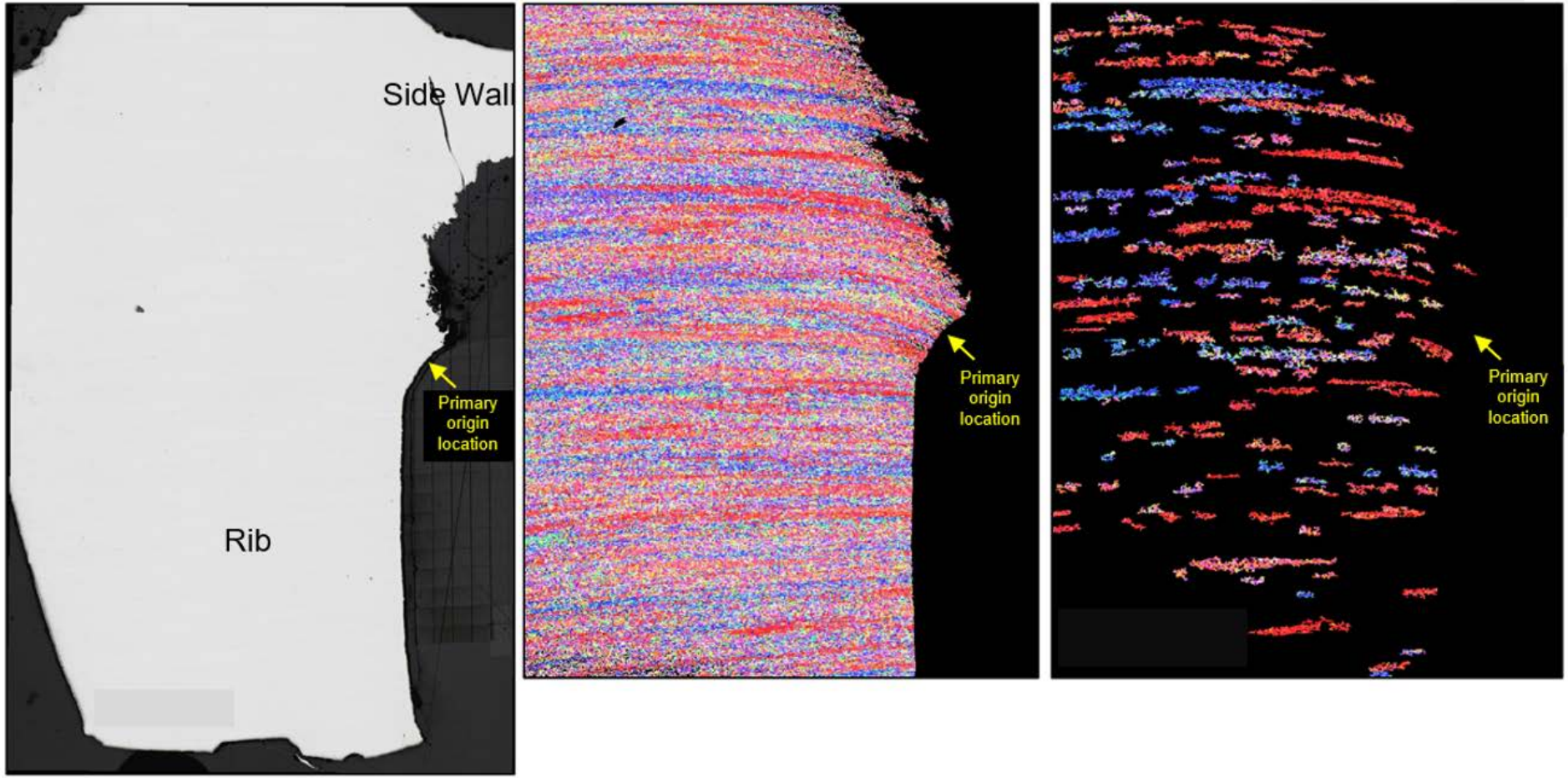

Figure 44: Images showing the EBSD/OIM results on the section planar into the fracture origin. Red areas represent basal texture regions. No MTRs were identified at the primary origin that was associated with the through-wall progression.

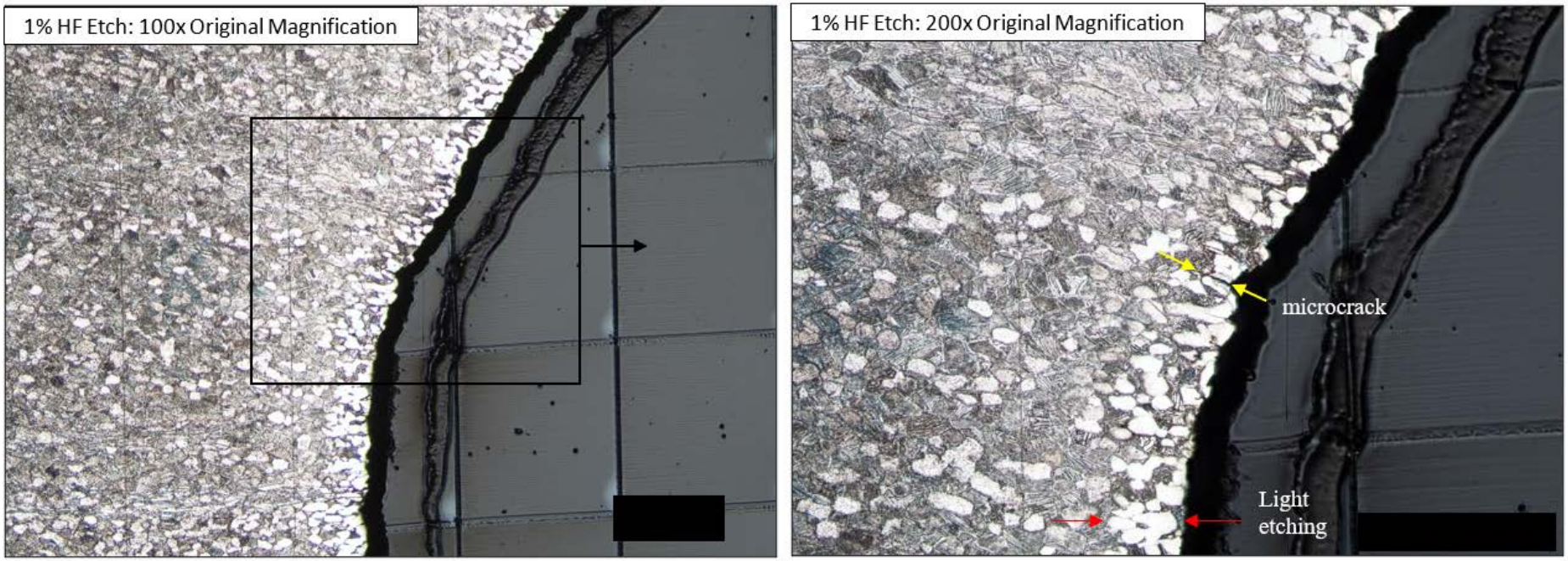

Figure 45: The planar section into the outboard half of the fracture origin area was etched with 1% HF. The alpha grains near the cavity surface exhibited a lighter etching layer. No distorted surface layer/deformation was observed. A spanwise microcrack, approximately 0.001" in depth, was observed at the radius runout to the rib.

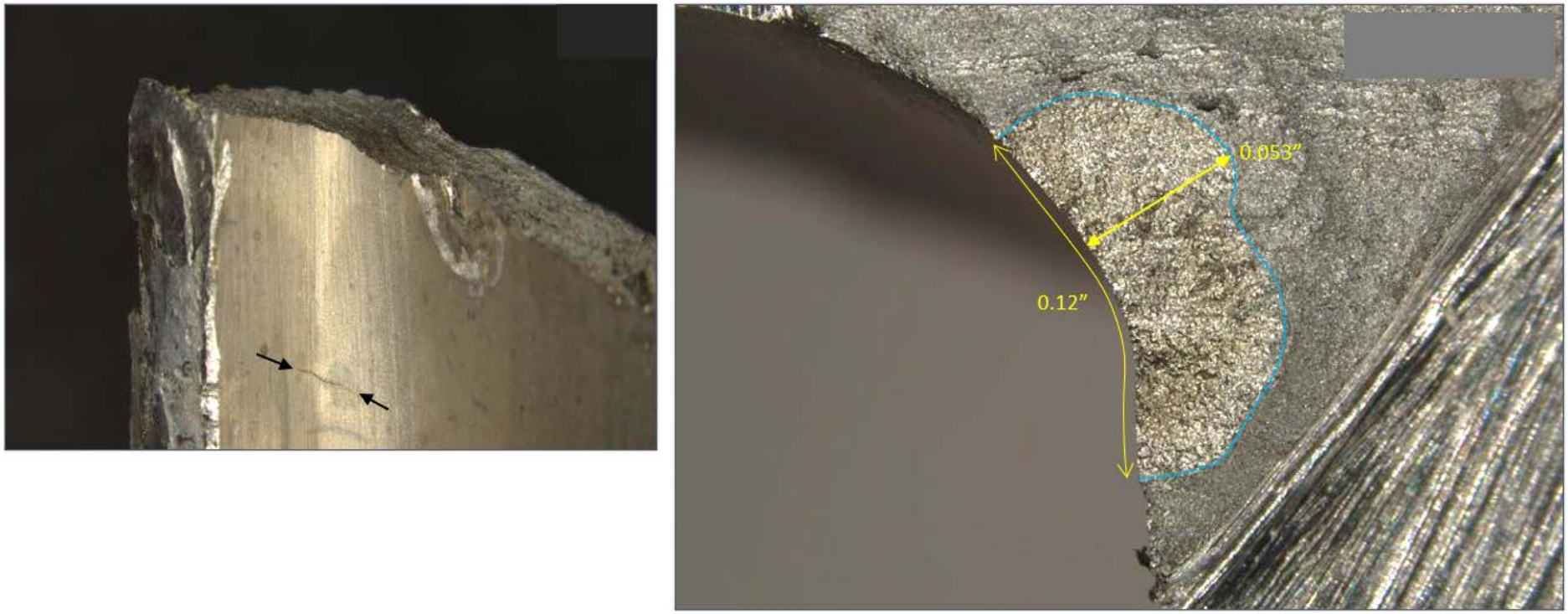

Figure 46: The large crack outboard of the fracture surface was broken open. The maximum crack depth measured 0.053”.

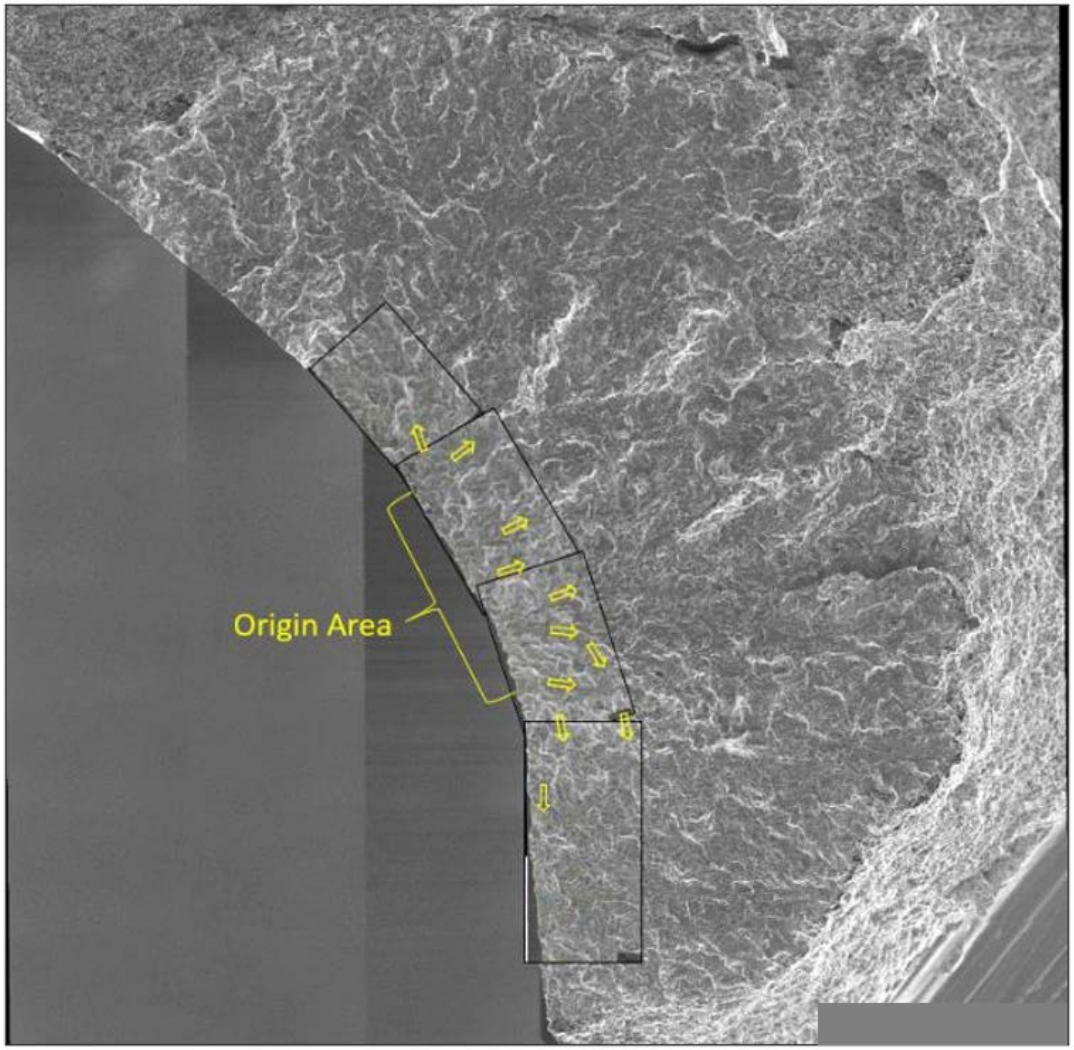

Figure 47: The outboard secondary crack origin area was located at the radius runout to the rib, consistent with the flowpath fracture surface and other secondary cracks. Some of the crack surface was smeared, likely due to damage during the event.

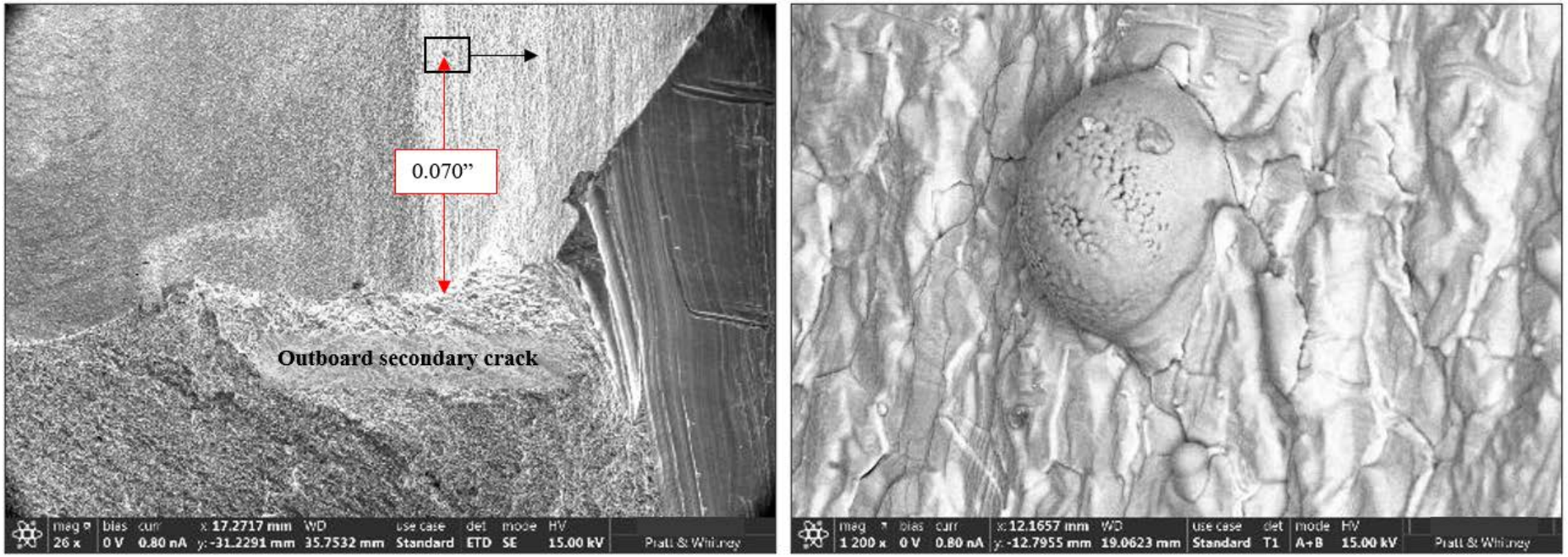

Figure 48: SEM images showing a spherical metallic deposit, consistent with what has been previously observed determined to be a “spark” from original machining, 0.070” outboard of the secondary crack. There were no sparks observed at origin area of the secondary crack and there were no cracks observed at the spark.

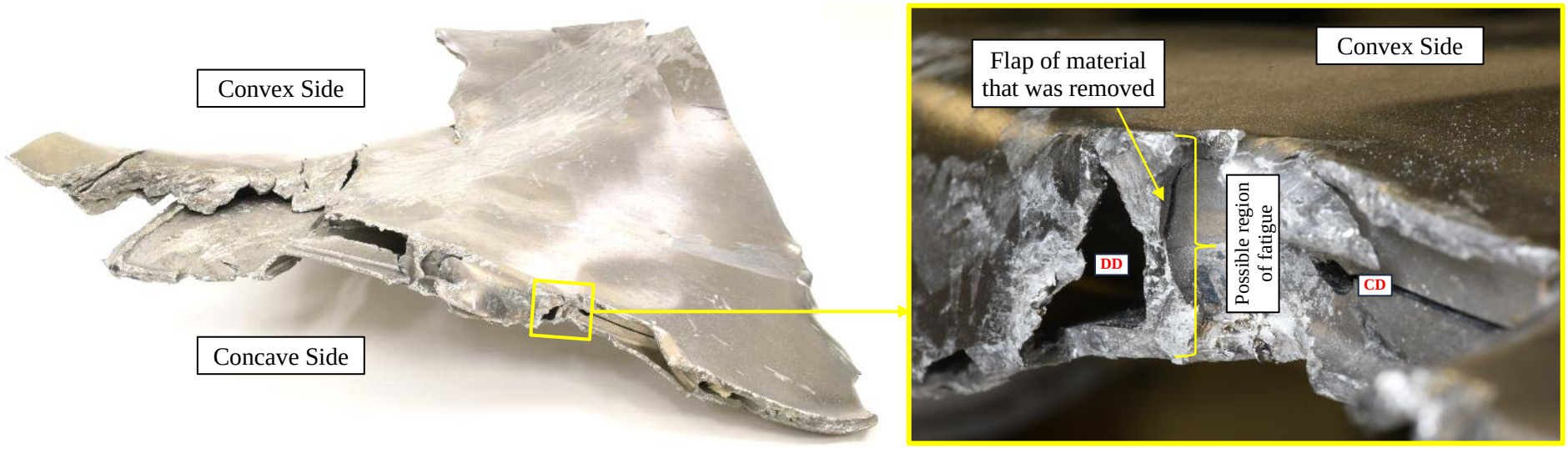

Figure 49: Binocular examination identified a region of possible fatigue on the outboard surface of the damaged piece that was removed from the case.

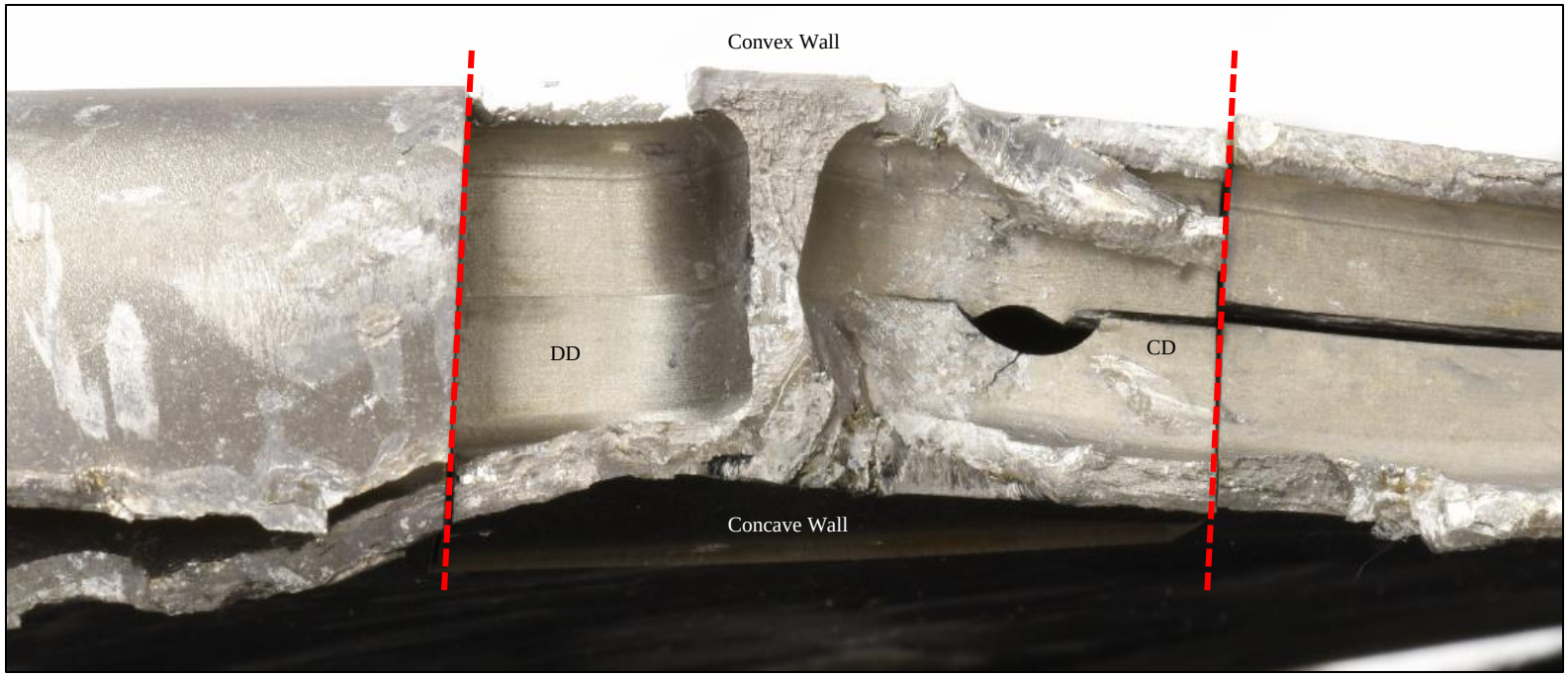

Figure 50: The area was sectioned out of the airfoil and the flap of material was removed. The area was located in the spanwise rib between cavities DD and CD, approximately 0.2” outboard of the inboard chordwise rib.

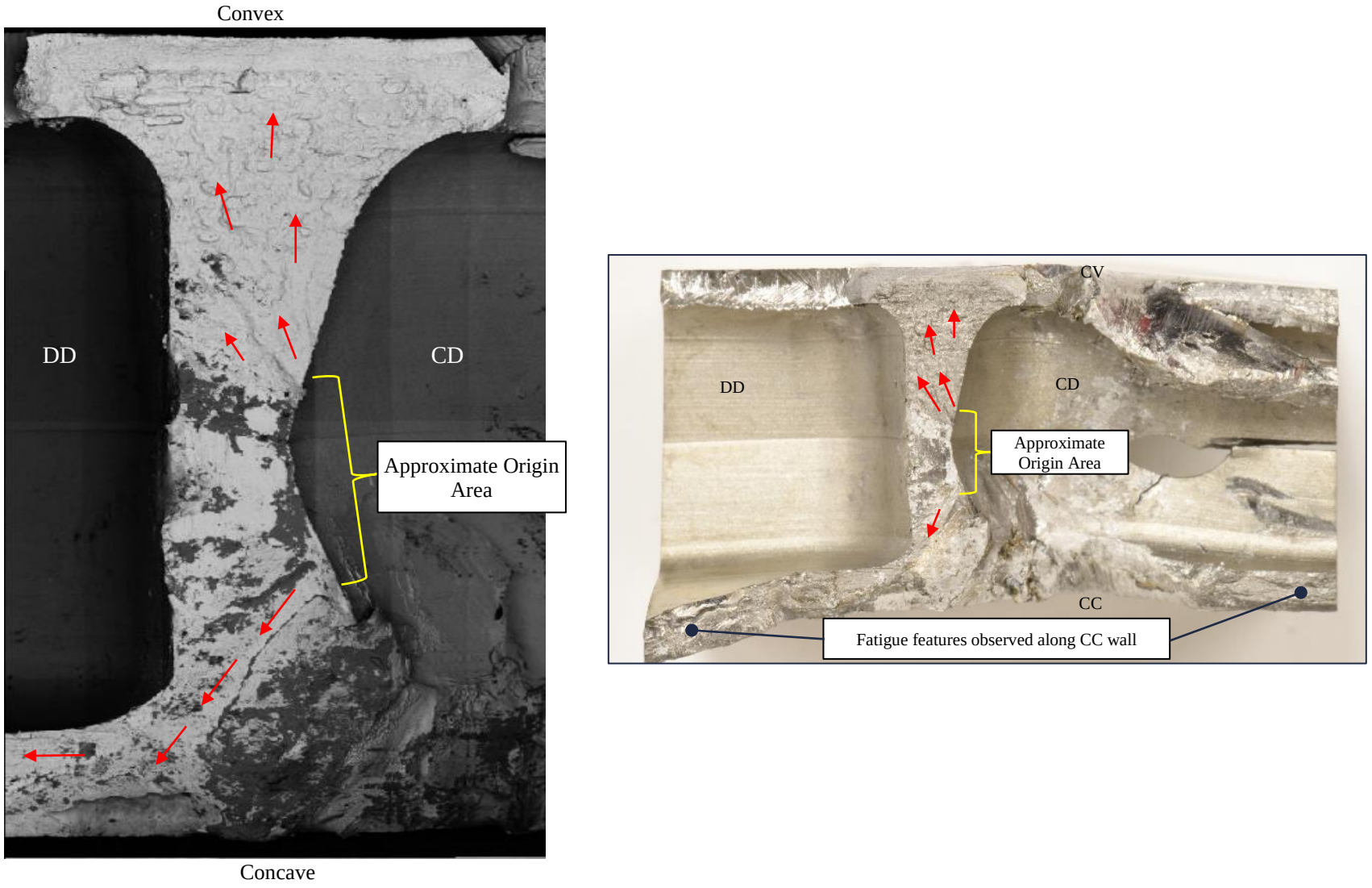

Figure 51: SEM examination identified areas of striations and faceted features interspersed among large areas of secondary damage/smearing. Fatigue features progressed from an origin located on the CD side of the rib (red arrows). Due to the damage, the exact origin area could not be identified. Fatigue features were also observed progressing along the concave wall.

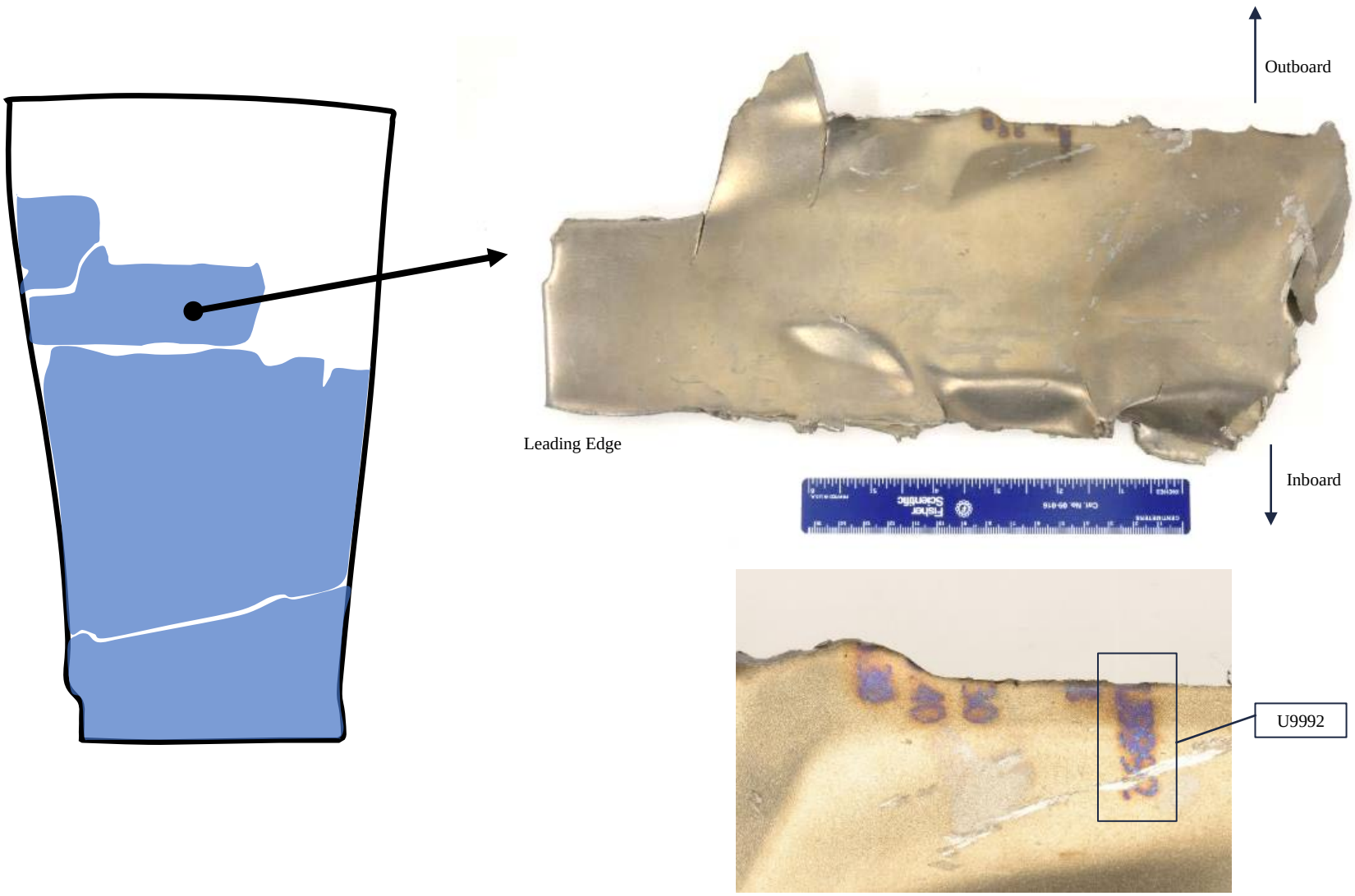

Figure 52: Images showing the largest of the outboard blade fragments. Remnant part markings included the last 5 digits of the incident blade S/N – "U9992", confirming that the fragment was from the incident blade.

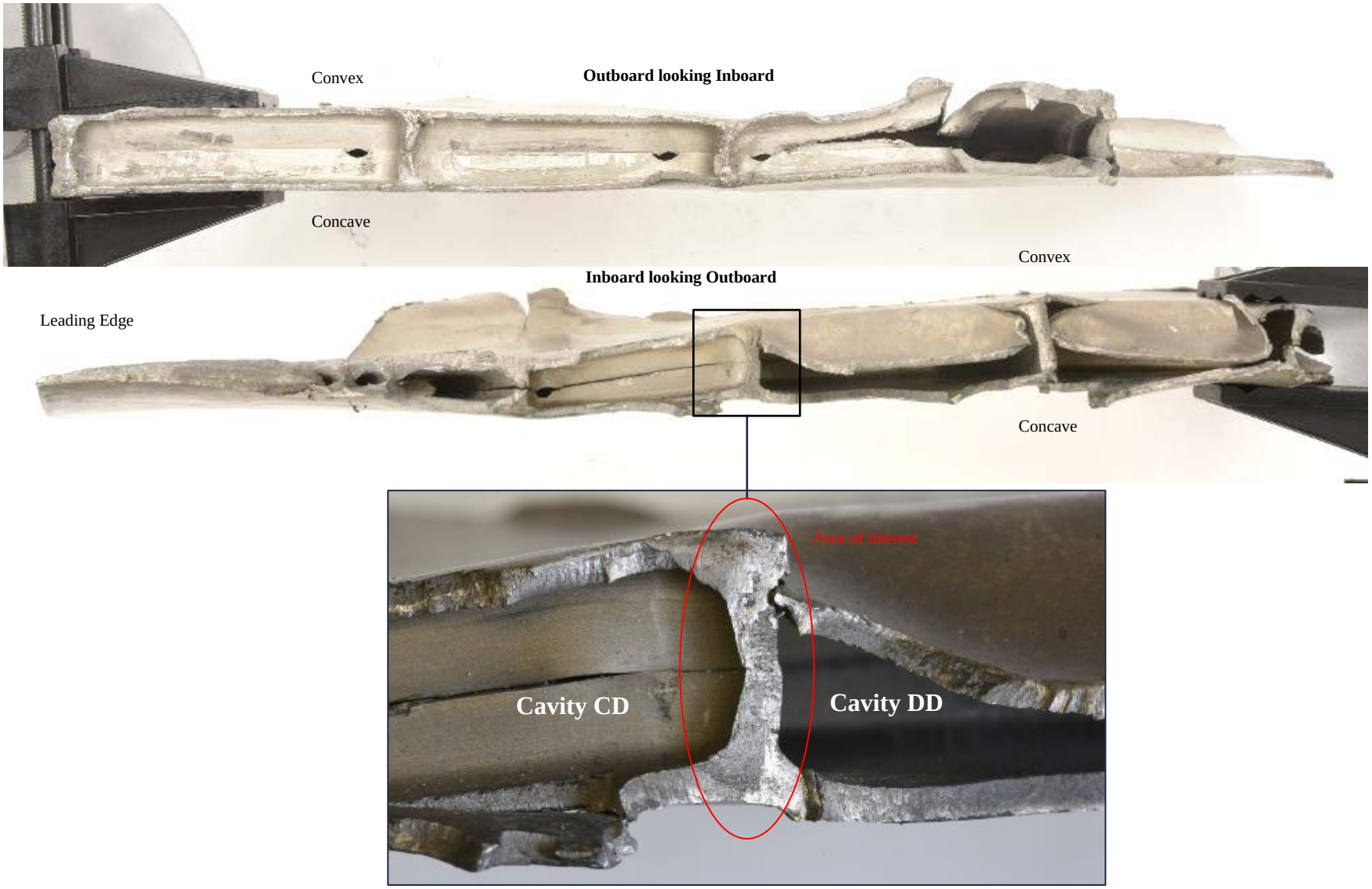

Figure 53: Binocular microscope inspection of the fracture surfaces identified possible fatigue on the inboard side of the fragment between cavities CD and DD.

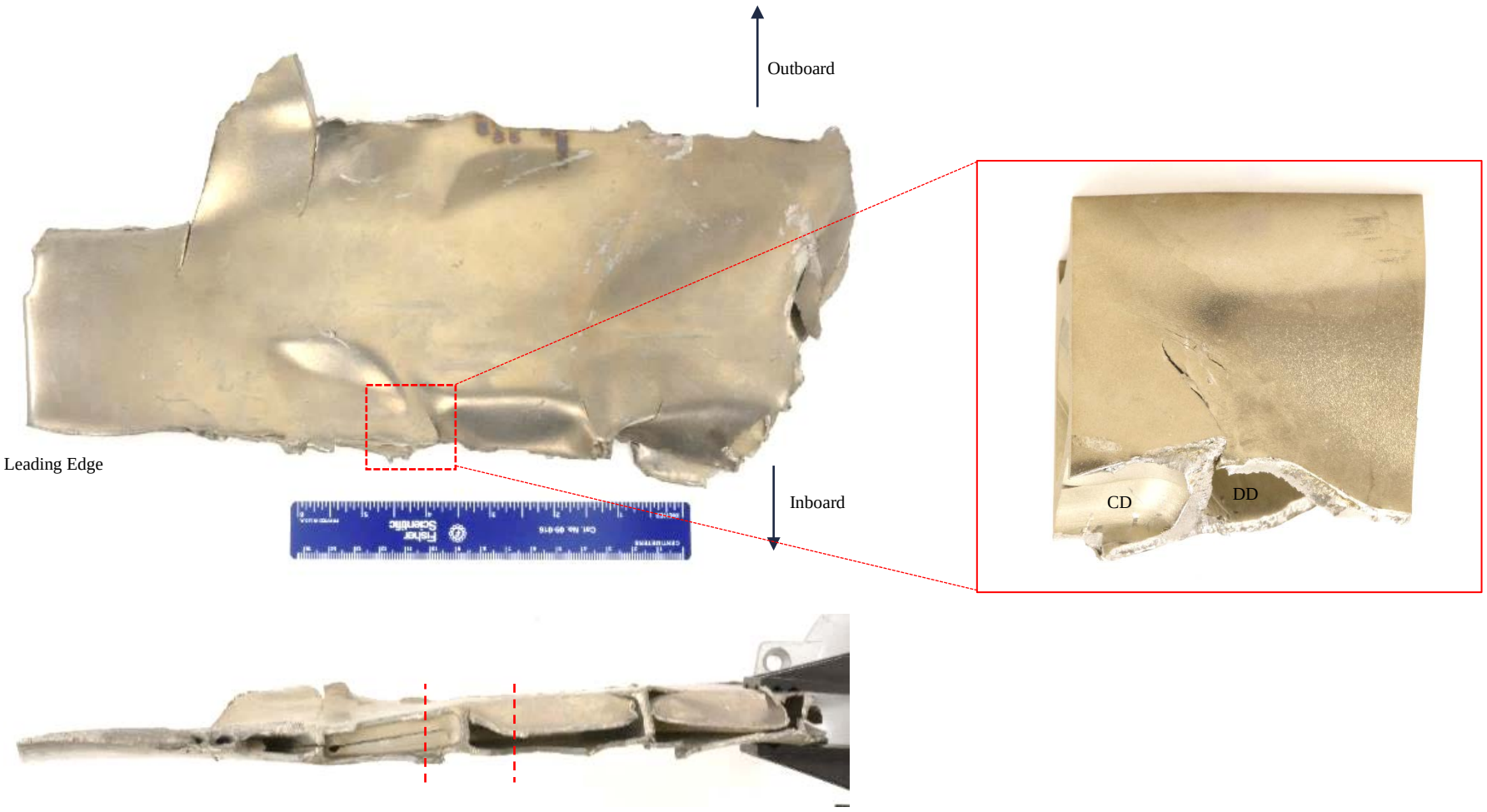

Figure 54: The region identified as possible fatigue was sectioned from the outboard midspan fragment as shown.

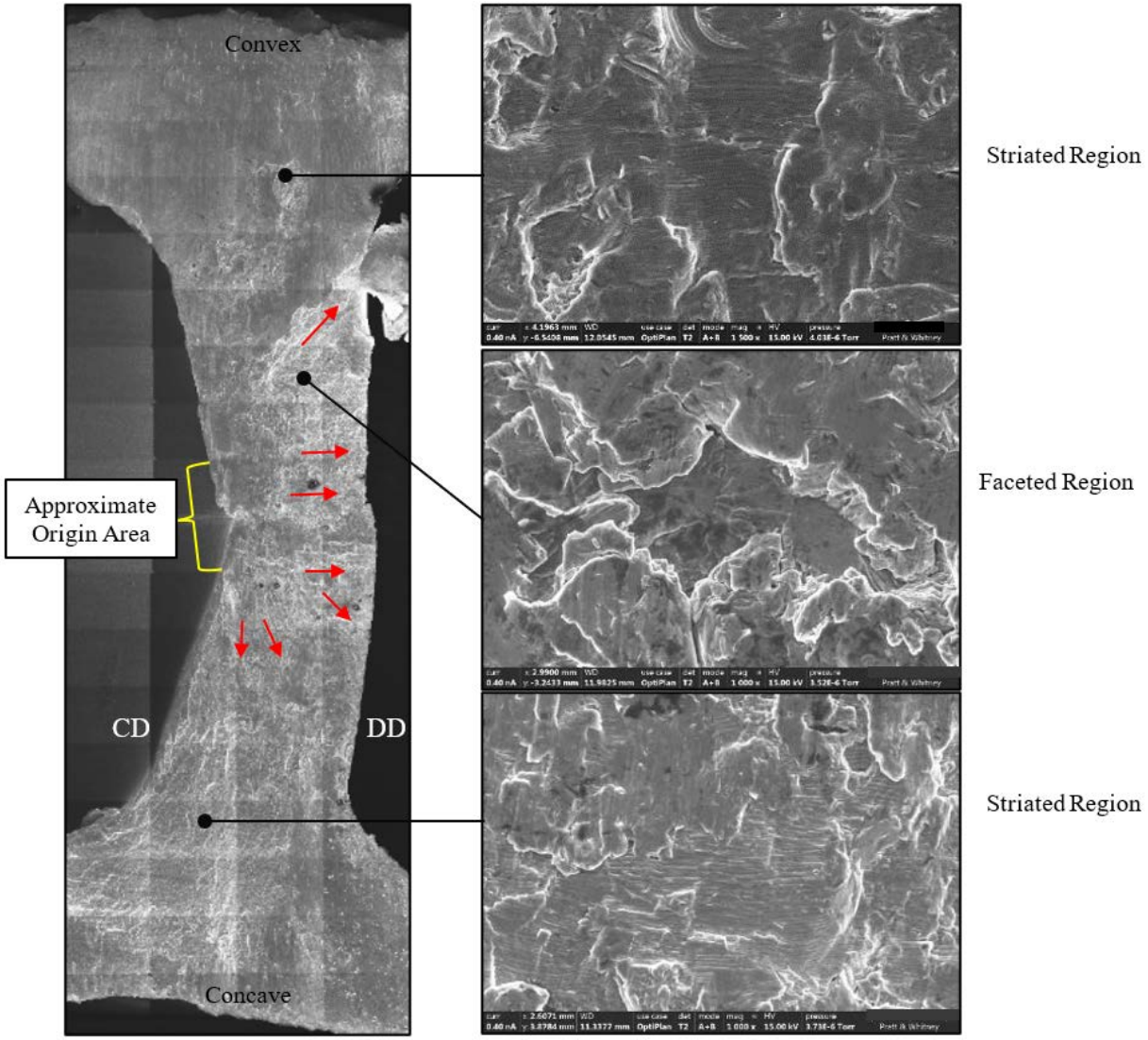

Figure 55: SEM examination confirmed fatigue on the fracture surface. Areas of striated and faceted features were interspersed among large areas of secondary damage/smearing. Features were progressing from an area near the bond line in cavity CD. Due to the damage, the exact origin area could not be identified.

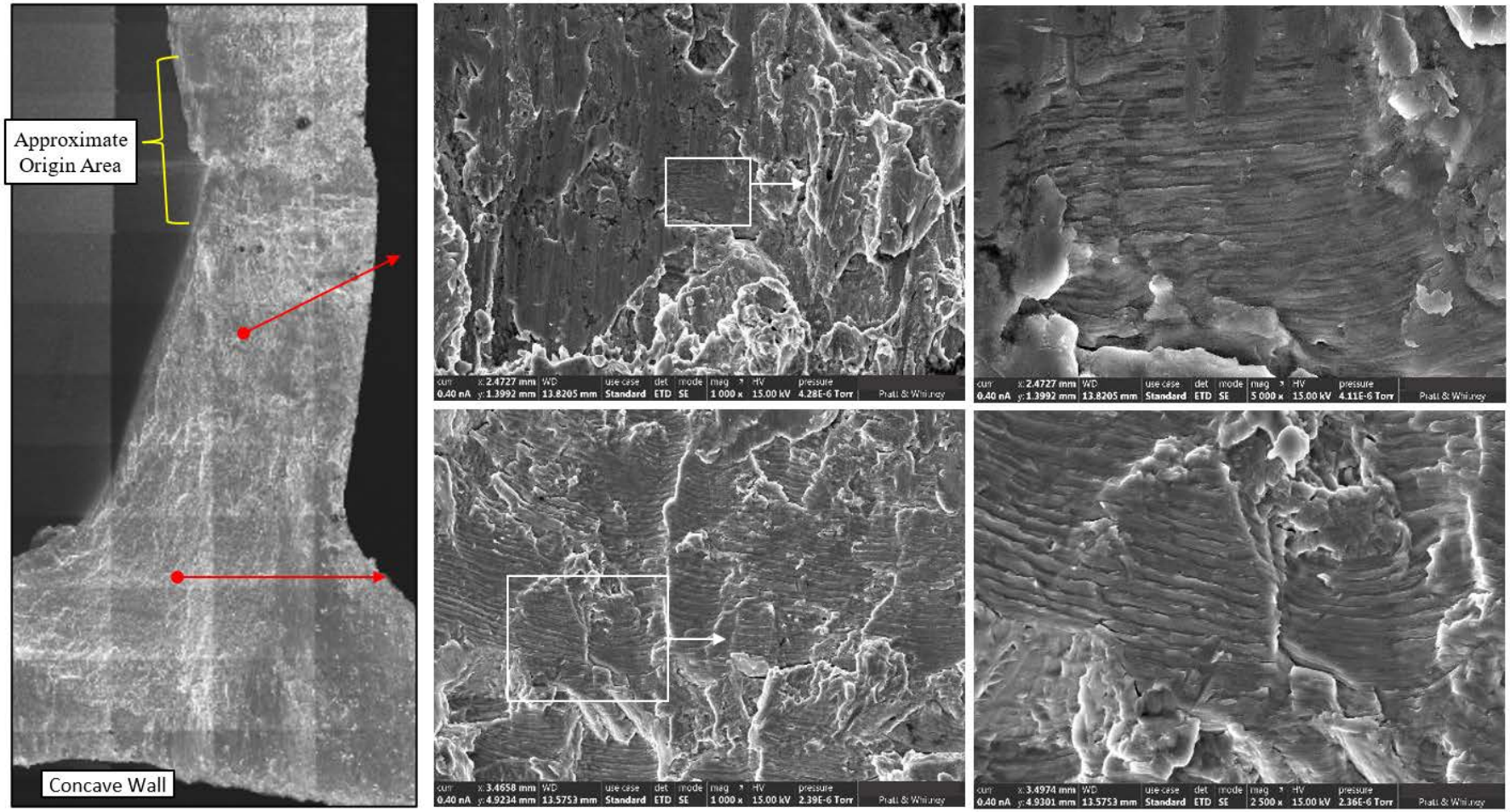

Figure 56: SEM images taken of the crack progression towards the concave wall. The progression exhibited a mix of striated and faceted features. Crack growth rate towards concave wall ranged $6.0x10^{-06}$ – $4.9x10^{-05}$ in/cycle.

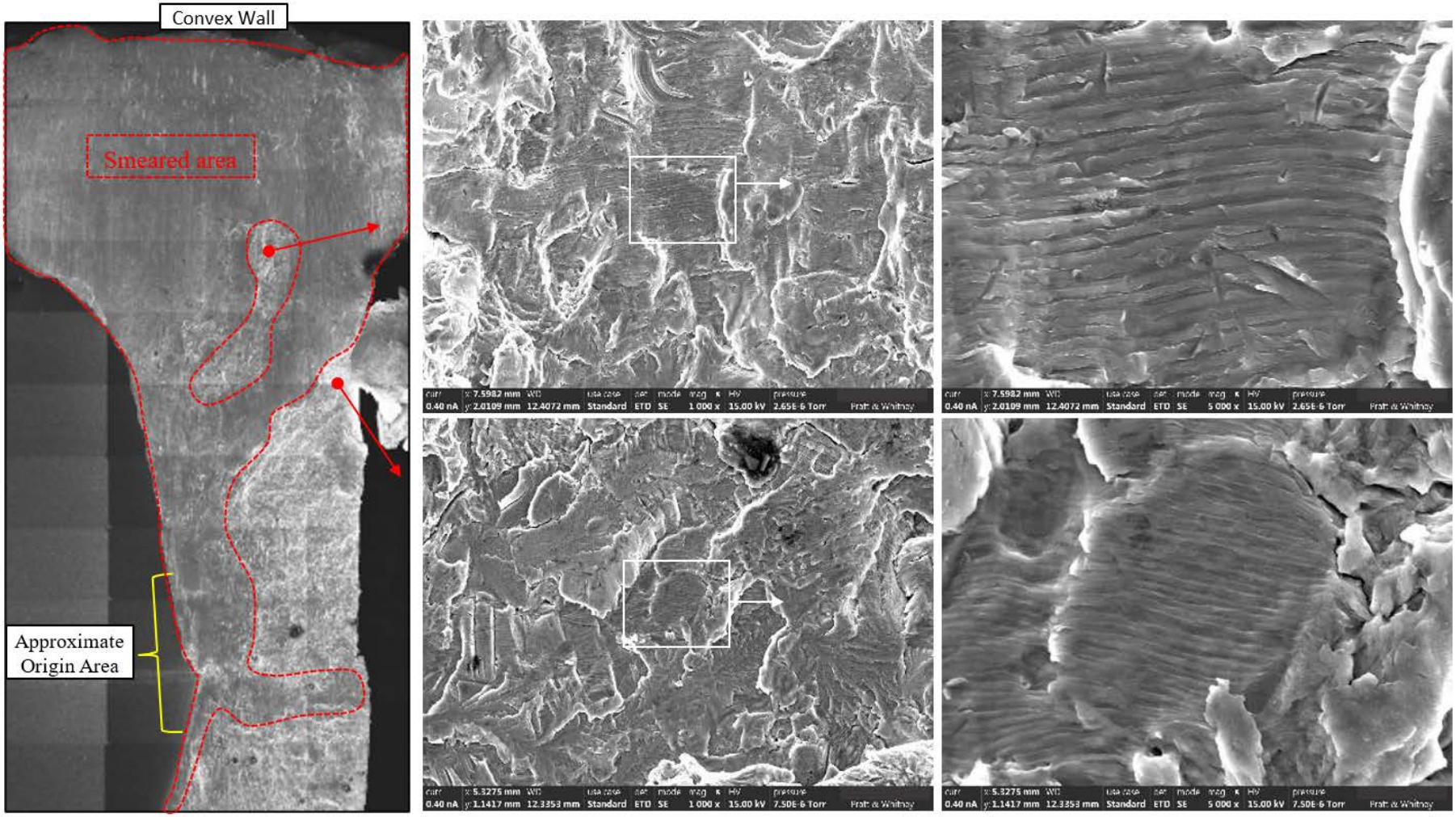

Figure 57: SEM images taken of the crack progression towards the convex wall. The progression exhibited a mix of striated and faceted features. Crack growth rate towards convex wall ranged $6.5x10^{-06}$ – $2.9x10^{-05}$ in/cycle. The areas circled in red were smeared. The exact origin could not be identified due to the damage.

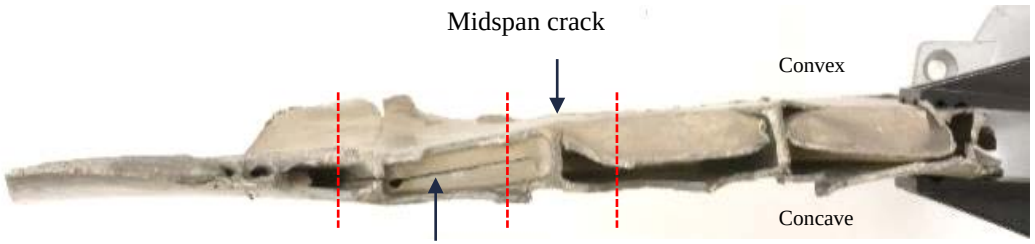

Bond Line Separation (between cavity CD and CE)

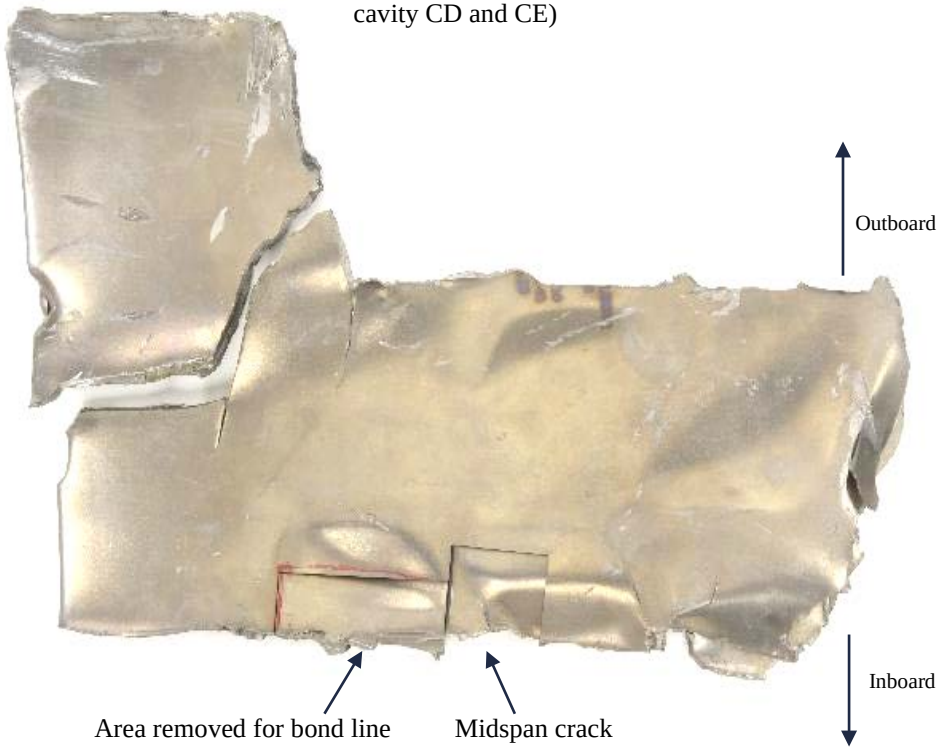

Figure 58: The bond line in the cavity adjacent to the crack was separated. It was removed from the part as shown above for further evaluation.

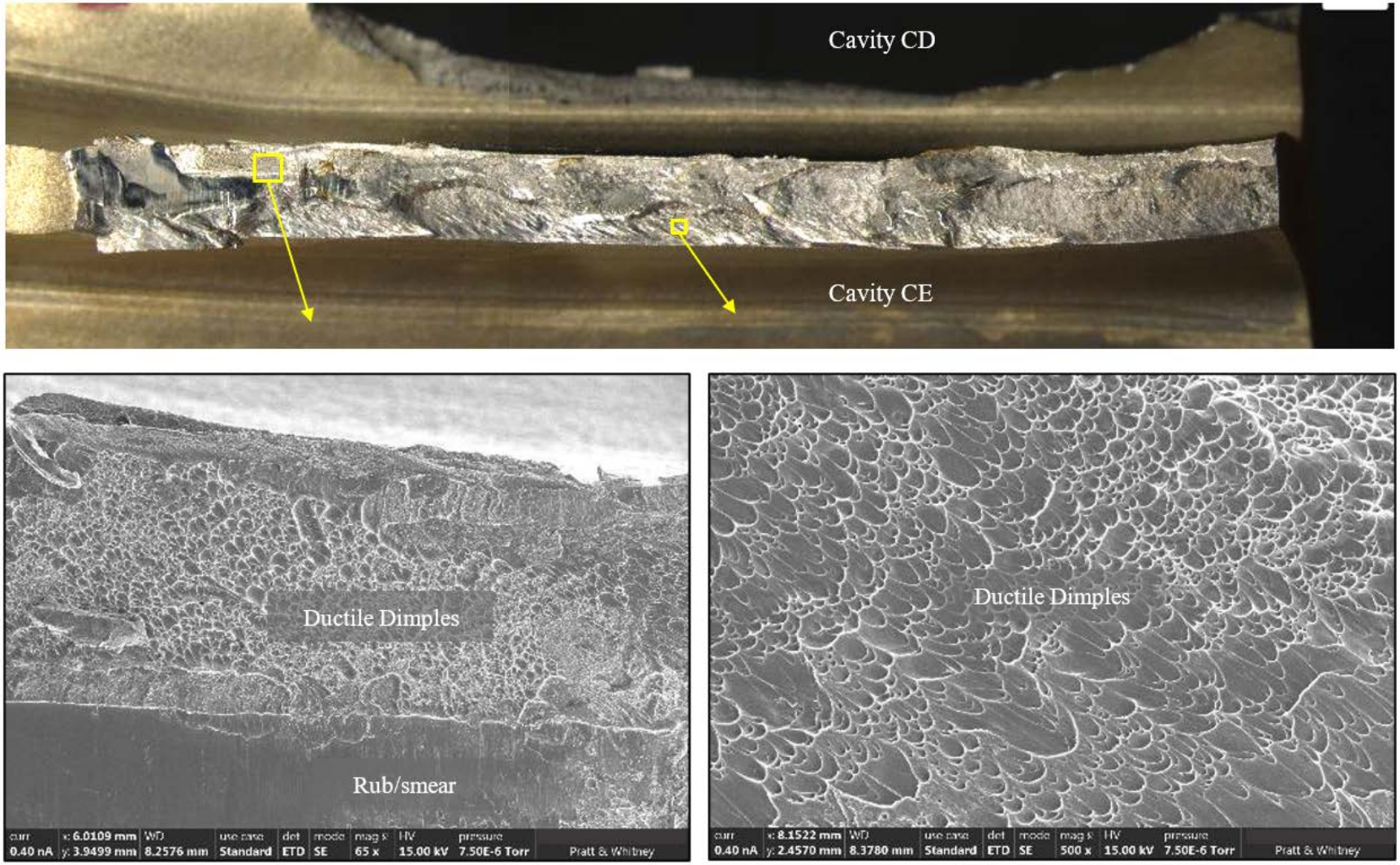

Figure 59: Binocular and SEM examination of the disbonded rib between cavity CE and CD identified elongated ductile dimples and rub/smear. No fatigue was observed.

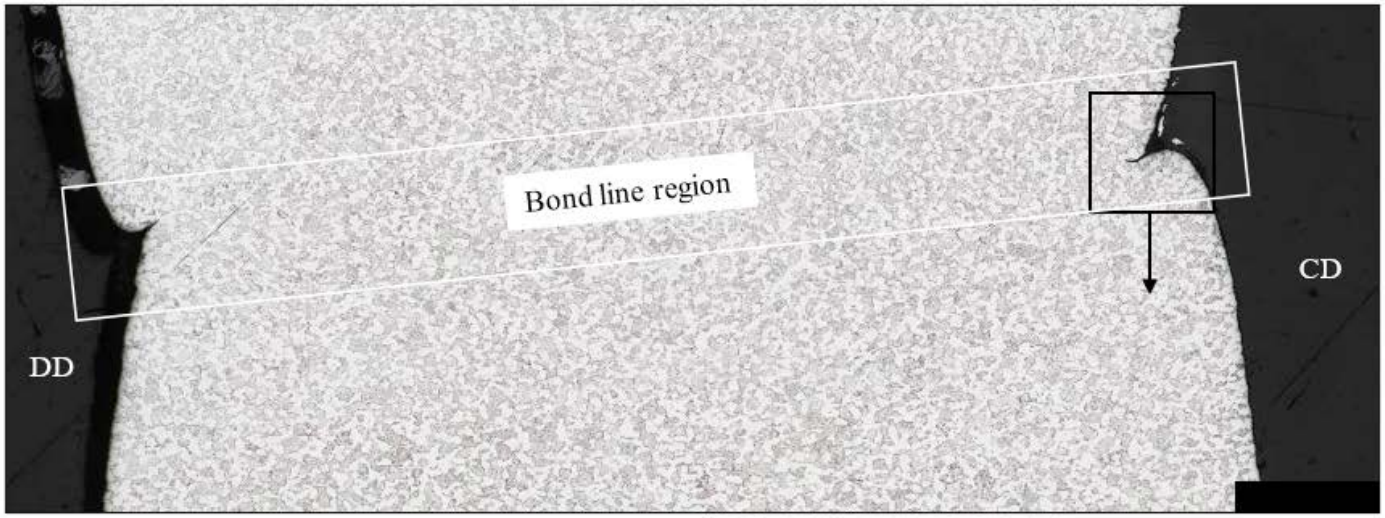

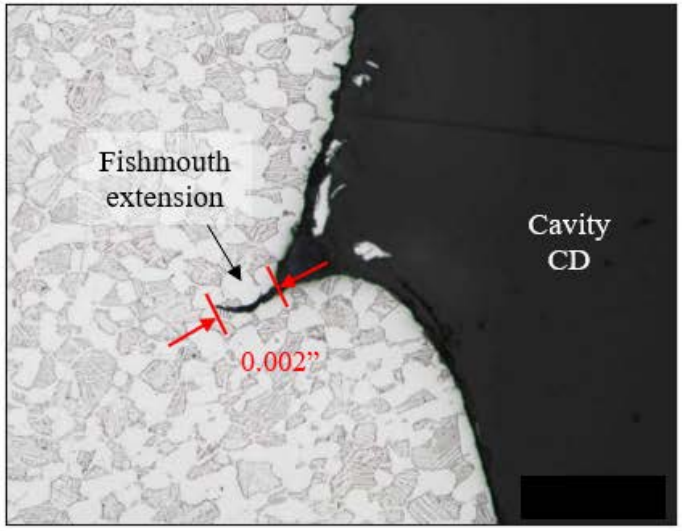

Figure 60: Metallographic images showing a transverse section through an area of the spanwise rib that appeared intact just outboard of the midspan crack in the outboard blade fragment. No voids or unbonded areas were observed. The fishmouth feature extended 0.002” which was acceptable per bond quality requirements.

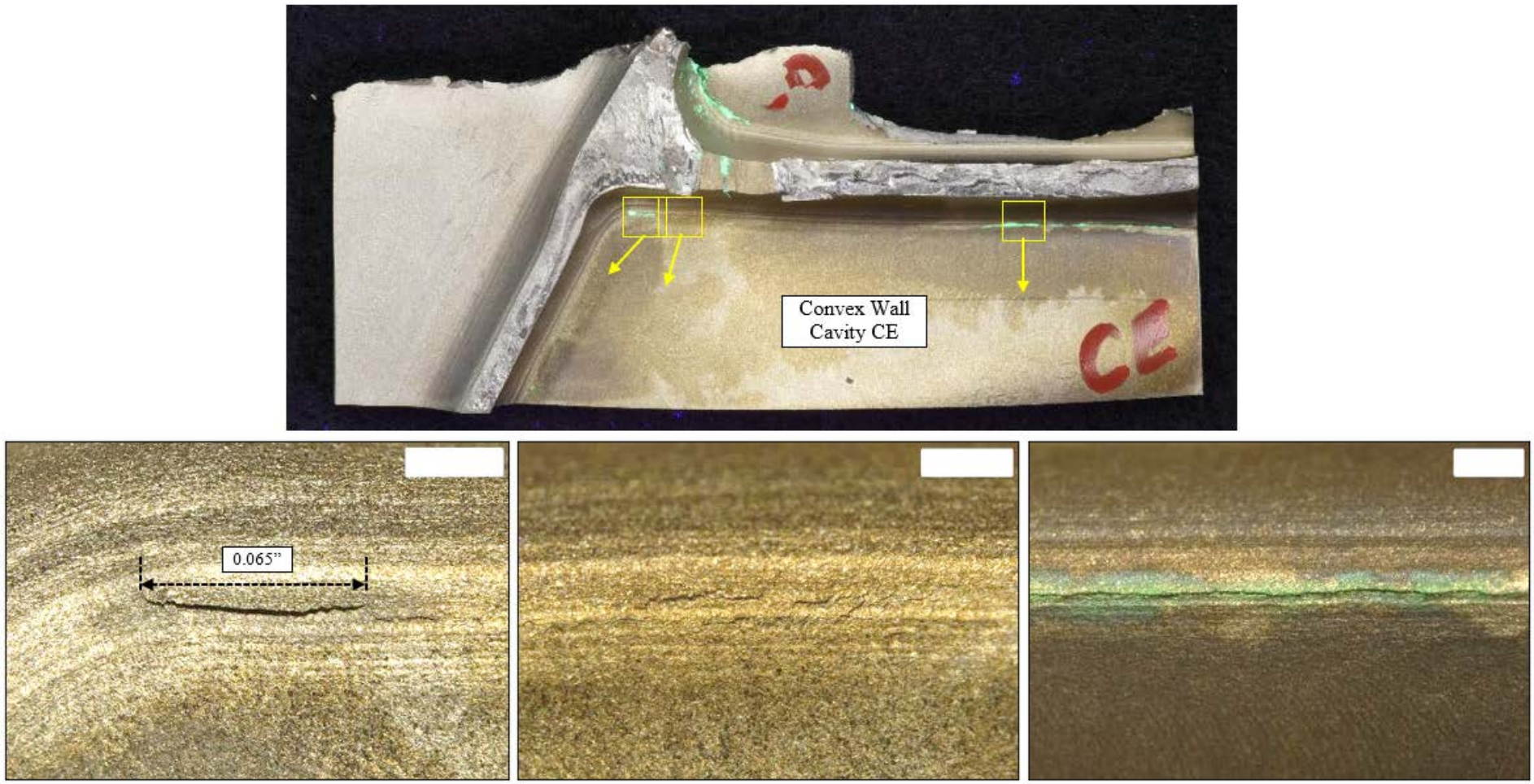

Figure 61: Images showing crack-like indications in the radius between the convex wall skin and the chordwise rib between cavities CE and CD.

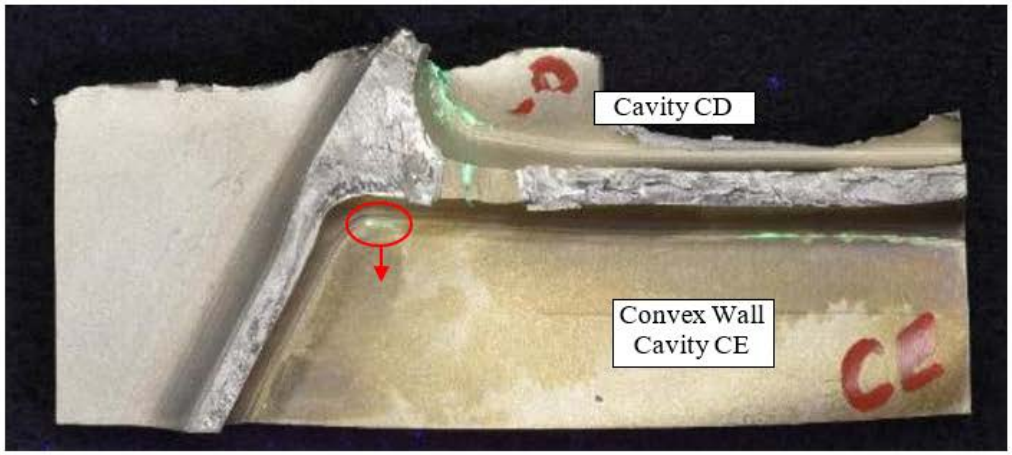

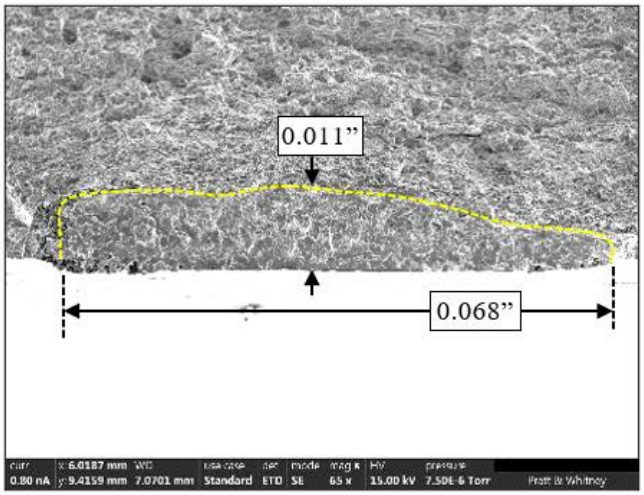

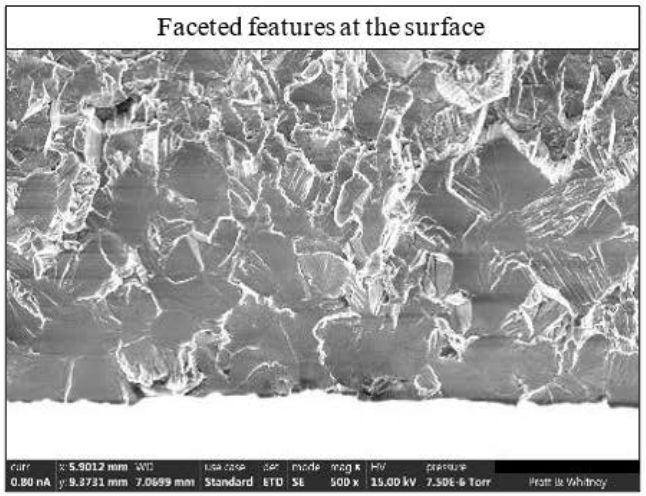

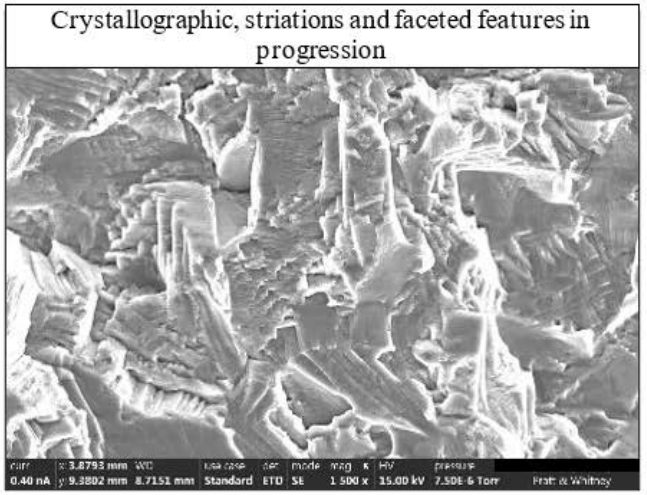

Figure 62: SEM images showing the fatigue features at the crack that was broken open in cavity CE.

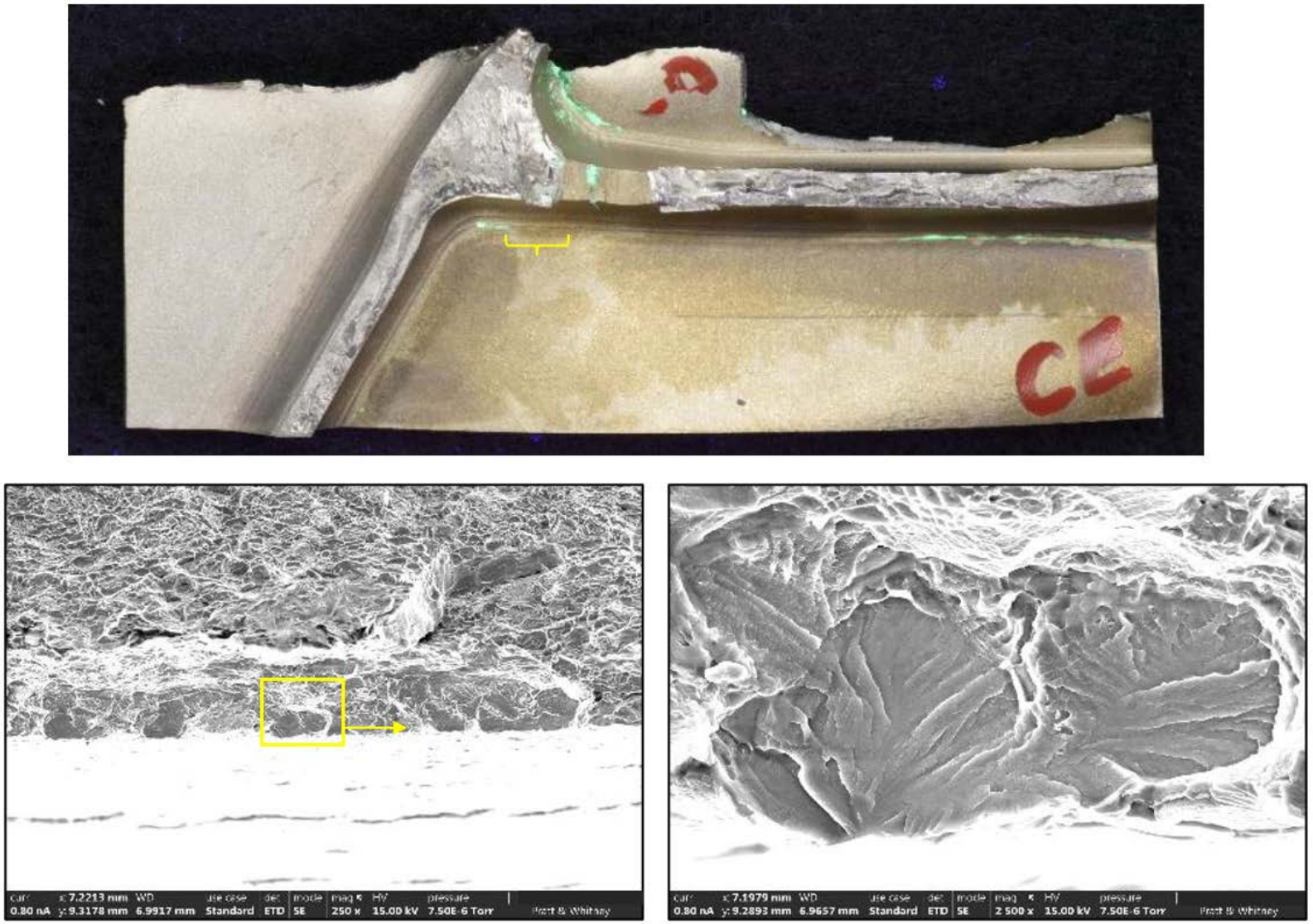

Figure 63: SEM images showing faceted areas one or two grains deep along the surface in the force fractured region outside of the broken open crack.

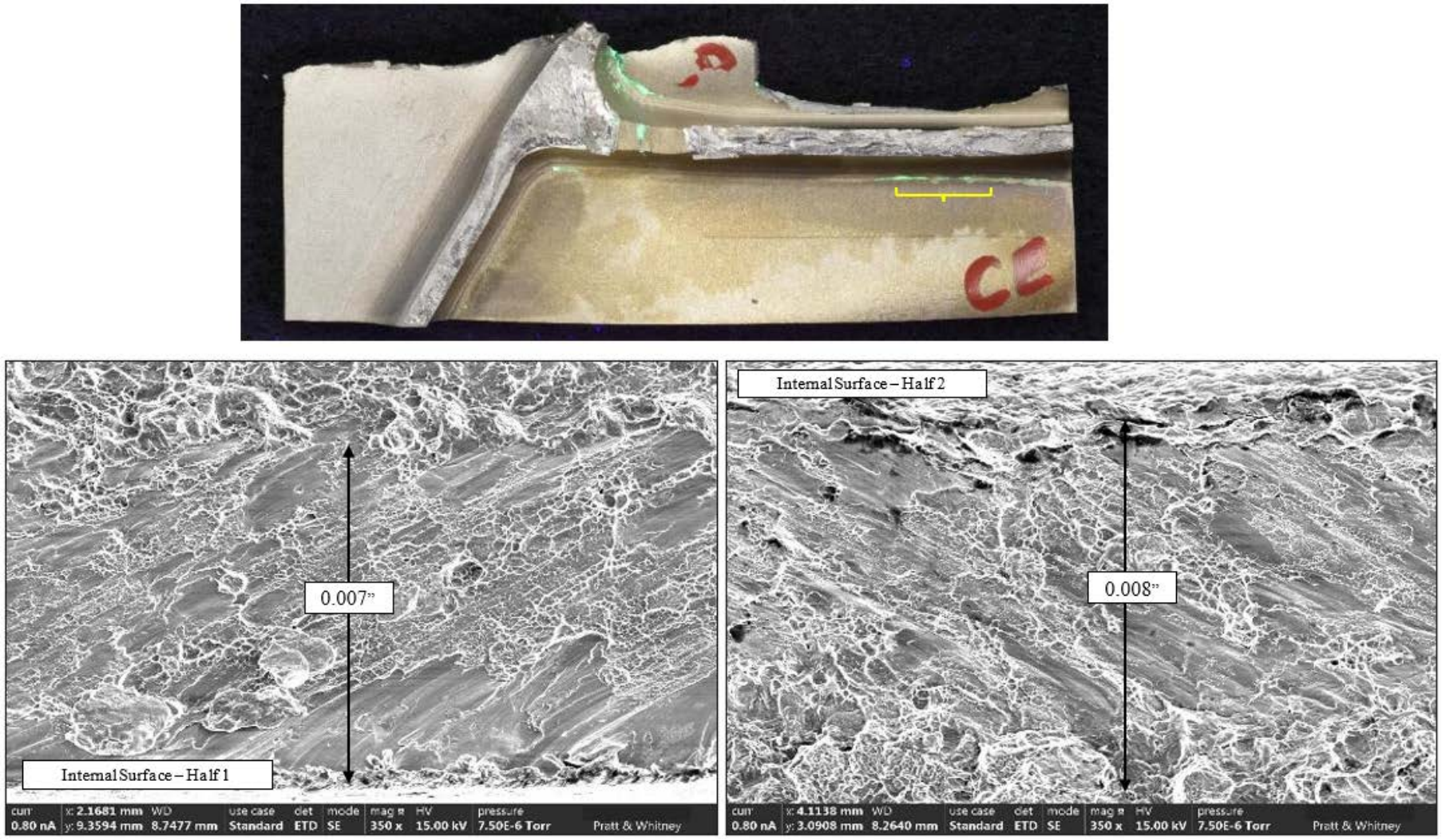

Figure 64: SEM images showing smear and ductile dimple features at an area at the TE of cavity CE that was force fractured open.

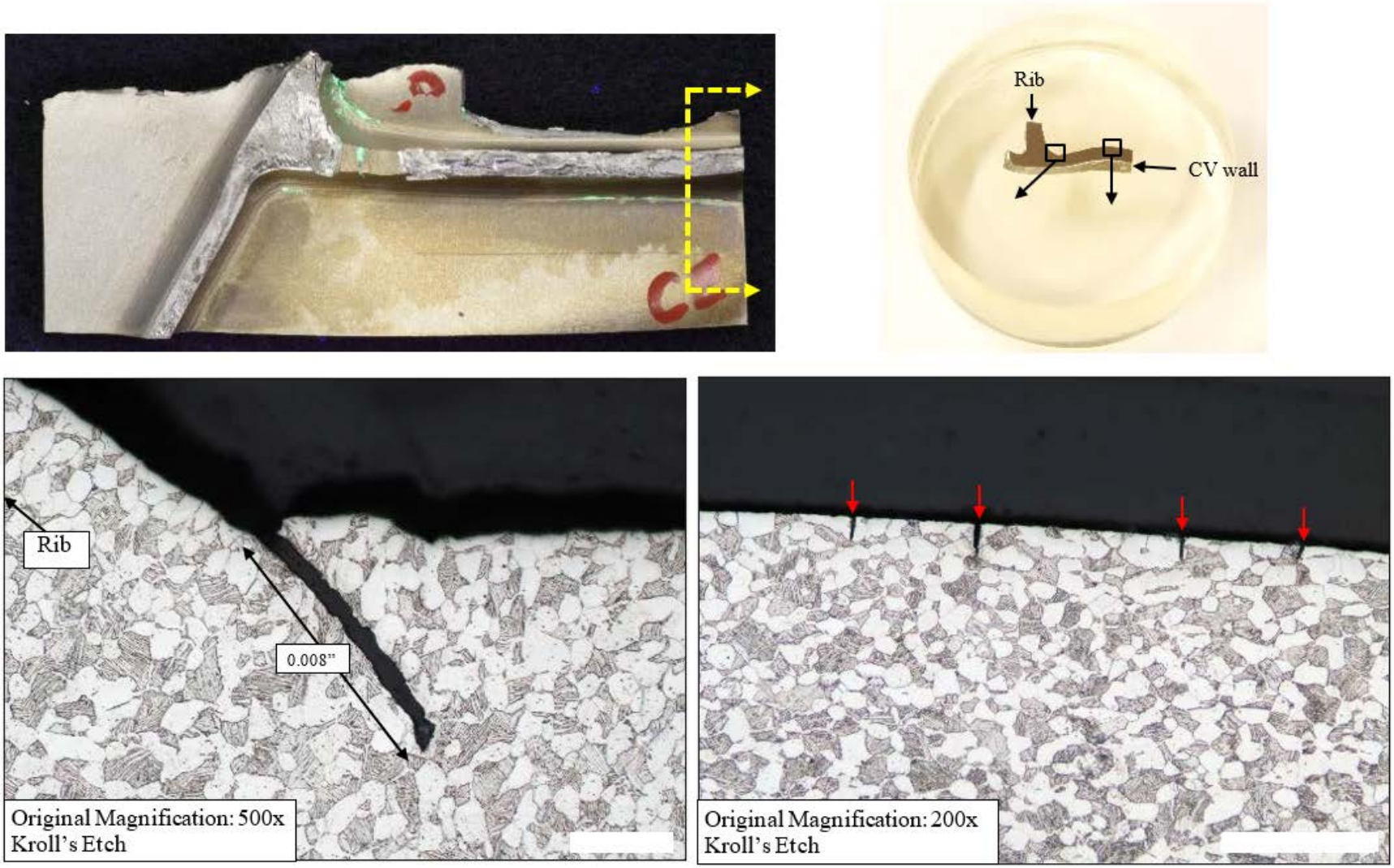

Figure 65: Metallographic images of the longitudinal section through the chordwise rib at the TE side of cavity CE.

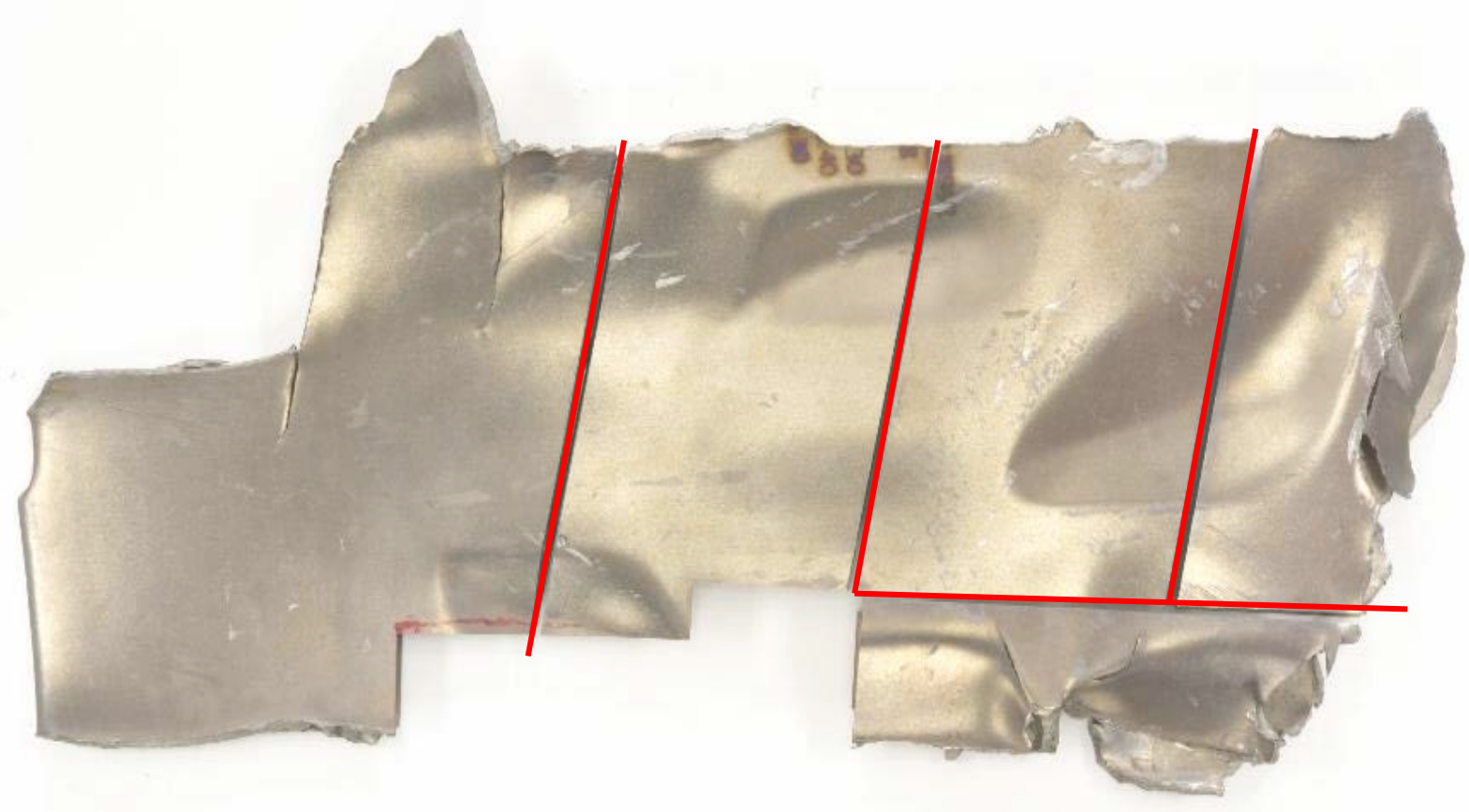

Figure 66: Image showing how the outboard midspan fragment was sectioned via wire EDM for visual access to the cavities.

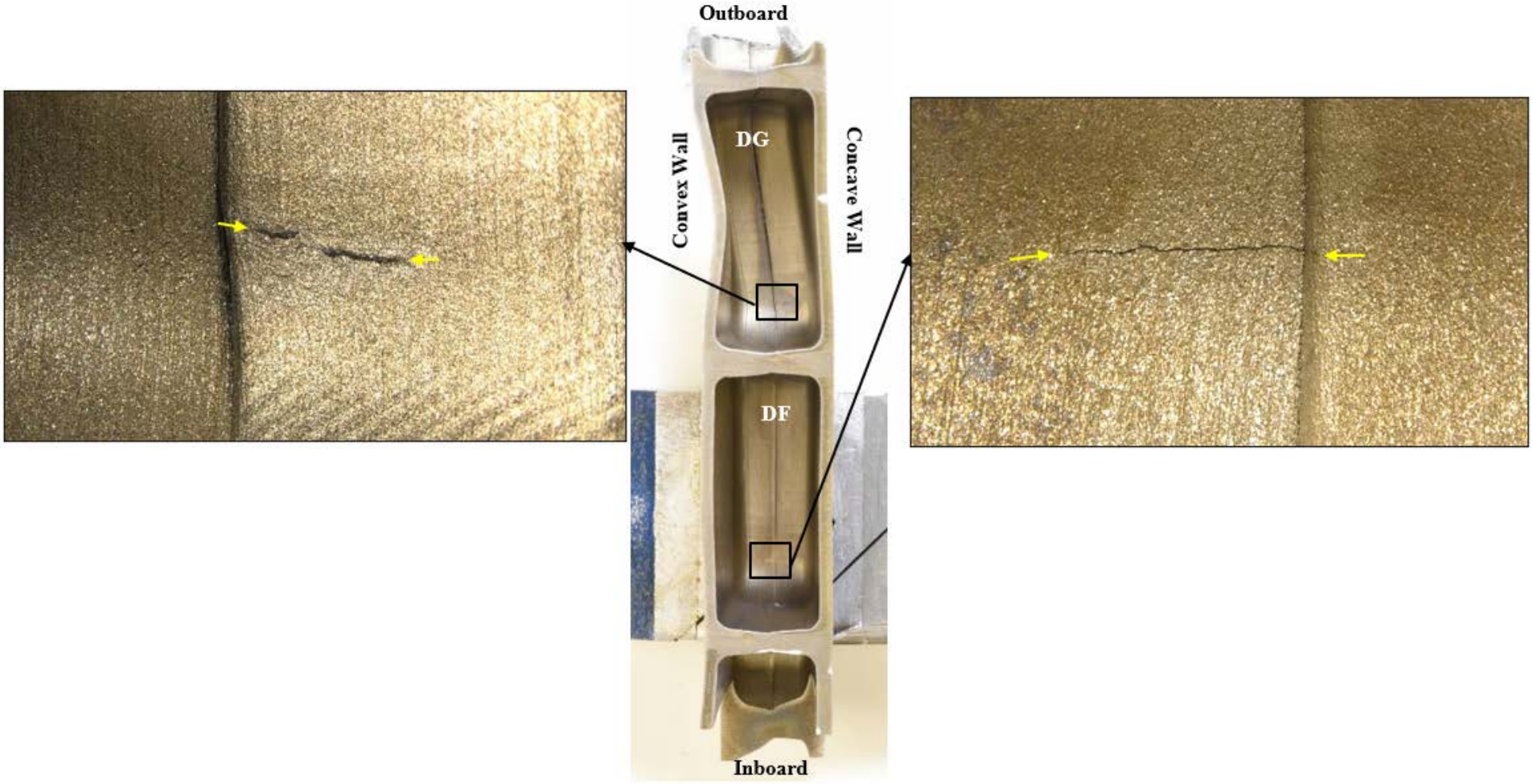

Figure 67: Images of the cracks observed at the forward sides of cavities DF and DG. Both cracks were located just outboard of the chordwise ribs.

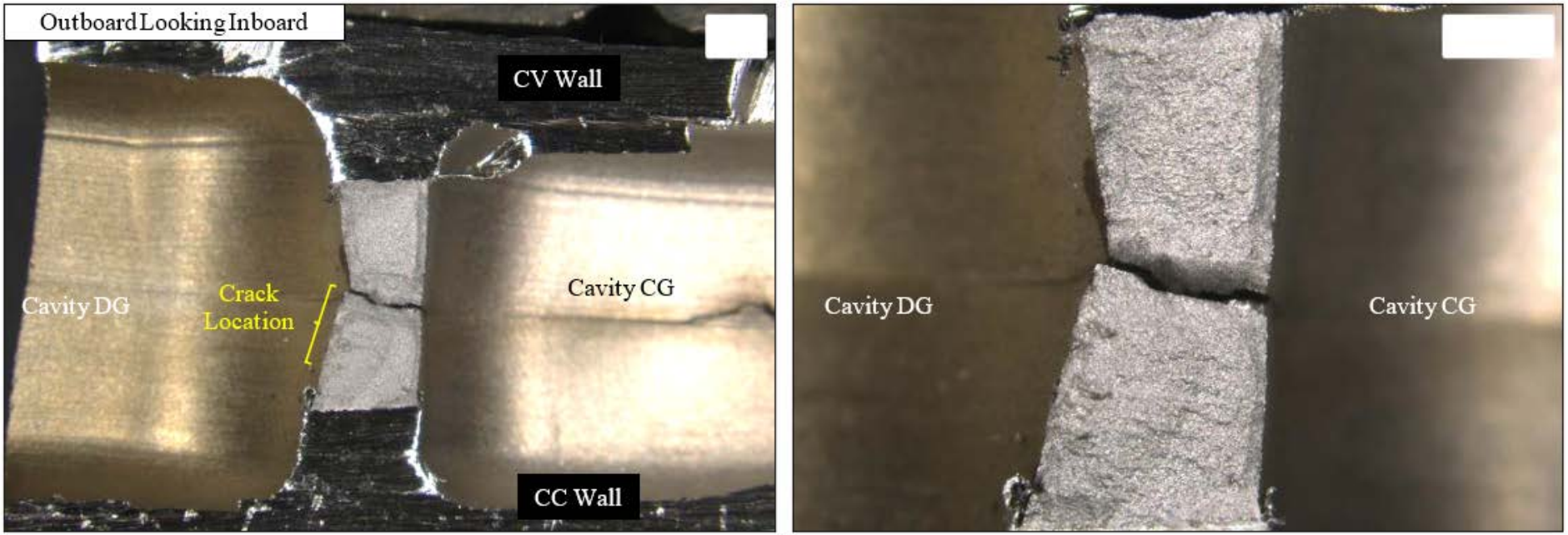

Figure 68: Images of the broken open crack indication in cavity DG showing no fatigue features.

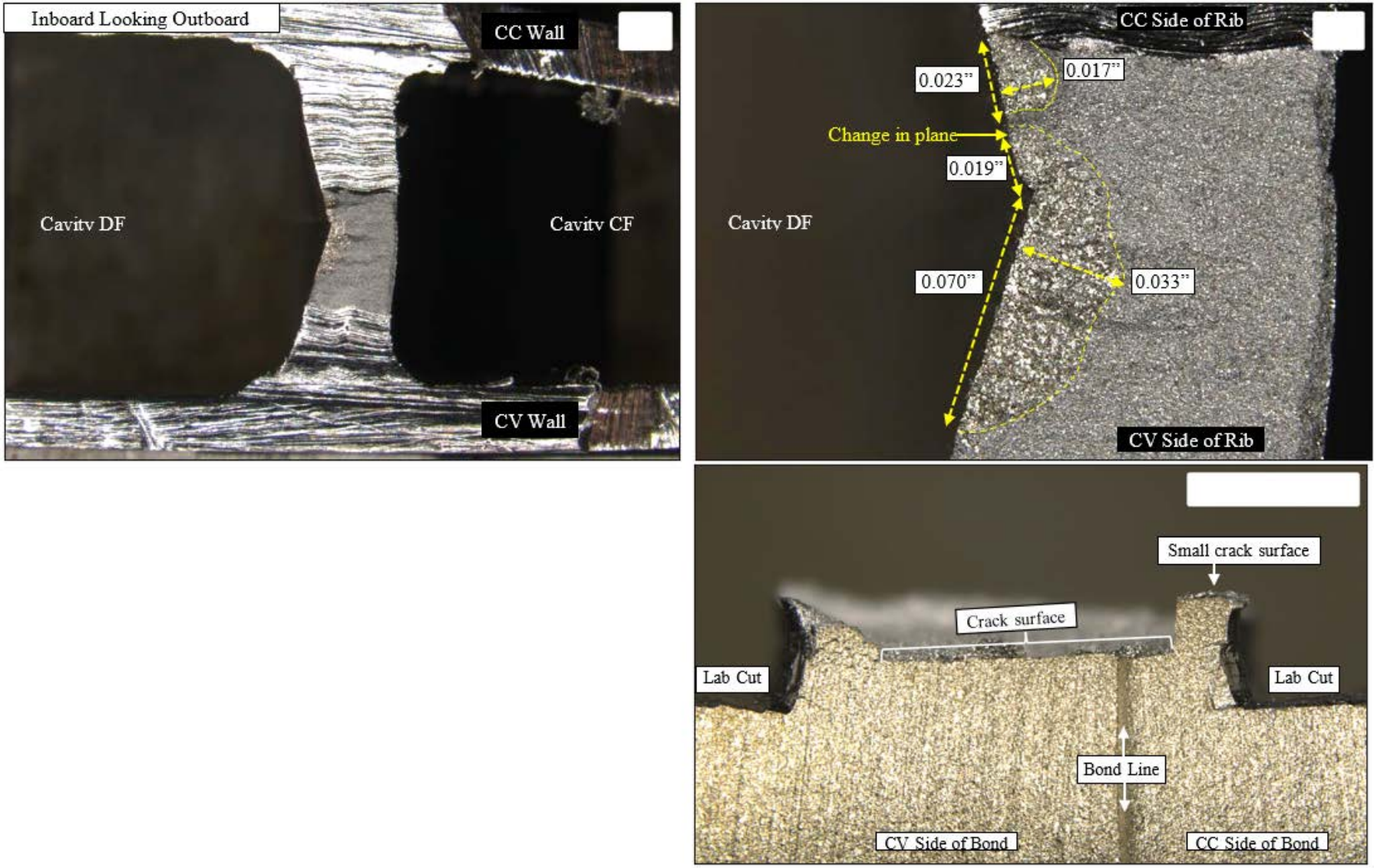

Figure 69: Images showing the broken open cracks in cavity DF.

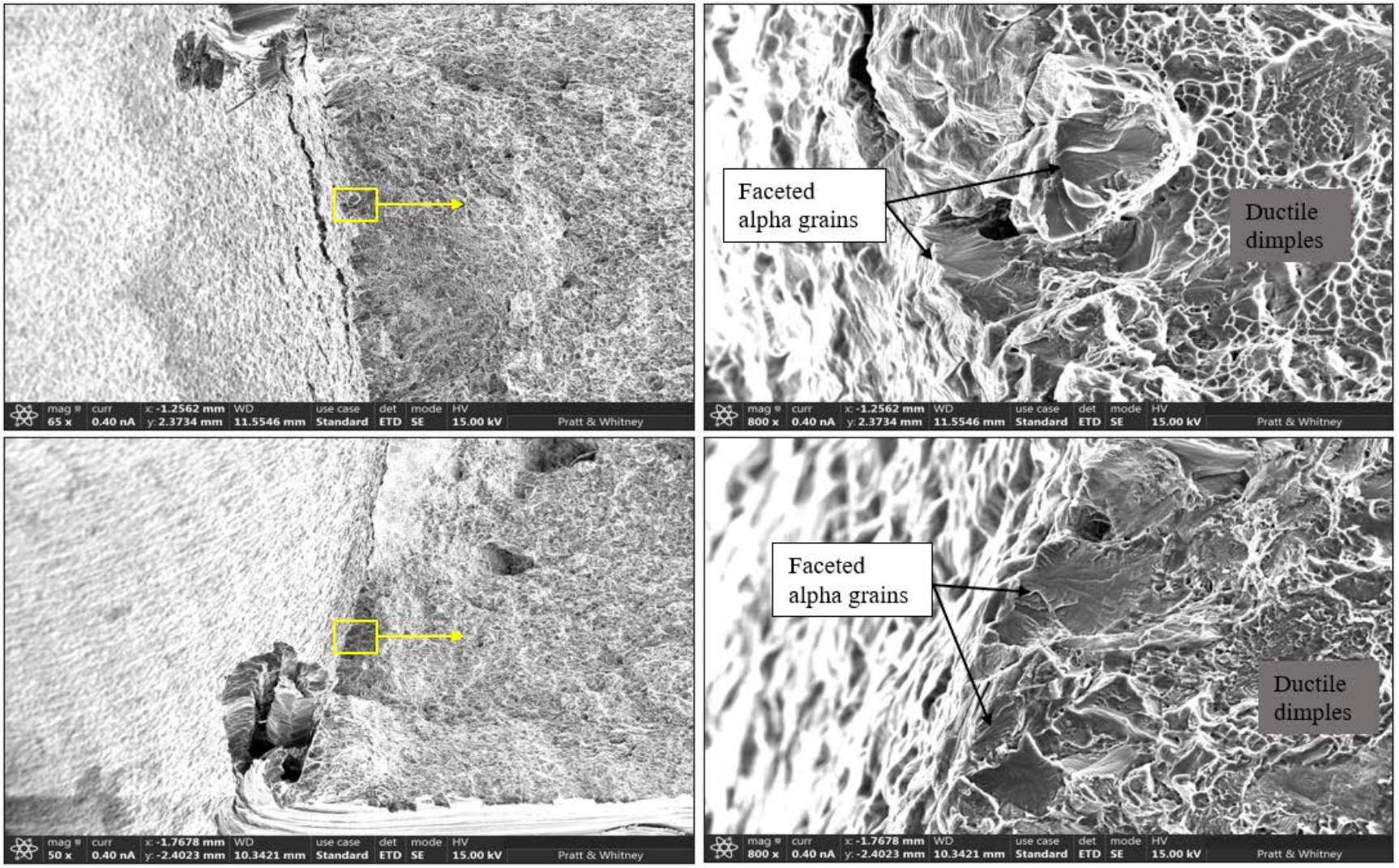

Figure 70: SEM images showing the features in cavity DG after force fracturing the crack open. Faceted alpha grains were observed along some of the fracture at the edge of the cavity surface. The remainder of the features exhibited ductile dimples, indicative of overstress.

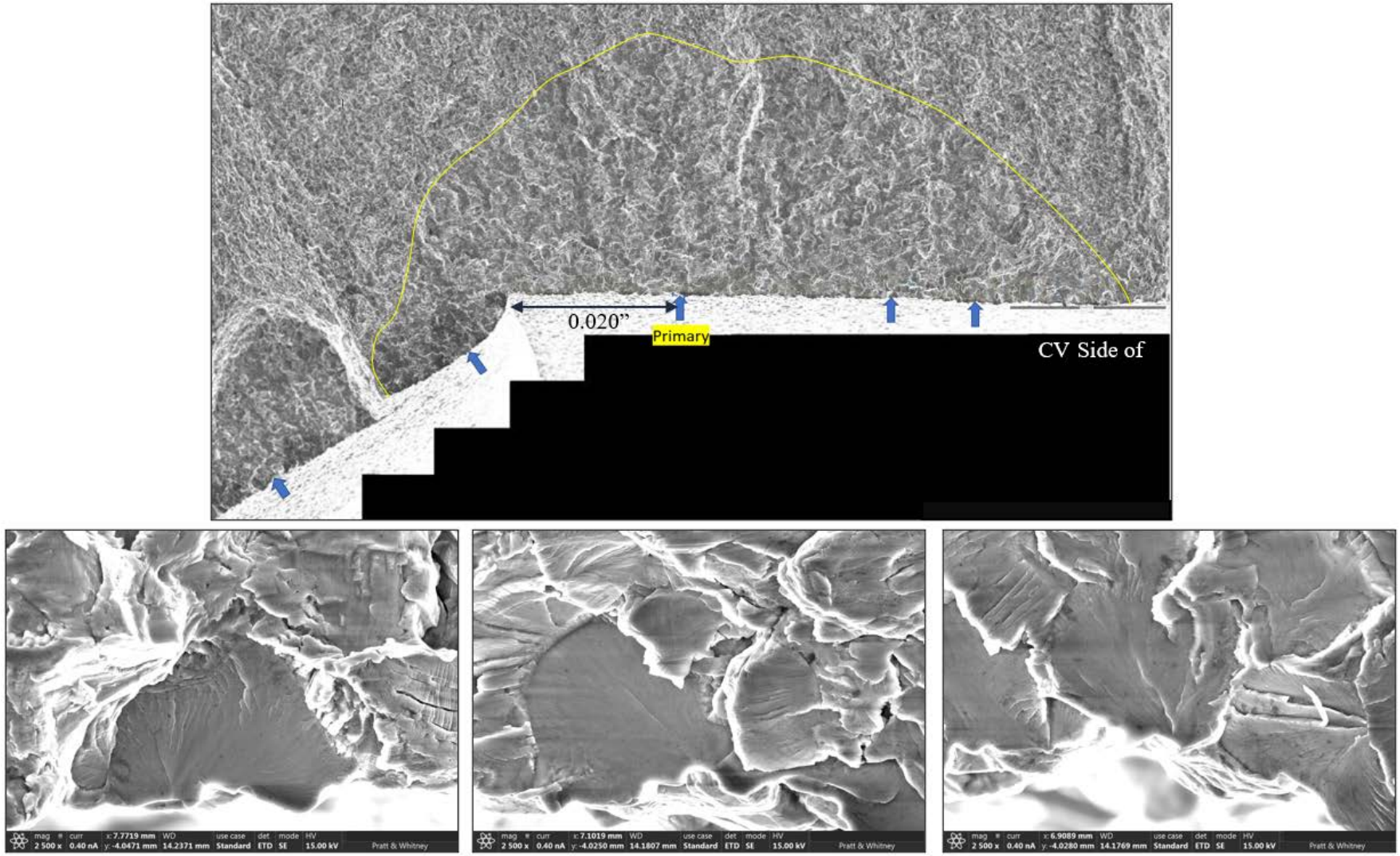

Figure 71: SEM images showing multiple origins identified on the crack in cavity DF (blue arrows). The origins were consistent with surface grain origins.

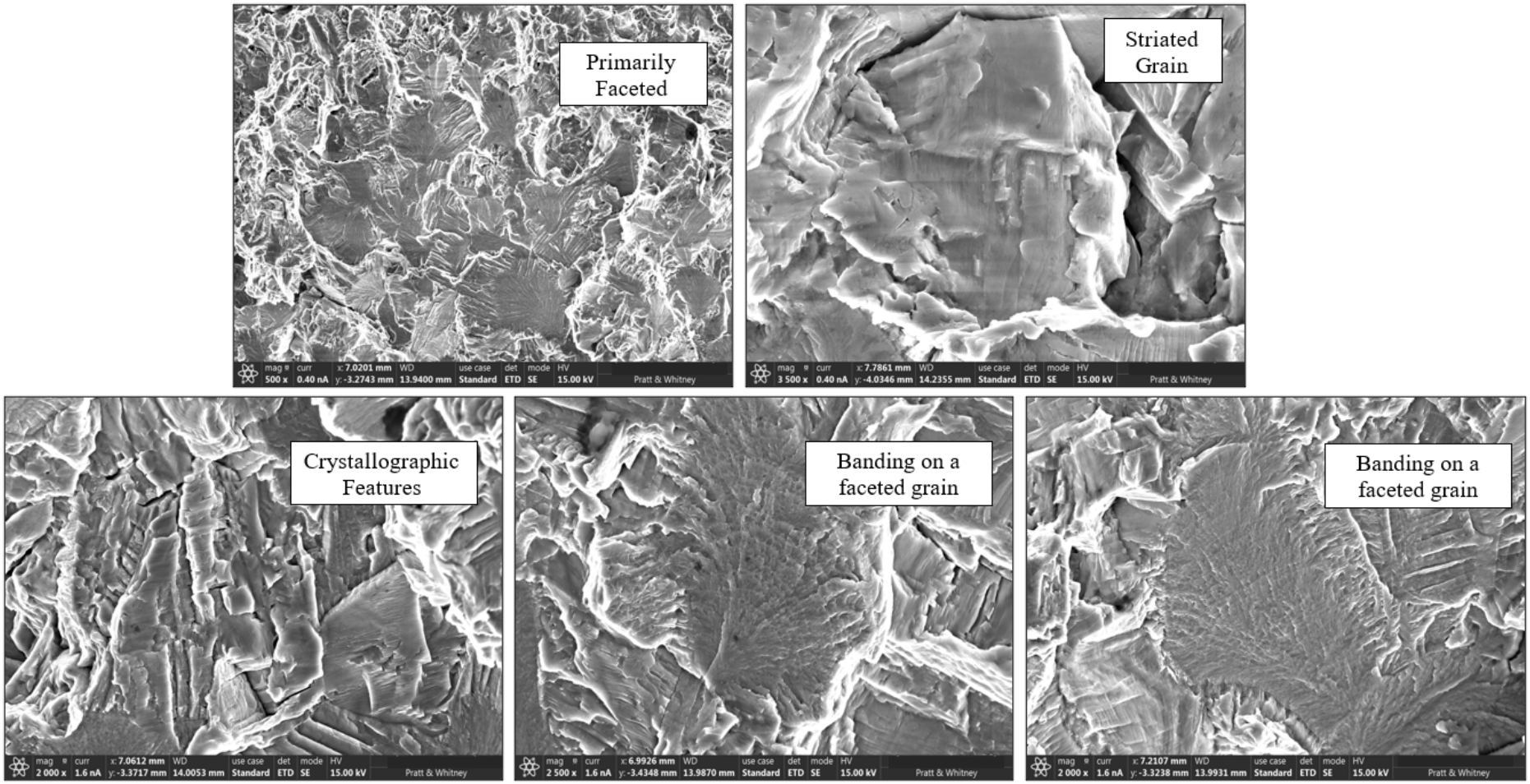

Figure 72: SEM images of crack progression features in cavity DF. These fatigue features indicate low delta K cracking.

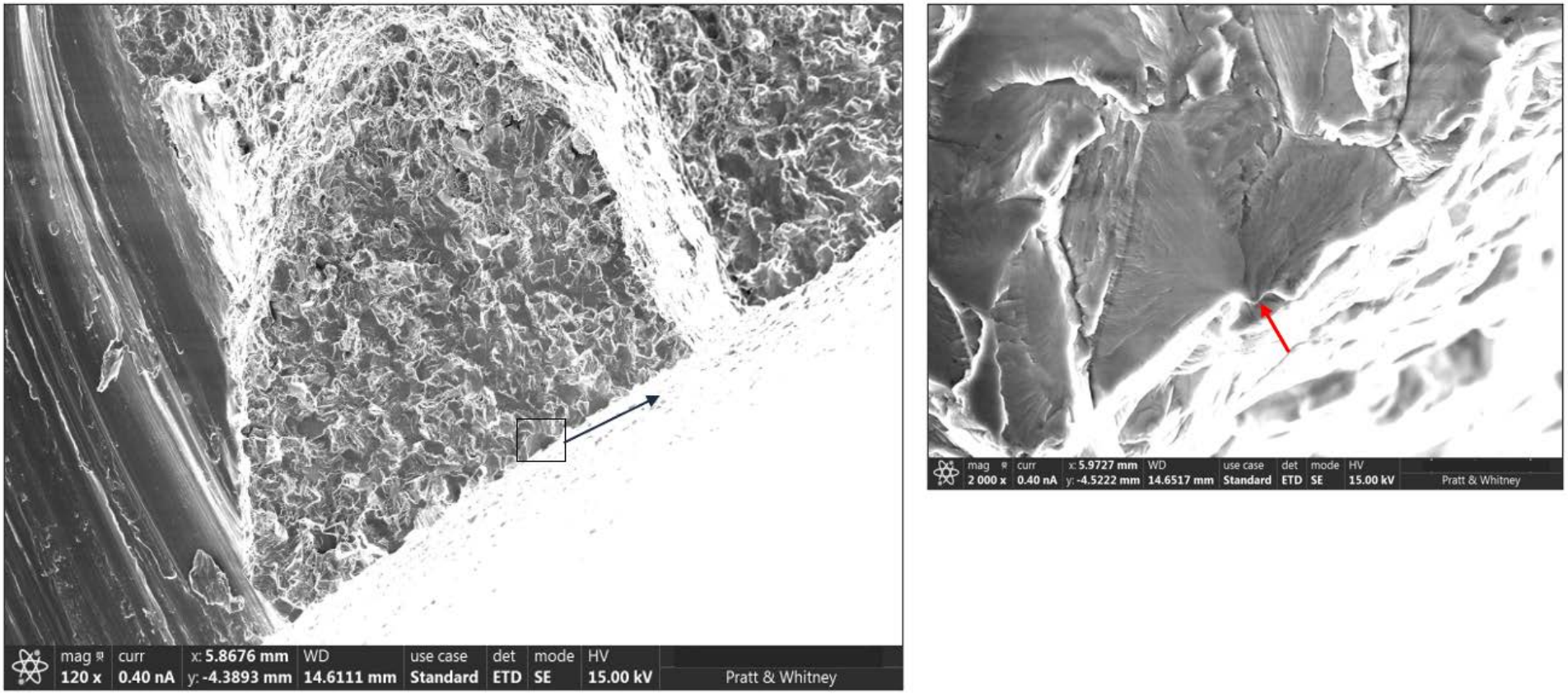

Figure 73: SEM images of the smaller crack on the concave side of the rib in cavity DF. A single surface origin was observed (red arrow).

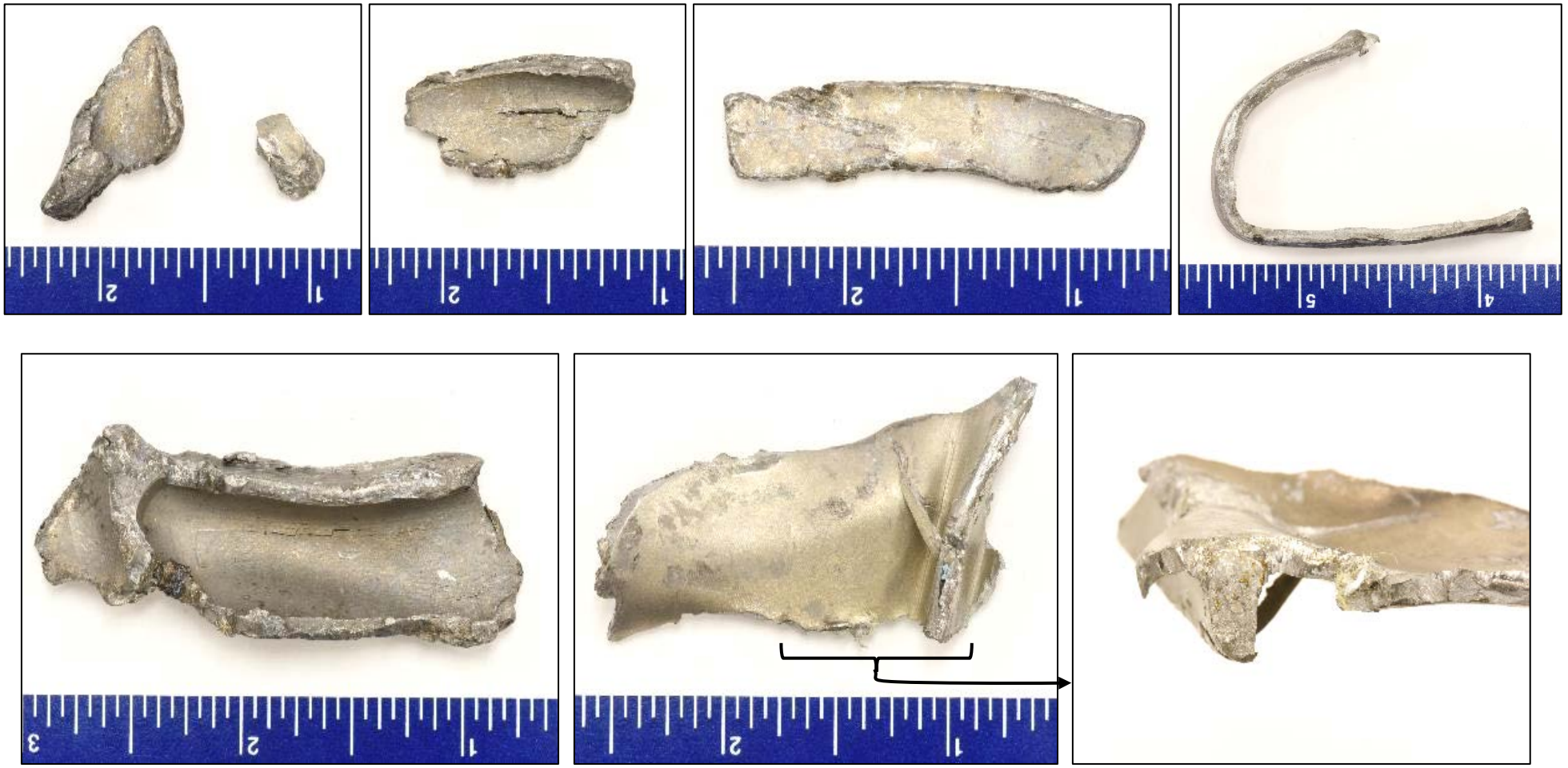

Figure 74: Images of the small blade fragments returned to P&W for evaluation. The fragments exhibited extensive secondary damage.

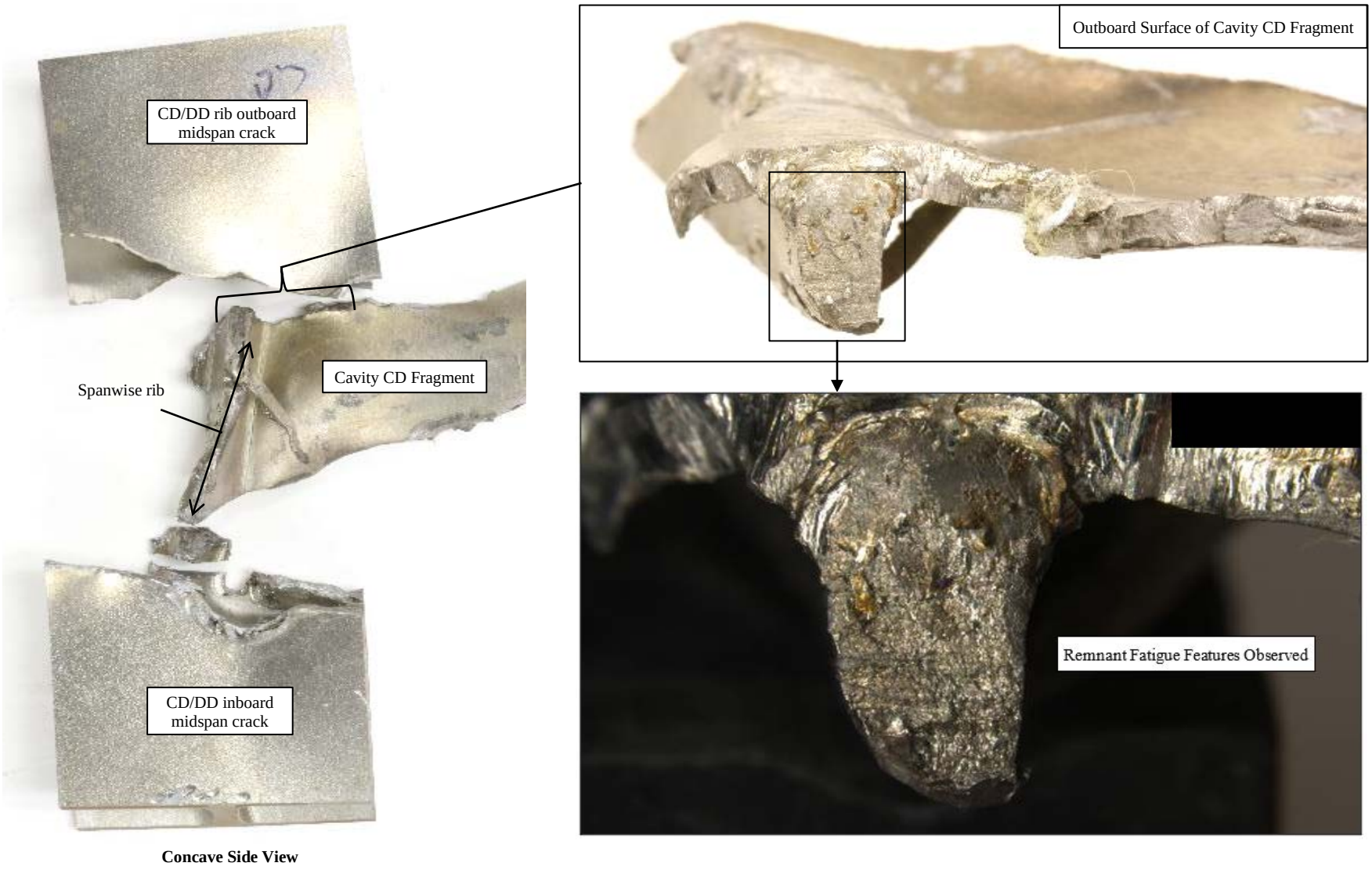

Figure 75: Images showing how the small fragment mated with the other blade pieces in cavity CD. The fatigue features observed on the fragment correlated with the midspan crack that was identified on the larger outboard midspan fragment.

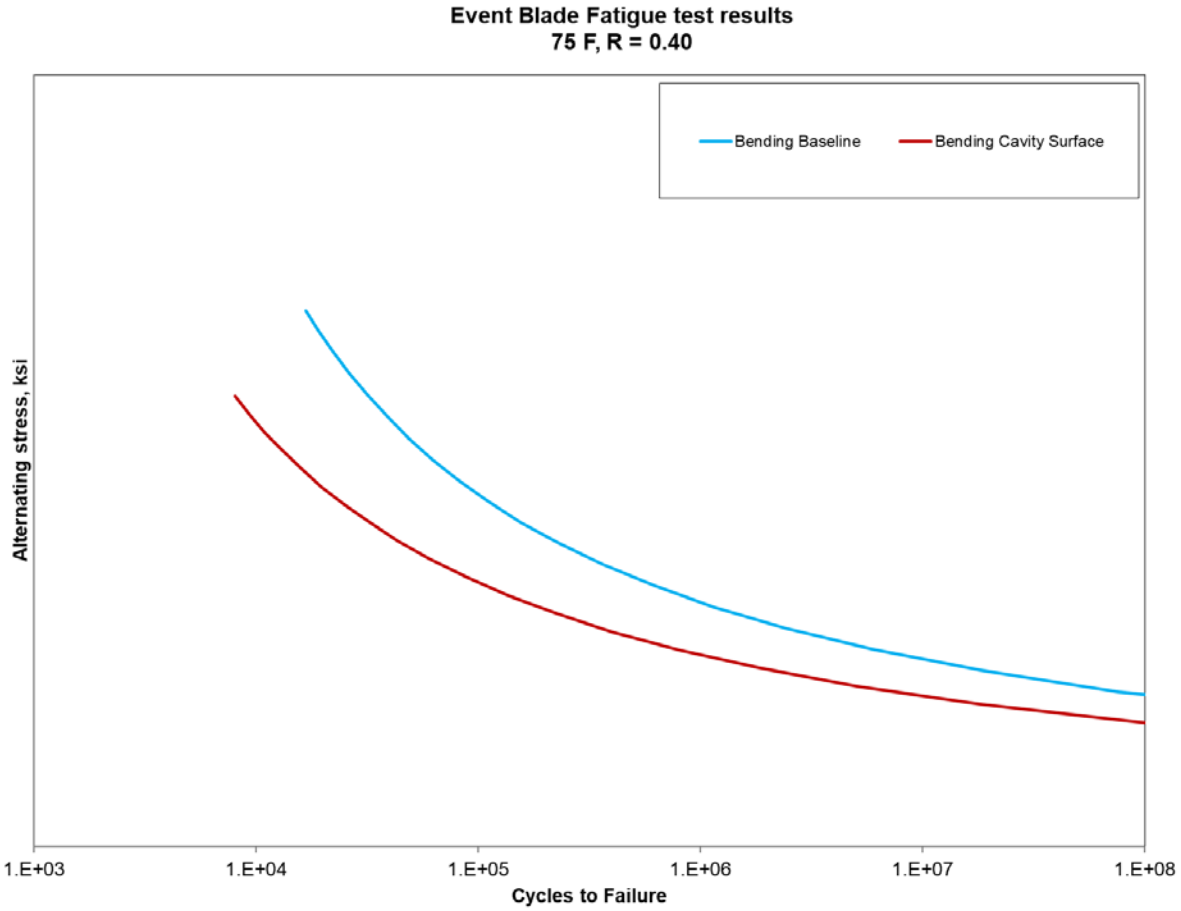

Figure 76: Event blade fatigue test results. The samples representing the as-produced cavity surface from the root of the subject event blade exhibited lower fatigue capability compared to the bulk material specimen from this blade.

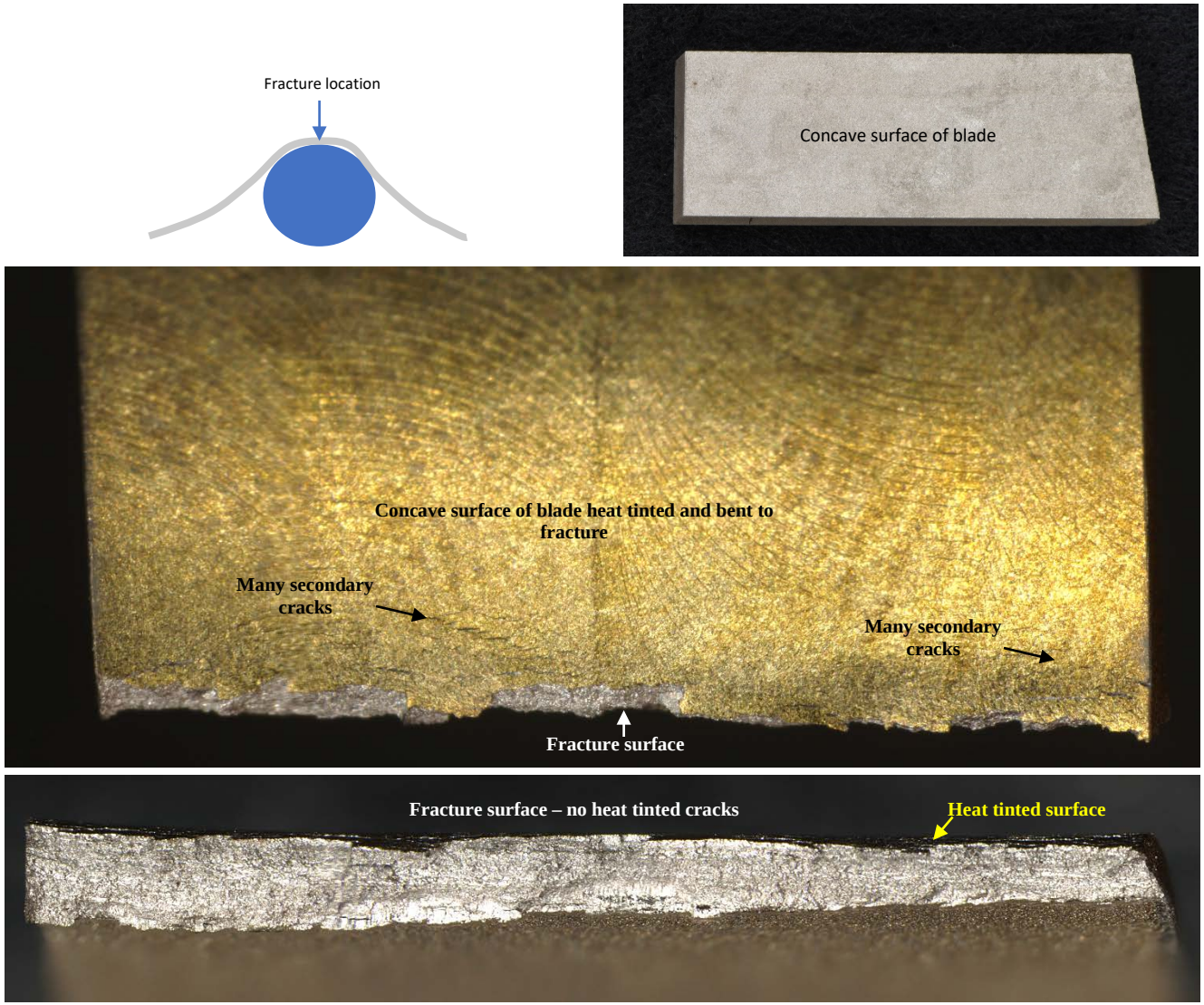

Figure 77: Images showing the heat tinted bend test sample after fracturing. Multiple secondary cracks were observed on the bent surface. No heat tint areas were observed on the fracture surface.

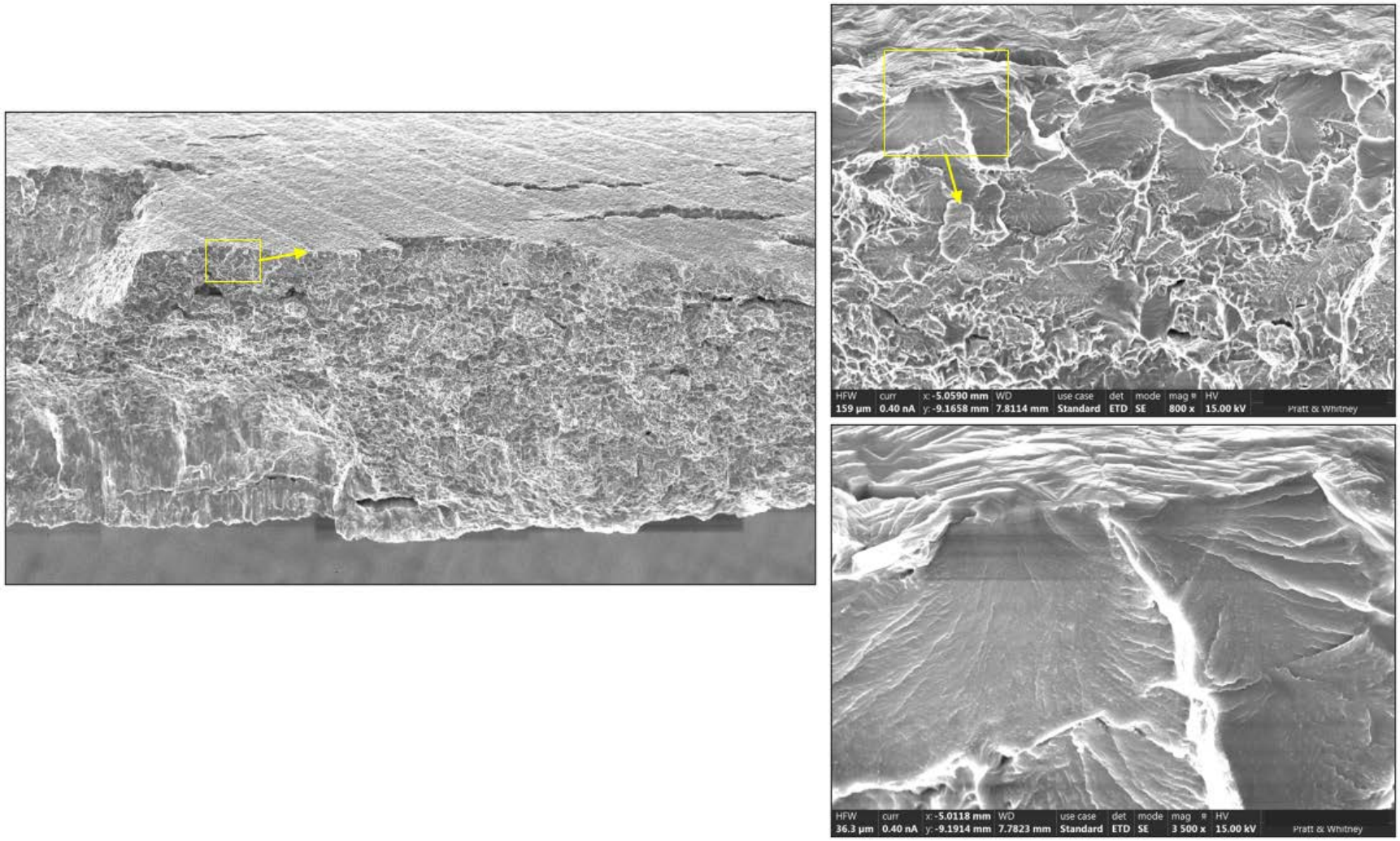

Figure 78: SEM images showing a layer of faceted grains along the surface of the bend test fracture.

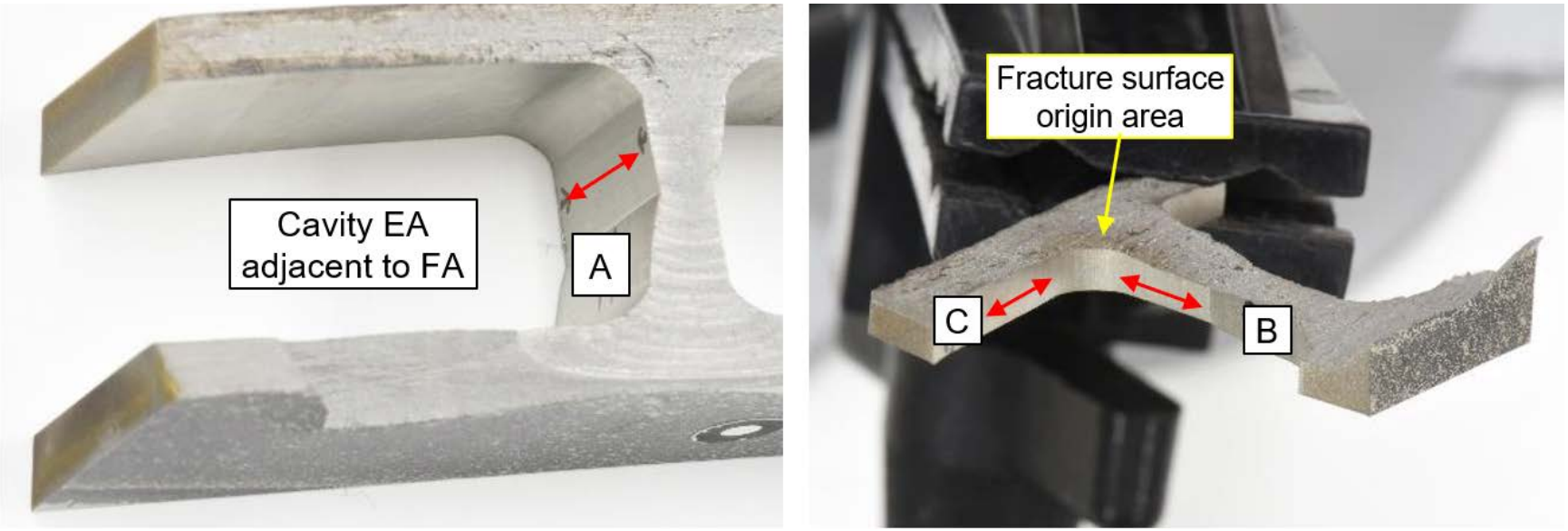

Figure 79: Surface roughness measurements were taken with a Mahr® profilometer using a 4mm stylus along the red lines shown in the images above. Ra values ranged between 18 – 53 µin which met drawing requirements.

DA-CV-1 2021 event blade fatigue sample

CBDUAY1357 Baseline fatigue sample

Laser Profilometry

Stylus Profilometry

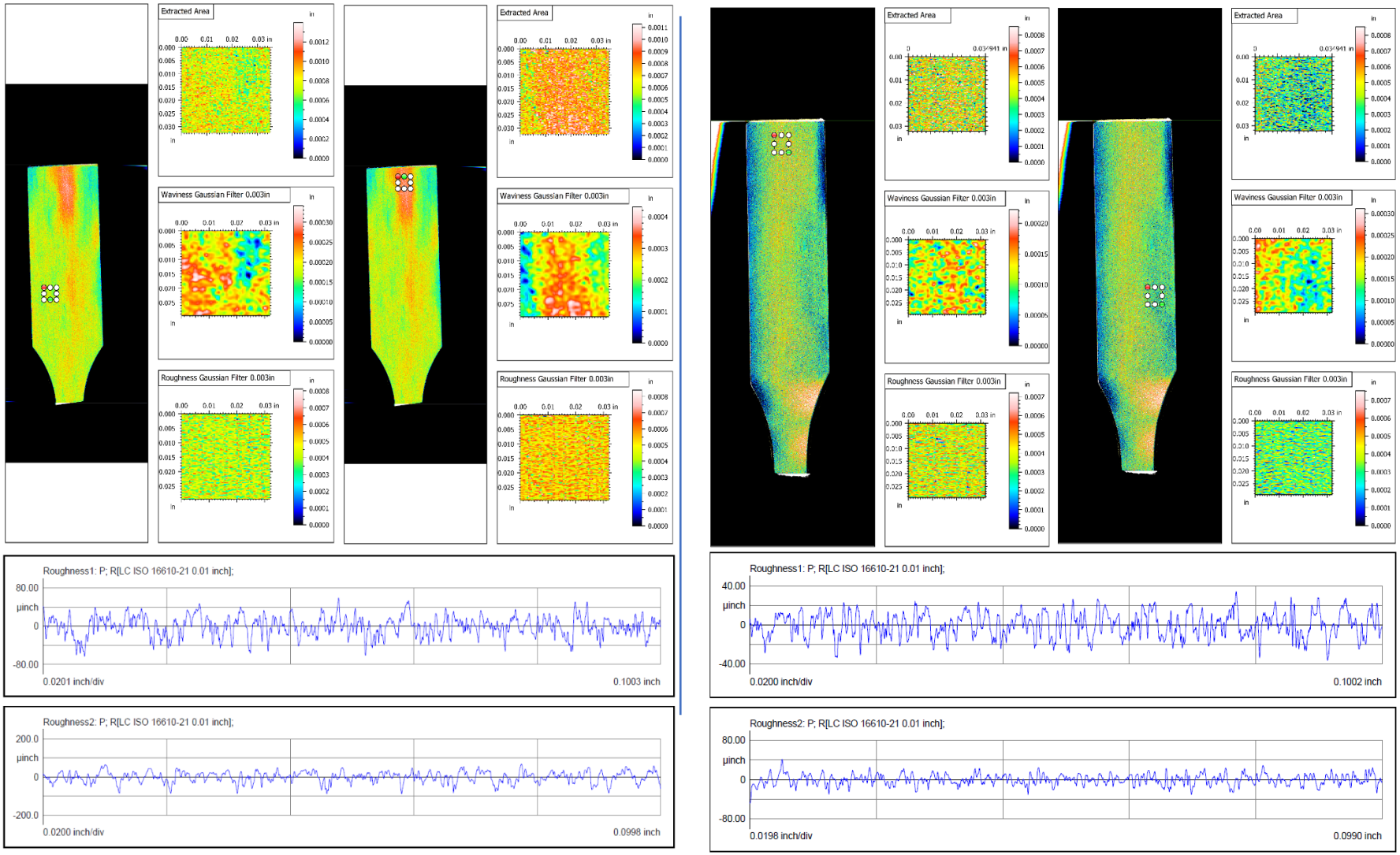

Figure 80: Images showing the laser and stylus profilometry results on fatigue test coupons from the incident blade (DA-CV-1) and a baseline fatigue sample from blade S/N CBDUAY1357.

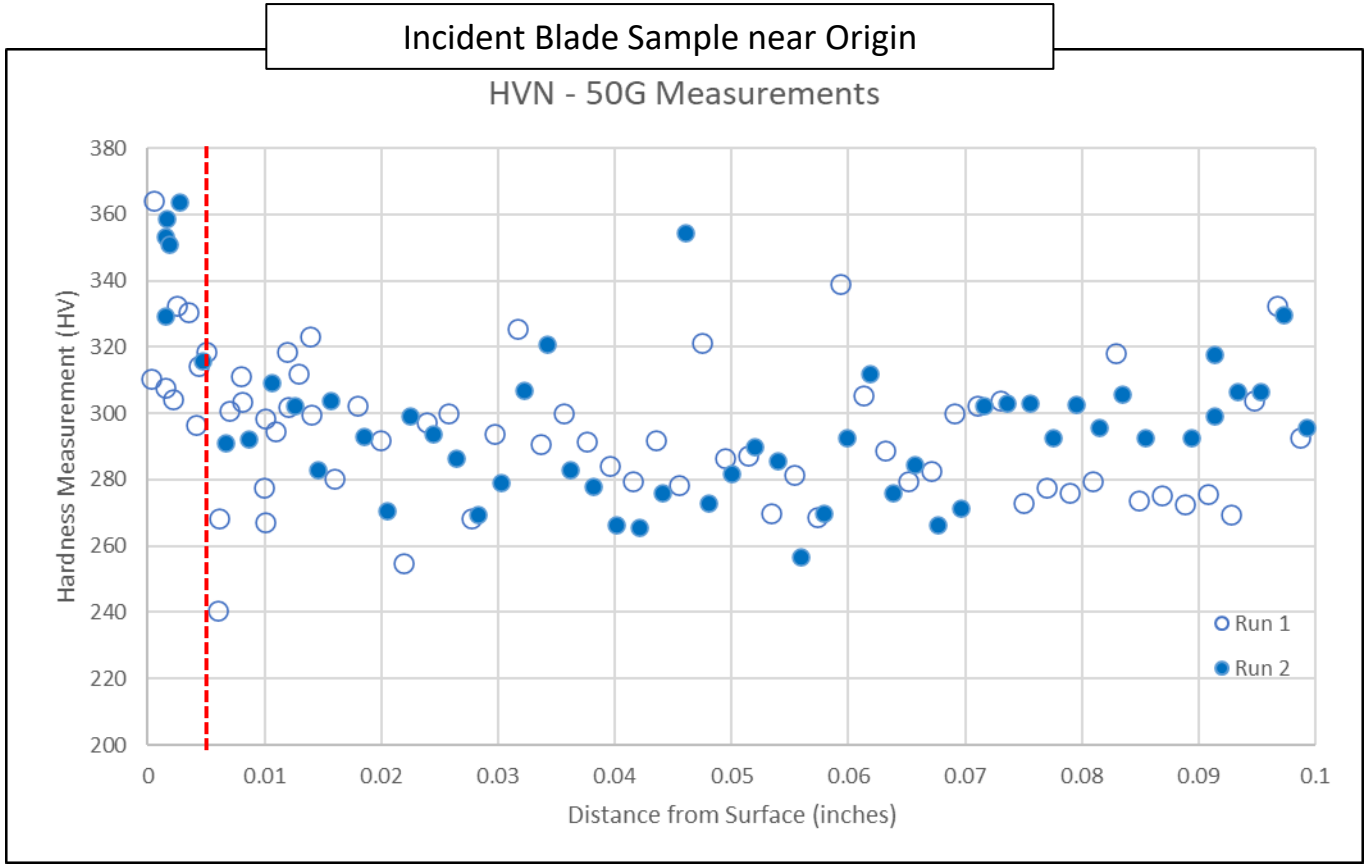

Figure 81: Graph showing the results of microhardness measurement traces taken from the cavity surface near the primary origin. A slight increase in hardness was observed within 0.005" of the surface.

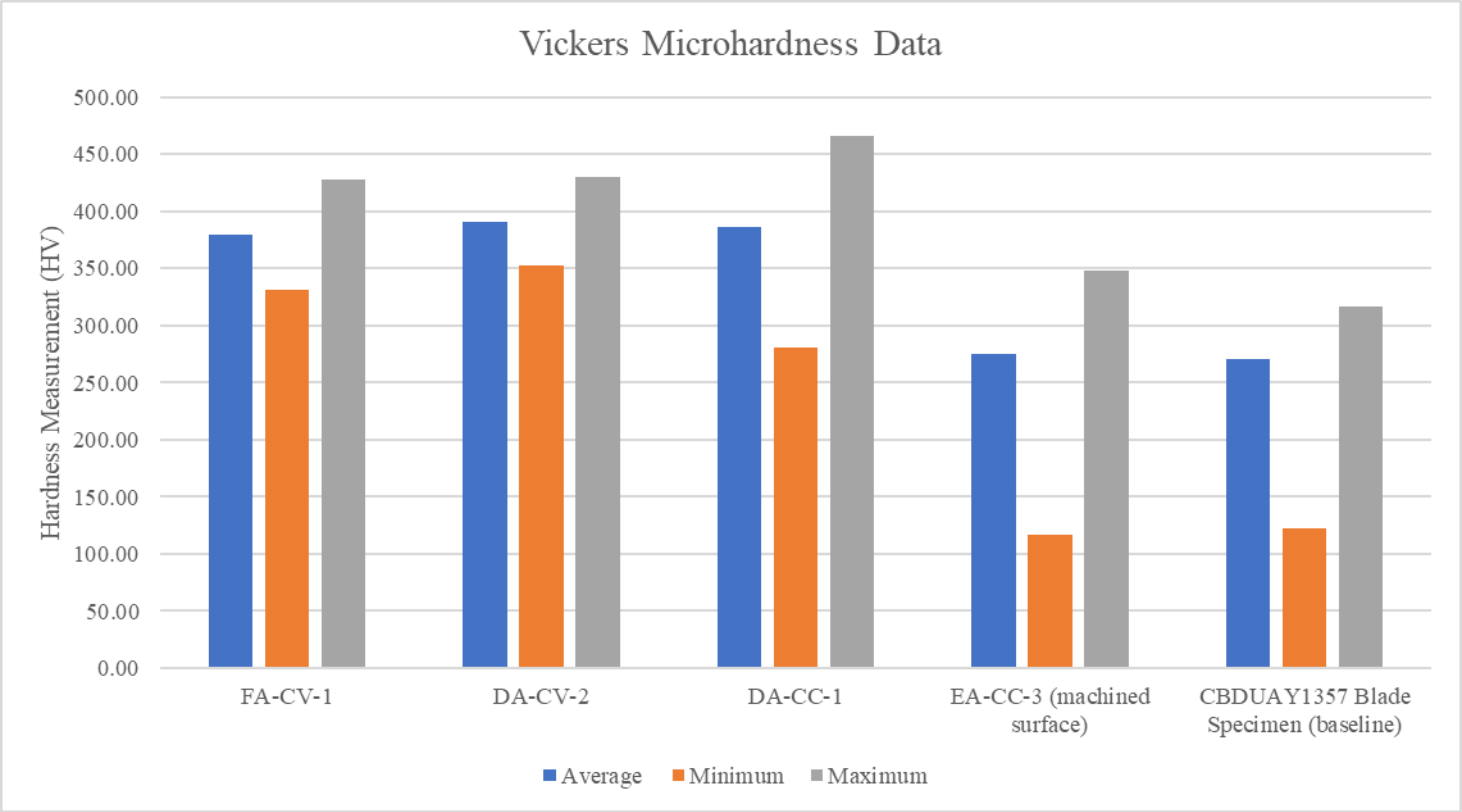

Figure 82: Graph showing the average, minimum, and maximum hardness measurements on the surface of the fatigue test coupons.

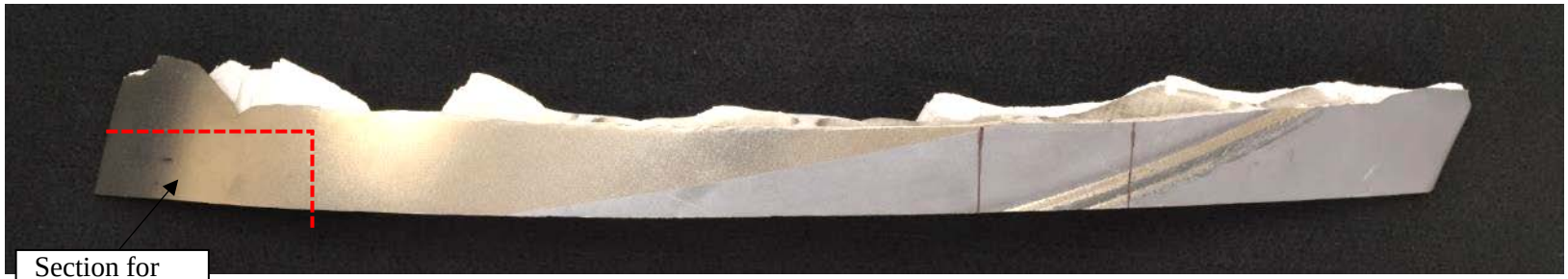

Element	Al	B	Cu	Fe	Si	V	Y	Cr
Wt. %	6.64	<0.001	0.001	0.18	0.032	4.17	<0.001	0.017
Element	Ni	Sn	C	S	H	O	N	Ti
Wt. %	0.015	0.013	0.016	<0.001	0.0017	0.18	0.004	Bal.

Figure 83: Table showing wet chemistry results on the bulk fan blade material. Chips were removed from near the LE just inboard of the fracture surface as shown by the red lines above.

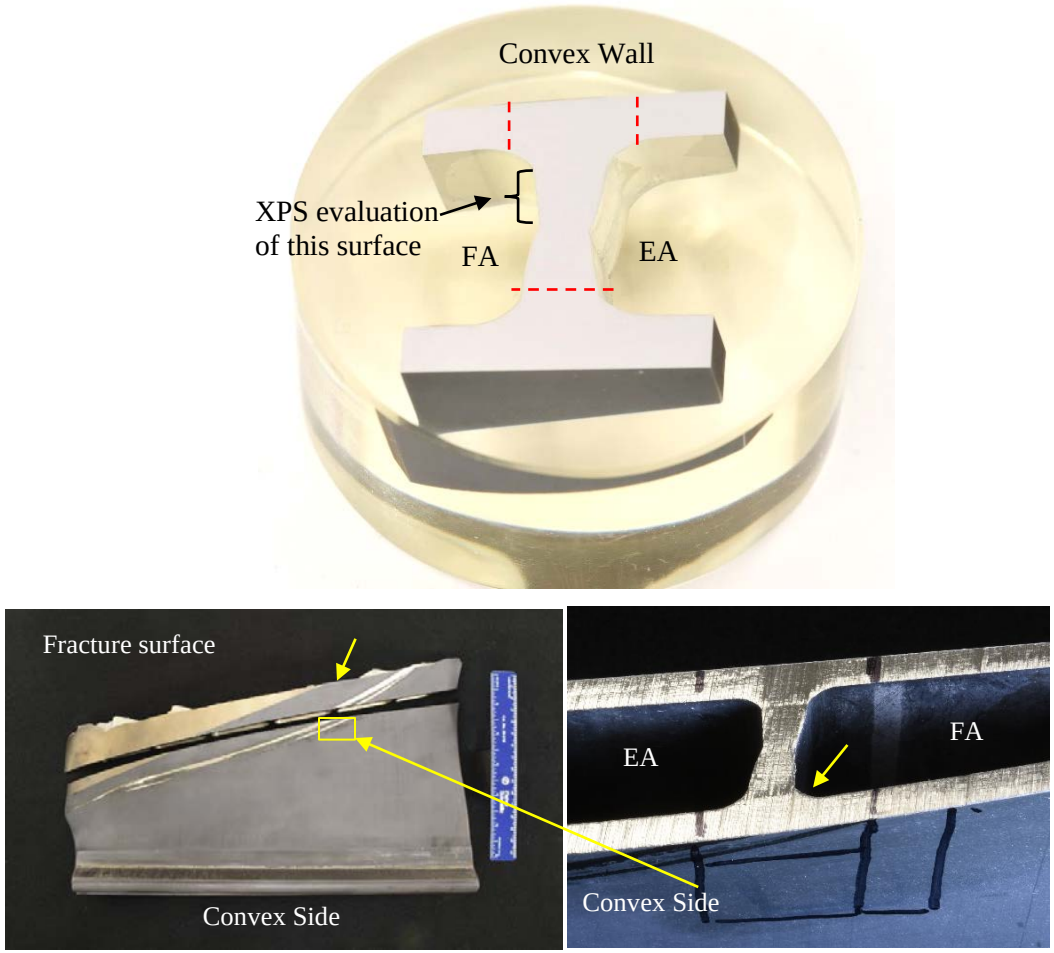

Figure 84: XPS was completed at the location shown above, on a rib in cavity FA, approximately 1 inch below the fracture surface.

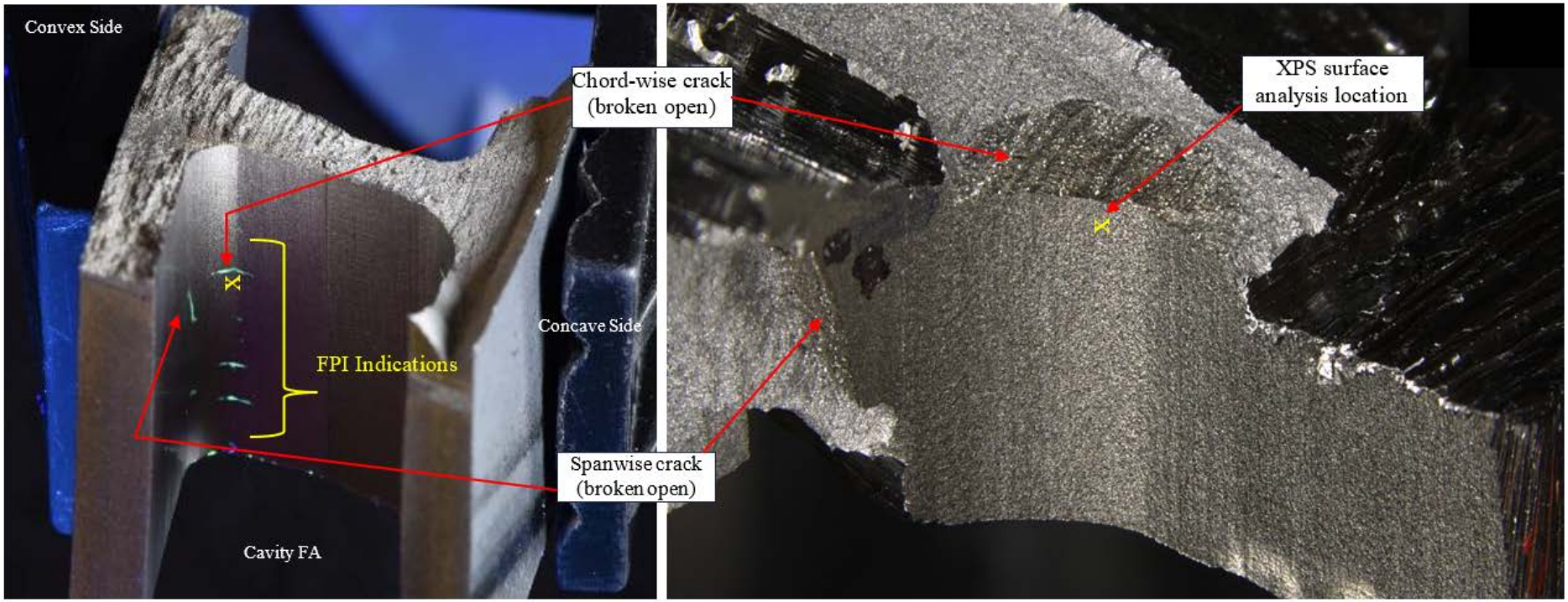

Figure 85: XPS was completed at the location shown above, near an origin on the secondary chordwise crack. The section that was used also contained half of the spanwise crack surface.

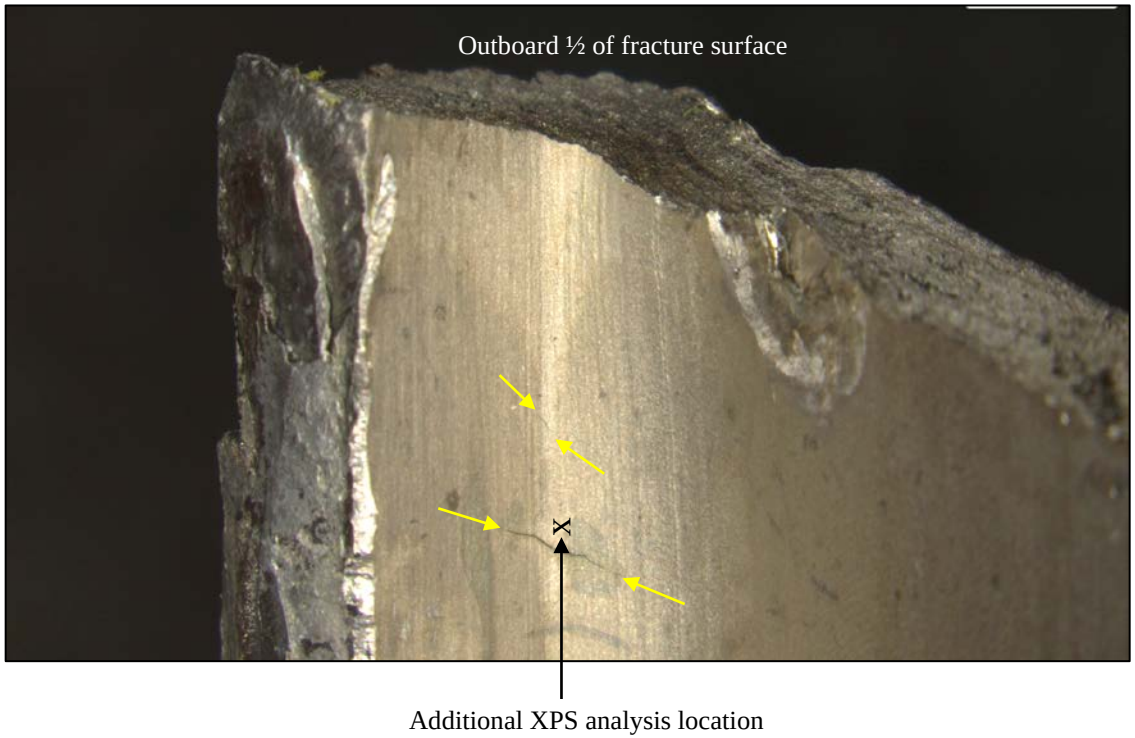

Figure 86: The third XPS trial was completed at the location shown above, near an origin on the outboard secondary chordwise crack.

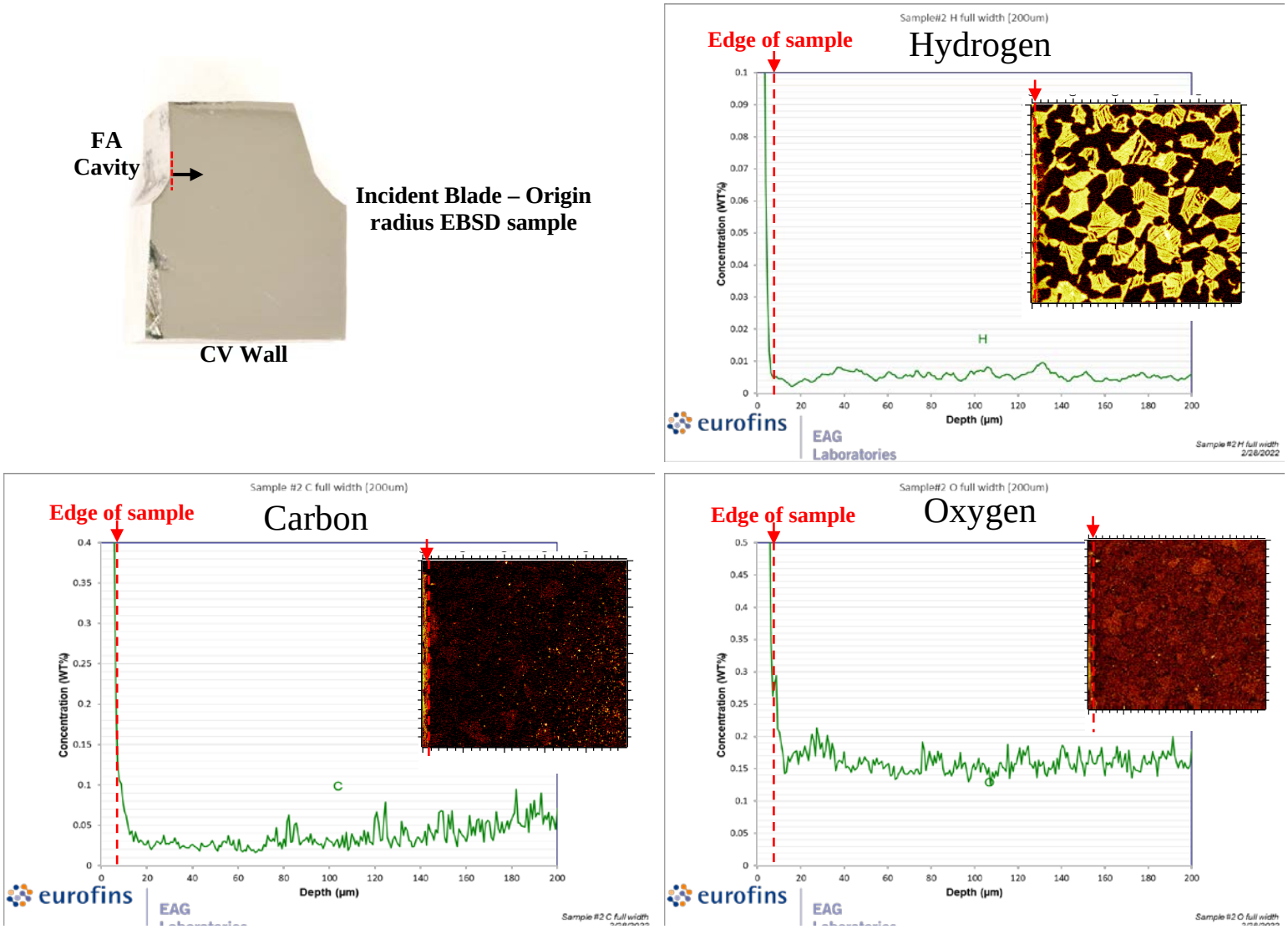

Figure 87: SIMS analysis of a secondary fatigue origin sample from the event blade did not detect significant surface concentration gradients for H, C or O. Concentration line scans were taken over the width of an elemental map that is 200 µm wide. The runout concentration levels were within spec limits for Ti 6-4 blade alloy.

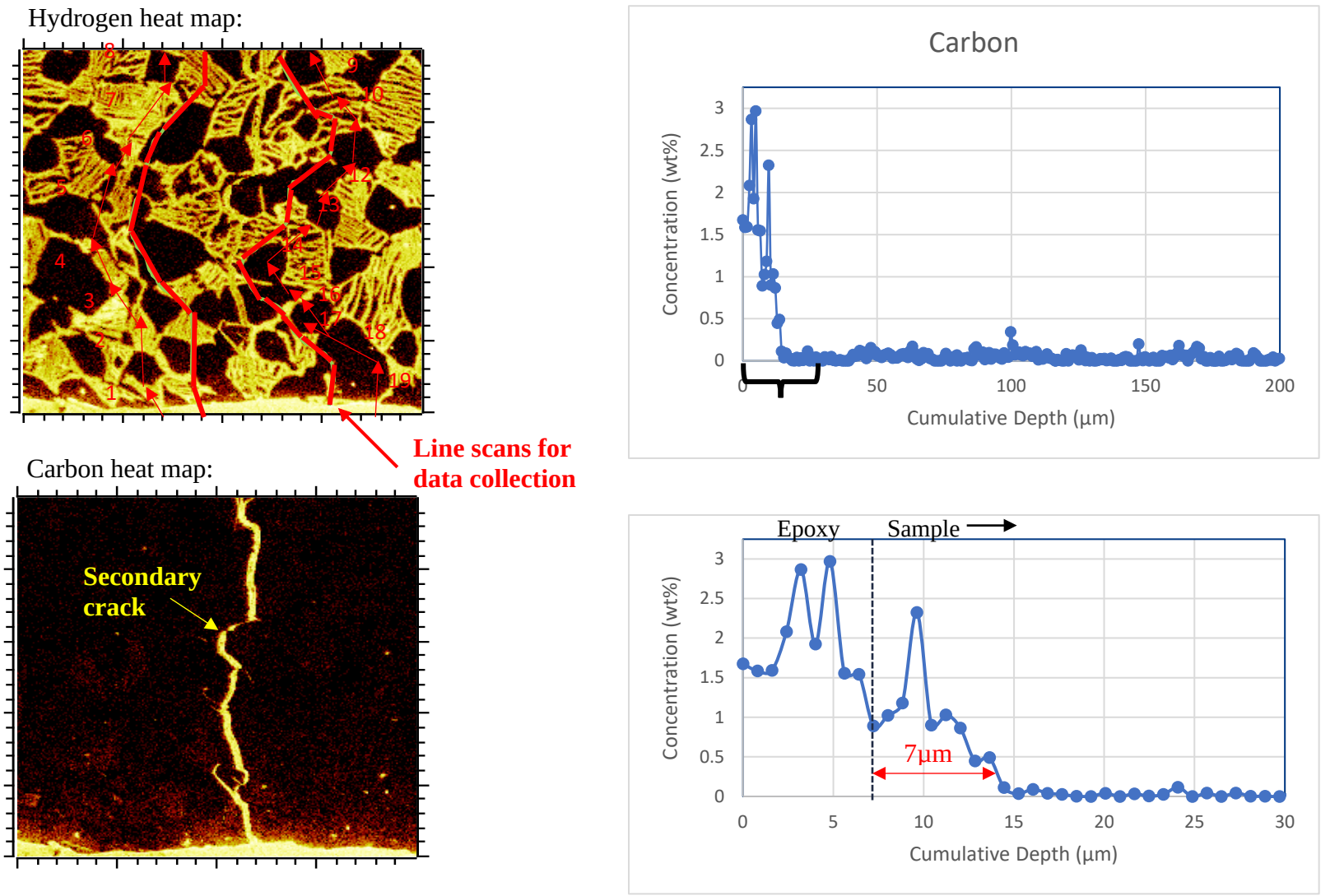

Figure 88: SIMS analysis adjacent to a flowpath secondary fatigue crack from the event blade (Reference Section 2.1.2.3) detected a 7µm carbon gradient starting at concentrations of approximately 1 wt%.

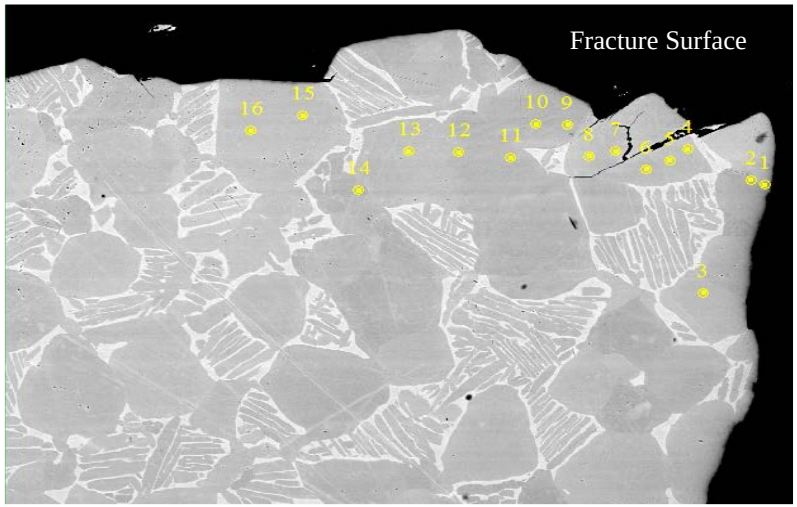

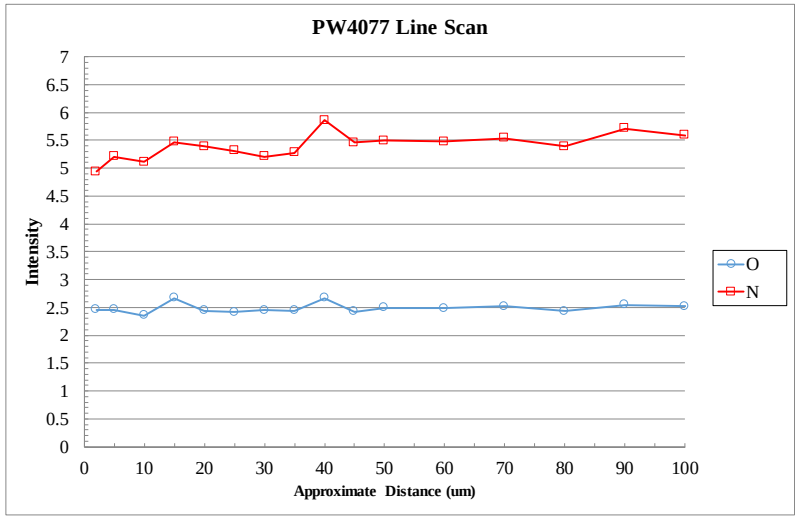

		Weight %				Relative Intensity
Area	Distance (um)	Ti	Al	V	O	N
1	2	91	6.6	2.2	2.5	4.9
2	5	90	7.4	2.2	2.5	5.2
3	10	90	7.5	2.1	2.4	5.1
4	15	91	7.2	2.2	2.7	5.5
5	20	90	7.6	1.9	2.4	5.4
6	25	90	7.6	2.0	2.4	5.3
7	30	91	7.5	1.9	2.4	5.2
8	35	90	7.6	2.1	2.4	5.3
9	40	90	7.6	2.0	2.7	5.9
10	45	91	7.6	1.8	2.4	5.5
11	50	91	7.5	1.9	2.5	5.5
12	60	90	7.6	1.9	2.5	5.5
13	70	91	7.3	2.1	2.5	5.5
14	80	91	7.3	2.2	2.4	5.4
15	90	90	7.7	1.8	2.5	5.7
16	100	91	7.7	1.8	2.5	5.6
Matrix-1		91	7.4	1.8	2.3	5.2
Matrix-2		90	7.5	2.2	2.2	5.4
Matrix-3		91	7.2	2.2	2.5	5.4
Matrix-4		91	7.5	1.9	2.0	5.4
Matrix-5		91	7.5	2.0	2.4	5.5

Figure 89: Image showing EMP traces into the material near the fracture surface on the transverse section through the primary origin (top left image). The data and graph show no detectable levels of nitrogen above the matrix alpha baseline and no significant differences in the oxygen levels between the near surface and matrix alpha phases.

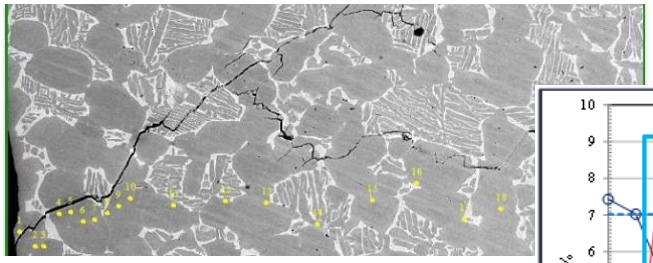

Outboard Crack

Crack A Results

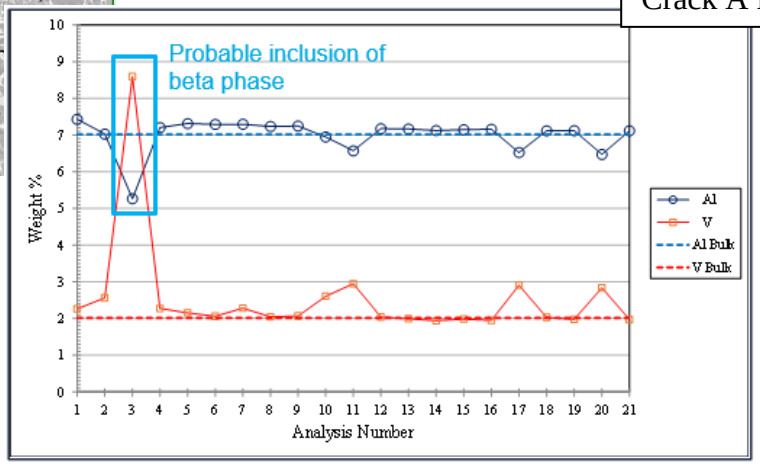

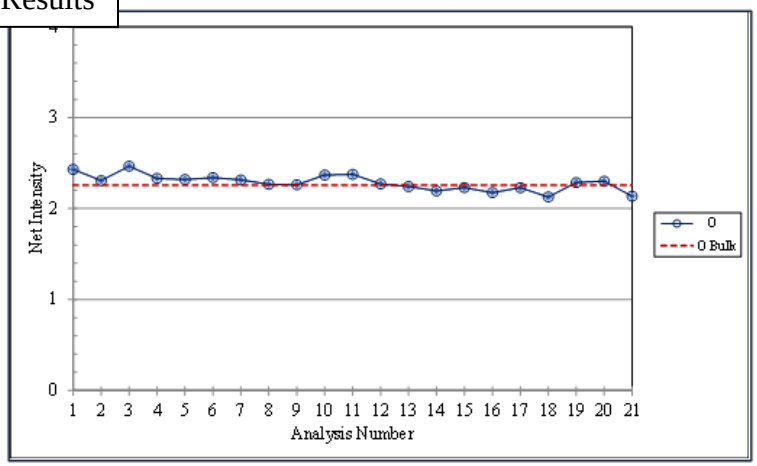

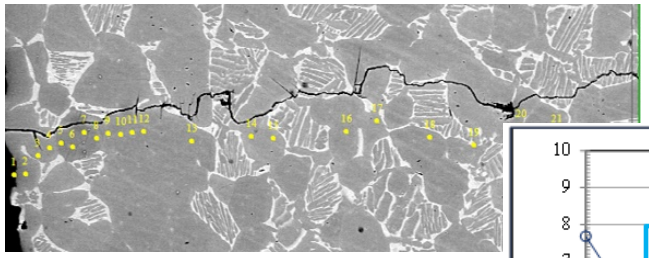

Inboard Crack

Crack B Results

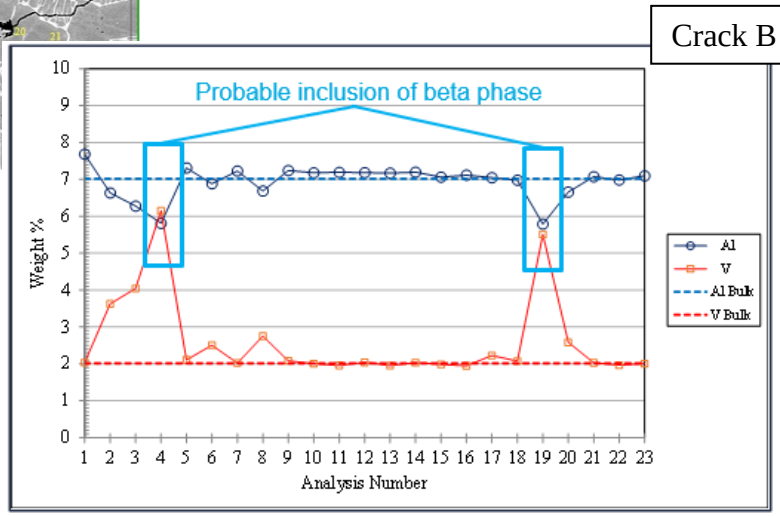

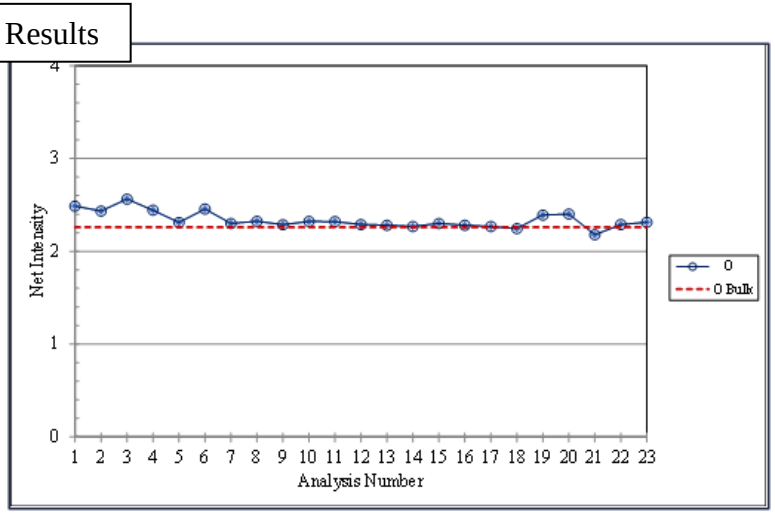

Figure 90: EMP results showing no significant difference in Al, V, and O levels between the surface and bulk alpha grains in the section through additional chordwise cracks.

Carbon Standard 1
Heat treated per blade final form cycle
Etch effect ~0.0024”

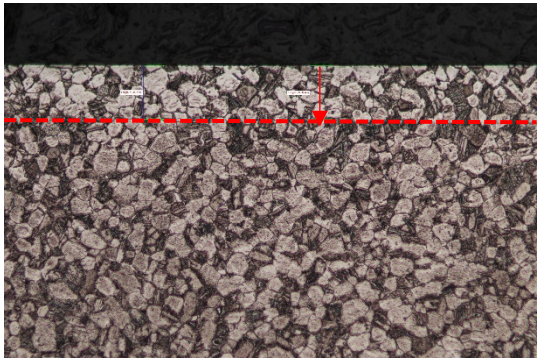

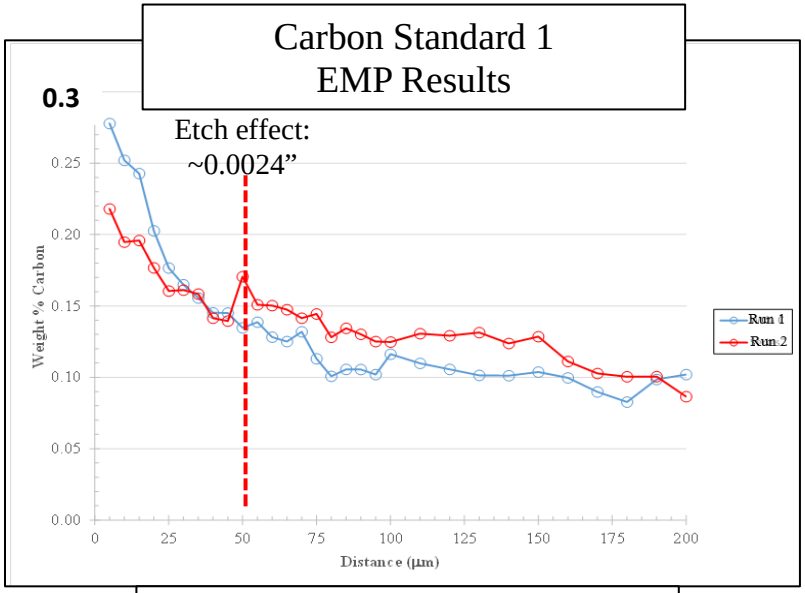

Carbon Standard 2
Heat treat process replicated processes prior to forming (longer and higher temp than sample 1)
Etch effect varied from 0.014” to 0.025”

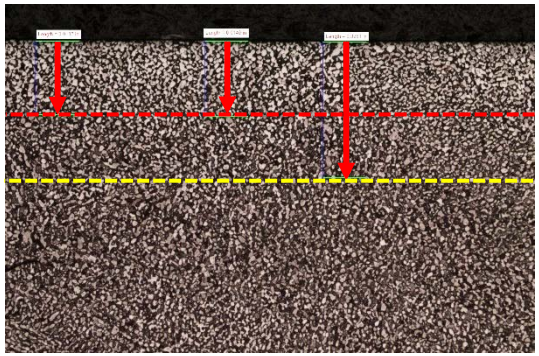

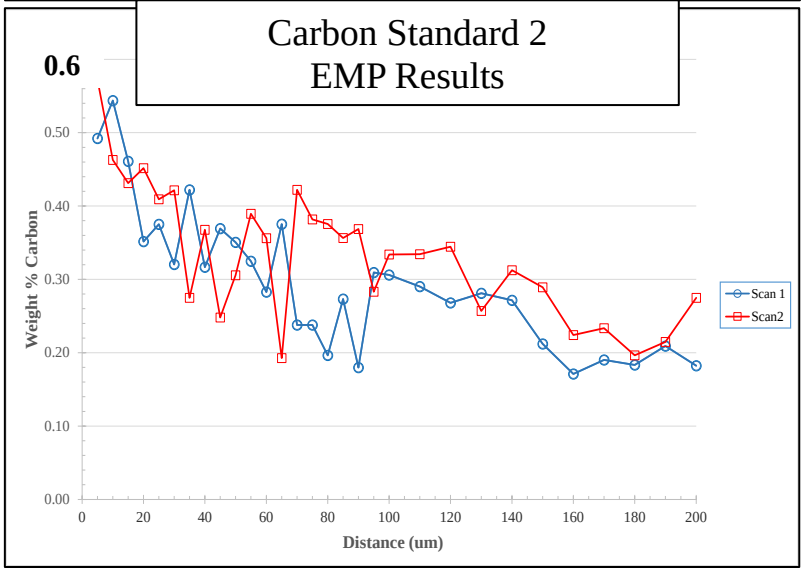

Figure 91: Images showing the etch effect and EMP carbon linescan results of the carbon contaminated samples.

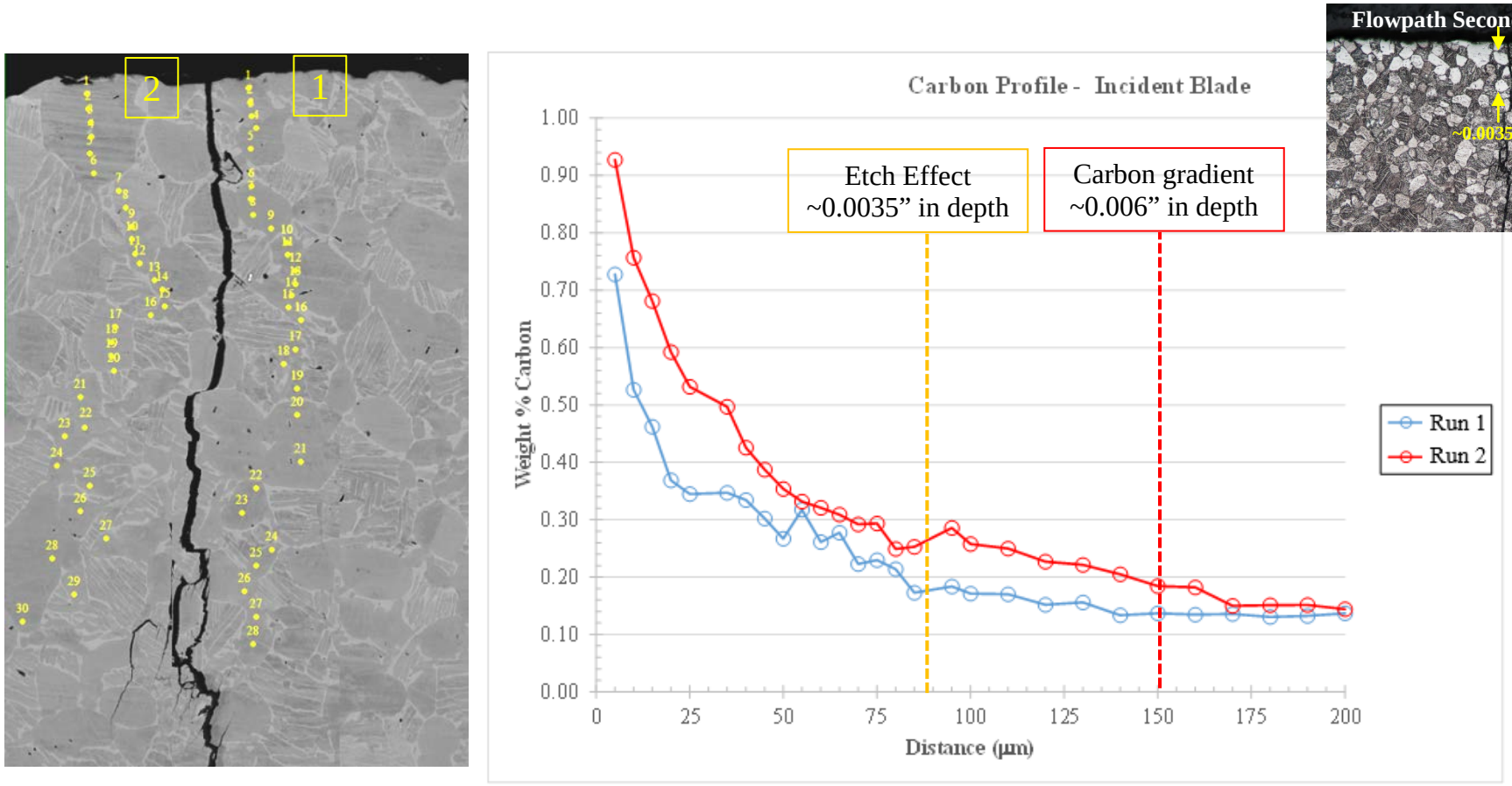

Figure 92: Two EMP carbon traces on a spanwise metallographic section through secondary flowpath cracks (Reference Section 2.1.2.3) identified a carbon concentration gradient from the surface to approximately 0.006” in depth.

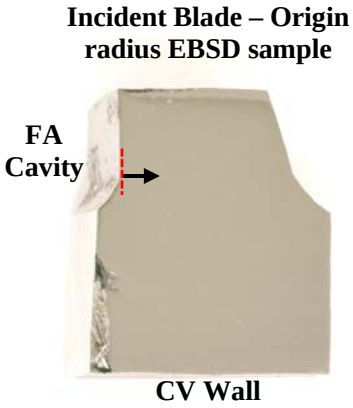

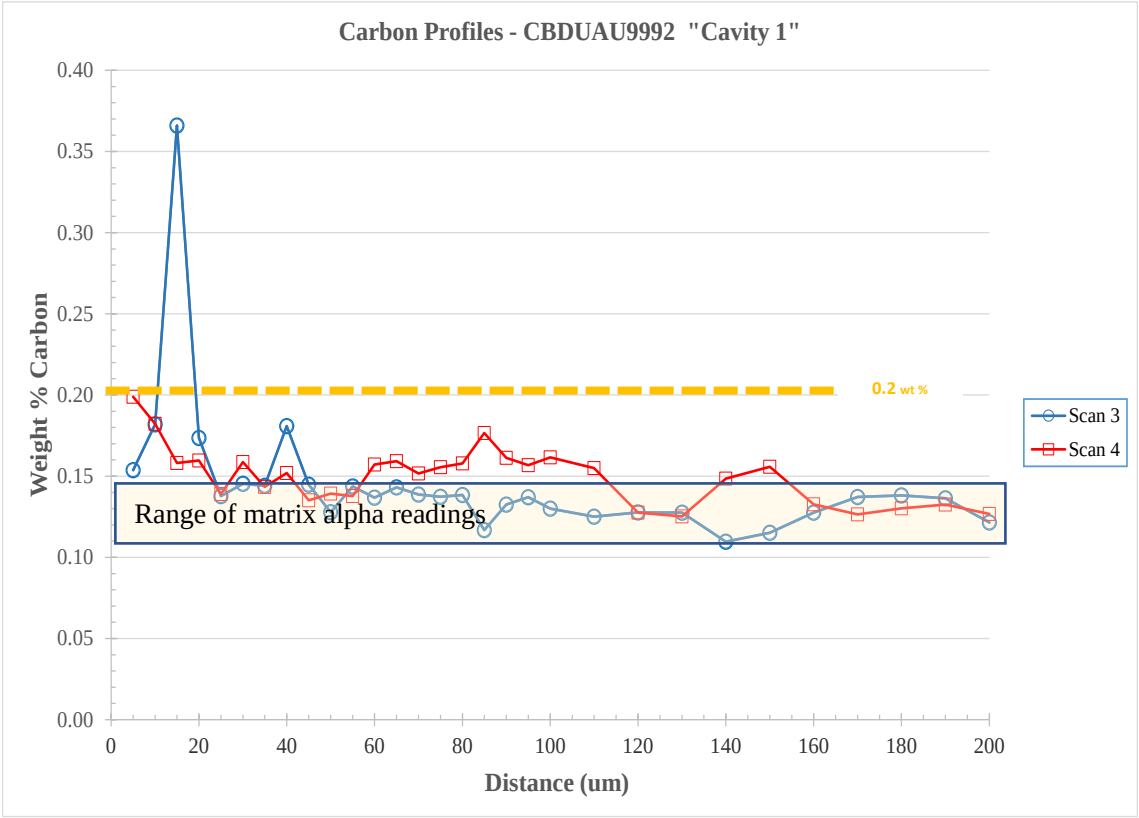

Figure 93: Two EMP carbon traces were completed on the secondary flowpath crack EBSD origin sample that was previously evaluated using SIMS. EMP did not detect a carbon gradient, consistent with the SIMS results which also did not detect a gradient (Reference Figure 87).

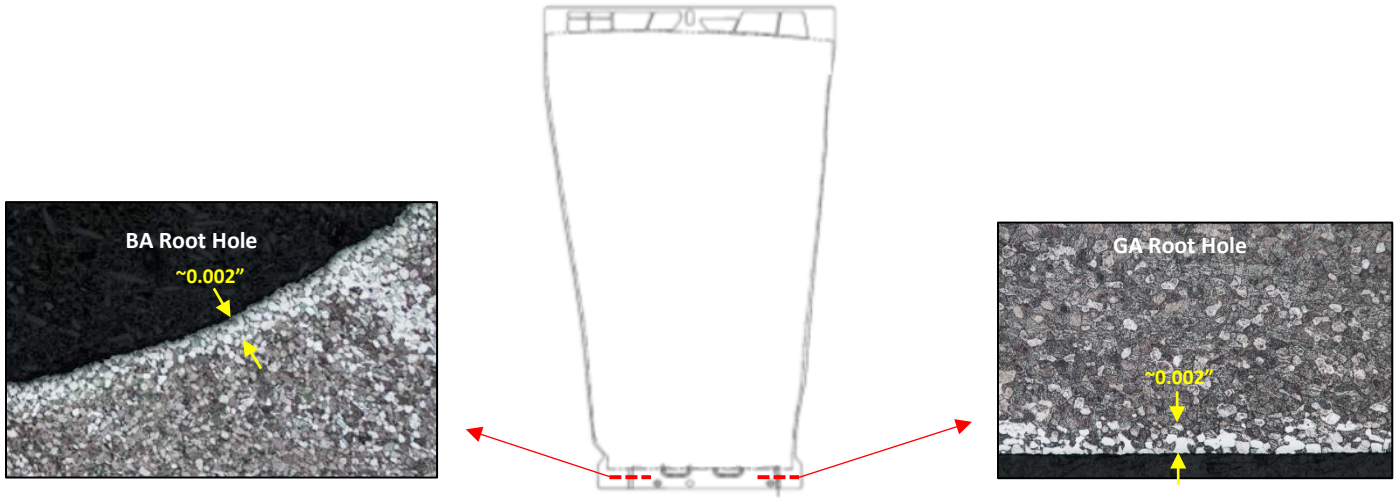

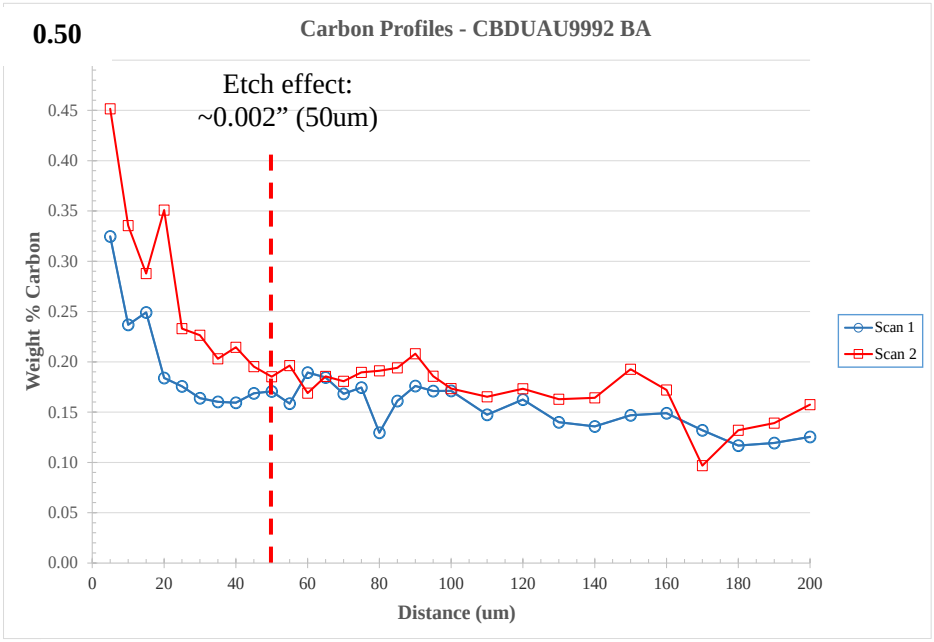

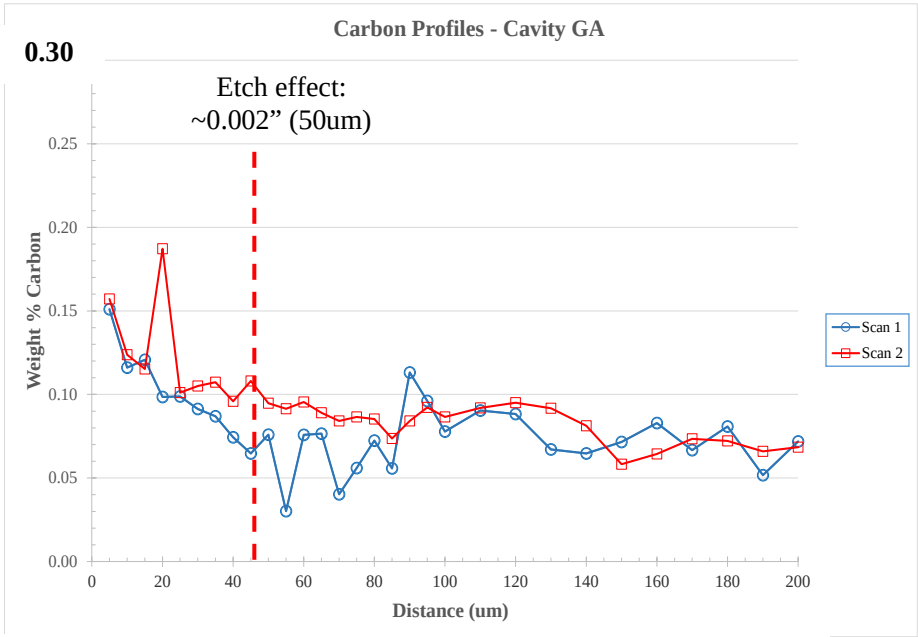

Figure 94: EMP carbon traces at cavities BA and GA identified smaller carbon gradients from the surface.

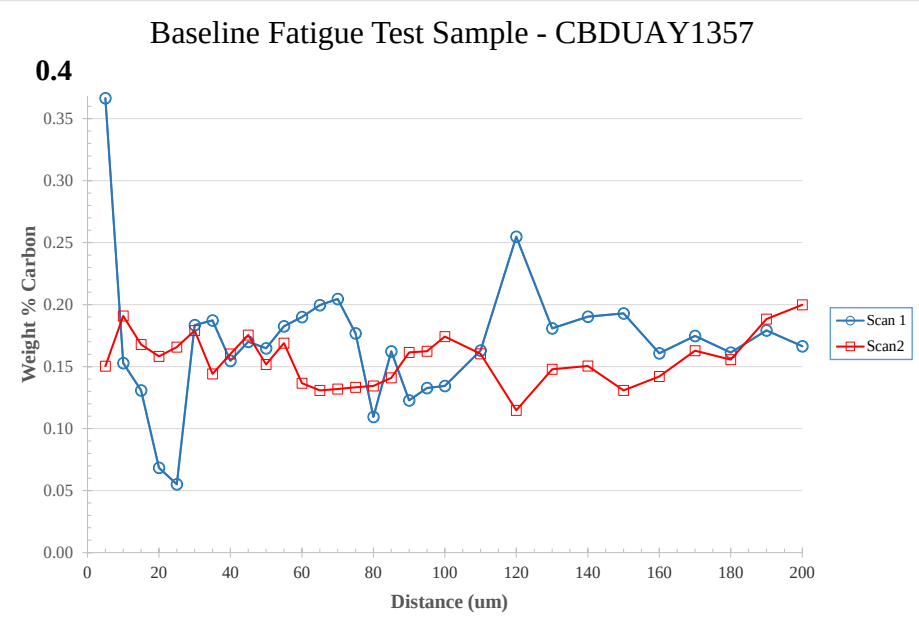

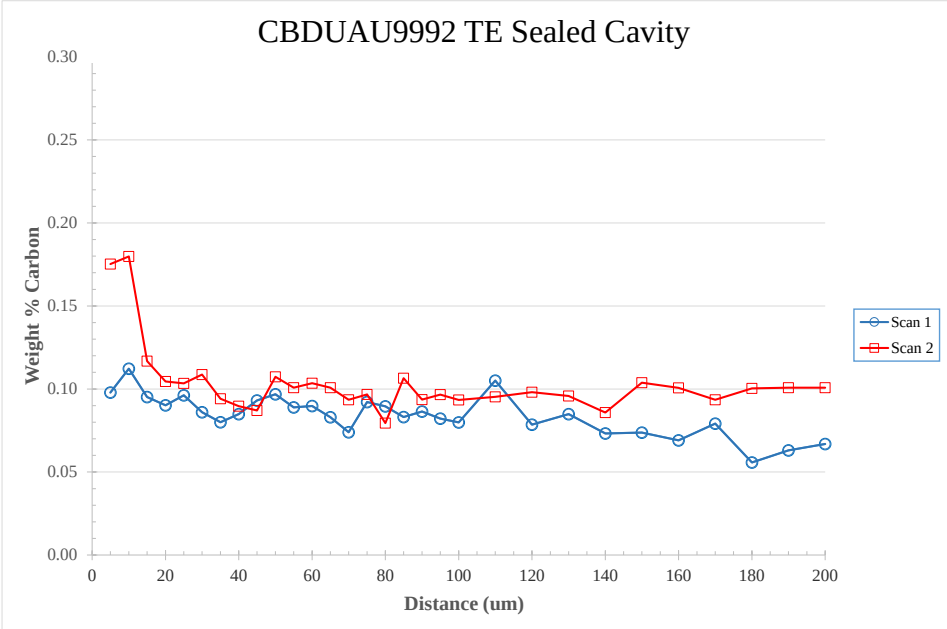

Figure 95: EMP carbon traces of the baseline fatigue test sample from CBDUAY1357 and from the sealed cavity on the incident blade. Neither showed a carbon gradient at the surface.

~~ASSY 55A801~~
ASSY 56A201 B R01
A12 286
CC RABET
CV RABFE
S/N CBDUA49233

Figure 96: Image showing the following sister blade, CBDUA49233, the part markings, and the pieces recovered from the ground that were found to be remnants of this blade.

	P/N	S/N
1	55A801	CBDUAU9698
2	55A801	CBDUAW0002
3	55A801	CBDUAW0148
4	55A801	CBDUAU9946
5	55A801	CBDUAU9999
6	55A801	CBDUAU9945
7	55A801	CBDUA02403
8	55A801	CBDUAU9998
9	55A801	CBDUA00652
10	55A801	CBDUAY4296
11	55A801	CBDUAY1402
12	55A801	CBDUA17218
13	55A801	CBDUAU9590
14	55A801	CBDUAU9856
15	55A801	CBDUA02397
16	55A801	CBDUAW0089
17	55A801	CBDUAU9220
18	56A201	CBDUA49233
19	55A801	CBDUAU9992
20	55A801	CBDUAU9701
21	55A801	CBDUA29456
22	55A801	CBDUAY1394

Yellow– blades that were not with the set for the lifespan of the incident blade

Figure 97: Image showing the engine at teardown and the corresponding blade serial numbers. The yellow highlighted blades were not with the set for the lifespan of the incident blade. The blades highlighted in gray were the blades destructively evaluated.